

博士論文

A Multi-Scale Study on Stress Development and
Pore Structure of
Contemporary Expansive Concrete

(膨張コンクリートの応力進展および空隙構造に関するマルチスケール研究)

区 光峰
Guangfeng OU

A dissertation submitted to
The University of Tokyo
In partial fulfillment for the requirements for
The Degree of Doctor of Philosophy

Supervisor
Prof. Toshiharu KISHI

**Department of Civil Engineering &
Institute of Industrial Science
The University of Tokyo
Tokyo, Japan**

August 2021

I was within and without,
simultaneously enchanted and repelled by the inexhaustible variety of life.
- F. Scott Fitzgerald, *The Great Gatsby*

Do not go gentle into that good night.
- Dylan Thomas

ABSTRACT

The initiation and propagation of unexpected early-age cracking in concrete will lead to rapid deterioration of the concrete structures, which closely associates with the penetration of aggressive substances and the corrosion of steel bars. These cracks reduce the margin of safety and also, jeopardize the durability performance of concrete structures in a long term. Due to its vast significance in engineering, related researches have been widely conducted since last century. To mitigate cracking, expansive additives have generally been used to compensate the shrinkage at early age. However, even though various expansive additives and supplementary cementitious materials (SCMs) have witnessed certain advancements during these years, the problems of early-age cracking are still not fully solved. Especially, it was found on site that the commonly-used calcium sulfoaluminate type additive (CSA) cannot compensate the rapid development of shrinkage during high temperature conditions and cracking was difficult to be controlled under such situation. The addition of fly ash or slag was also found to exert only limited effect on compensating the shrinkage stress. The complexity of these problems is not only related to the physical properties of concrete itself but, is also closely related to the temperature conditions and restraint degrees of the structures. And thus, the empirical method for mix design is not always effective, due to the variation of temperature and restraint conditions in different structures. In the contemporary era, how to design mix proportions using expansive additives remains a critical task for both researchers and engineers. To address such a problem, it requires a systematic evaluation method to quantify the deformation and stress development of concrete materials under varied temperature conditions and restraint degrees.

The first objective of this study is to experimentally evaluate and compare the cracking performances of OPC concrete and expansive concrete. It highlights the importance of a reliable and effective testing device. The experimental device named temperature stress testing machine has been regarded as one of the most effective and powerful tools. The UTokyo TSTM was originally constructed by Lin (Lin, 2006) in our research lab, which revealed accurate, reliable and reproducible performances. In my current study, some of the features have been updated on this device. Systematic experiments on early-age deformation and stress development of OPC, CSA and MgO concrete have been conducted using TSTM. It is confirmed in the experiments that CSA concrete fails to compensate rapid shrinkage stress effectively under high temperature and full restraint condition, while its hybrid use with lightweight aggregate indicates excellent cracking performance (Firstly discovered by Lin (Lin, 2006)). Apart from CSA, MgO is a relatively new type of expansive additive, which has been used for many dam structures in China. But the stress-related performance and in-depth understanding regarding mechanism of expansion is still strongly required. It was found from this study that MgO concrete can offer prolonged expansion due to the less water dependency for complete hydration. The Type-II MgO can effectively compensate shrinkage stress even under high temperature condition. Also, this study

shows for the first time that MgO concrete has better resistance to drying stress than CSA concrete under wetting/drying cycles. Plausible mechanisms can be attributed to the retarded expansion due to less water dependency and the finer pore structure which slows down the water evaporation from pores. Experimental results from nitrogen adsorption-desorption (NAD) tests and mercury intrusion porosimetry (MIP) show that MgO concrete has finer pore structure and more bottle neck pores, thus hindering moisture movement during drying. The experiment results offer us valuable insights on the application of expansive concrete in realistic construction site.

The second objective of the current study is to establish a multi-scale analytical model to quantify the deformation and stress development of concrete materials. It can provide valuable guidance information for mix design in practice. In order to achieve this goal, the microscopic mechanisms related to the effectiveness of expansion should be unfolded. It is found that expansion is closely linked with the pore structure and the moisture state inside these pores. The coupled thermo-hygro-mechanical process is simulated using a similar logic as DuCOM model (Maekawa, Ishida and Kishi, 2009). A new concept to interpret and model the expansion for CSA concrete is proposed. It is considered that the rapid drop of free water availability leads to ineffective expansion of CSA concrete, while a combined use with lightweight aggregate can solve this problem because of internal curing effect. By a coupled thermo-hygro-mechanical computation scheme, the free water availability in pores (nanometer scale) for CSA concrete with/without lightweight aggregate could be quantified reasonably, which can be further upscaled to model expansion and stress development at larger scale. To better elucidate how pore structure may affect the water availability, an innovative pore structure based on the combined effect between densification and volume expansion has been put forward. The proposed pore structure model attempts to link some of the conventional understandings ((Feldman and Sereda, 1970; Jennings, 2008a; Maekawa, Ishida and Kishi, 2009)) with innovative interpretations from ¹H-NMR technique. The purpose of this proposal is also to better clarify the role of each category of pores and offer clearer insights on the behavior of moisture movement inside these pores.

In conclusion, this study comprehensively investigates the deformation and stress development of OPC, CSA and MgO concrete using TSTM. It offers us valuable information on their cracking performances under varied temperature and restraint conditions during early age. The stress development of CSA and MgO concrete under wetting/drying cycles are also examined and compared. The pore structures of OPC, CSA and MgO cement pastes are studied by MIP and NAD. Additionally, a pore structure model for both OPC and CSA is proposed and implemented into the coupled thermo-hygro-mechanical model. A new nanostructure is established on basis of conclusions from a series of ¹H-NMR studies, which highlights the role of “gateway” gel pores and interlocked inter-hydrate pores for water exchange behavior.

Acknowledgement

I would like to express my great gratitude to my supervisor, Prof. Toshiharu, KISHI, for his constant instruction and support during my PhD life. The sharp insights along with careful considerations have shaped my views upon research and future career. The in-depth discussion and high requirement have motivated me a lot. I would also like to thank the committee of examiners: Prof. Tetsuya ISHIDA, Prof. Ippei MARUYAMA, Assoc. Prof. Kohei NAGAI (especially for the donation of monitor for TSTM), Assoc. Prof. Yuya SAKAI and Asst. Prof. Yuya, TAKAHASHI. Their valuable and meaningful comments offer me much help on the improvement of research.

Special thanks are given to Dr. Zhihai LIN, who recommended me to Kishi lab and offered me a lot of supports during the hard time of repairing TSTM. The valuable advice on research, application of TSTM and future development have greatly inspired me. Asst. Prof. Tomohisa KAMADA also supported, helped and encouraged me a lot, for all the detailed experimental procedures and patient discussions. Dr. Seunghyun NA and Dr. Seishi GOTO have given me kind and useful support as well.

Thanks to Shobond Scholarship for offering support during my PhD study and all my colleagues at Utokyo. I missed Avadh, Yaser, Vikas, Suhas and Dheeraj for their really bad jokes and pranks, and those funny experiences with Keita SUZUKI, Phalkong, Hanjing LIN, Yoko Ito, Aki, Dr. Punyawut, Vi Soth, Vu Cuong, Dr. Yuki Yokoyama, Dr. Gaddam, Dr. Adel, Dr. Shunsei Tanaka and Dr. Yi WANG. Thanks to Yuhan ZHENG and Xi JI for making fun on my mandarin accent and everything. Thanks to Shuai SHAO, Shuohan WANG and Yue WANG for simply helping me nothing. Thanks to K. Chirayu, Dr. K. Pen and Dr. jie FANG from Concrete Lab for helping me with DuCOM. Thanks to Chisei Mizuno from NI company. I have to show my sincere gratitude to those who helped me with the huge amount of concrete casting. I will treasure those memorable days and nights I had spent with you all.

Thanks to my close friends in Foshan, Peiming LIANG, Feng ZHANG, Dr. Yuxiang YANG, Yinming LIANG, Xianhua OU, Weixiong TANG, Maisui NING, Congyin ZHU, Luyin MO and kai WU for all of the interesting (mostly pointless) conversations. Thanks to Dr. Mei YANG and Dr. Zhaorui YAN for discussion on the useful (actually useless) philosophy of life. Thanks to all my professors and colleagues in HKUST and NAMI in Hong Kong. Thanks to all my professors, roommates and classmates in SZU. Thanks to Prof. Liwu MO for kindly offering the MgO expansive additive for free to our lab.

Finally, I would like to express my deepest gratitude to my parents and sister. Without their support and love, I cannot get through the difficult time. I would like to thank my future wife as well, for encouraging me to always look at the bright side and seize the moment.

List of Content

1.	INTRODUCTION.....	1
1.1	Background	1
1.1.1	Early-age Cracking.....	1
1.1.2	The Coupled Thermo-hygro-mechanical Process during Hydration	3
1.2	Review on Experimental Techniques.....	7
1.2.1	Determination of Free Strain using Length Comparator.....	8
1.2.2	Determination of Restrained Deformation and Restrained Stress.....	8
1.3	Research Significance and Objective	11
1.4	Outline of Dissertation	12
2.	Early-age Deformation and Stress Development	13
2.1	Experimental Device-TSTM	13
2.1.1	Overall Design.....	13
2.1.2	Sensors, Load Cell, Heater and Refrigerator.....	14
2.1.3	Design of Friction Reduction	15
2.1.4	Measurement and Automation	15
2.1.5	Displacement Control System.....	16
2.1.6	Summary on Updated Features	18
2.2	Experimental Scheme for TSTM	19
2.2.1	Full-Restraint Condition.....	19
2.2.2	Free Deformation Condition	20
2.2.3	Measurement of Elastic Modulus.....	20
2.2.4	Evaluation of Early-age Creep	20
2.2.5	High Temperature Condition (Semi-adiabatic Condition).....	21
2.2.6	Low and Medium Temperature Condition.....	21
2.2.7	Curing Condition.....	21
2.3	Experimental Method for TSTM.....	22
2.3.1	Experimental Procedures.....	22
2.4	Materials and Mix Proportions.....	24
2.4.1	Notations	26

2.4.2	Fresh Properties and Compressive Strength.....	26
2.5	Experimental Results for OPC Concrete.....	27
2.5.1	Effect of w/c on deformation and stress development	27
2.5.2	Effect of aggregate volume ratio on deformation and stress development	28
2.6	Multi-scale Modeling of OPC Concrete using DuCOM	29
2.7	A Proposed Parallel-Serial Constitutive Law.....	33
2.7.1	The mathematical formulation	34
2.7.2	Formulation of relaxed stress	36
2.7.3	Consideration of Reduced Tensile Modulus	36
2.7.4	Computation Flow of the Constitutive Law	38
2.7.5	Model Validation for OPC concrete.....	39
2.8	Experimental Results for CSA Concrete.....	44
2.8.1	Deformation and Stress Development of CSA Concrete with/without LA	44
2.8.2	Visualization of Internal Curing Effect.....	45
2.9	The Expansion Mechanism of CSA Concrete and Modeling	46
2.9.1	Discussion on expansion mechanism of CSA concrete	46
2.9.2	Modeling of deformation and stress development of CSA concrete.....	48
2.10	The Expansion Behavior of MgO Concrete.....	52
2.10.1	Stress Development of Type-I MgO	53
2.10.2	Stress Development of Type-II MgO.....	54
2.10.3	The effect of different temperature conditions.....	56
2.10.4	Calcination condition and reactivities of MgO concrete.....	57
2.10.5	Measurement of Thermal Expansion Coefficient (TEC)	58
2.11	Cracking Sensitivity under Wetting-Drying Cycles.....	59
3.	The Thermo-Hygro-Mechanical Model	62
3.1	The hydration heat model.....	63
3.2	Moisture Isotherms.....	64
3.3	The Computation Scheme of the Coupled Model.....	66
3.3.1	Computation of Autogenous Shrinkage	69
3.3.2	Computation of Thermal Deformation.....	69
3.3.3	Modeling of Modulus Development	70

3.4	The Pore Structure Model	70
3.4.1	Introduction and Review of Pore Structure.....	70
3.4.2	Simulation-aided study using Mic.....	73
3.4.3	The proposed pore structure model based on combined effect	82
3.4.4	Pore structure characterization of MgO and CSA concrete	97
3.4.5	A hypothesis on the nanostructure of C-S-H.....	99
3.4.6	Pore size distribution and moisture state of OPC, MgO and CSA.....	103
3.4.7	The insight on drying behaviour	105
3.4.8	Limitations of the pore structure model and current gap of understanding	106
4.	Conclusions and Future Perspectives.....	108
4.1	Conclusions	108
4.2	Future Perspectives.....	109
5.	Appendix.....	111
5.1	Modelling on Working Principle of Cracking Frame	111
5.2	Modelling on Working Principle of TSTM.....	113
5.3	Prediction of Adiabatic Temperature Rise	118
5.4	Estimation of Porosity from Bulk Density	119
6.	REFERENCES.....	123

List of figures

Figure 1.1 Impact of early-age cracking on life span of concrete structures, corrected from (<i>Non-structural Cracks in Concrete, Cement and Concrete Society, United Kingdom, 1978</i>)	2
Figure 1.2 Calcination Temperature and Expansion Property.....	6
Figure 1.3 (a) Experimental set-up for ASTM C157 standard (b) ASTM C1698 standard	8
Figure 1.4 (a) the covered dual ring and (b) the uncovered dual ring	9
Figure 1.5 Schematic representation of a rigid cracking frame (Springenschmid, 1998)	9
Figure 1.6 Outline of UTokyo TSTM (Ver. 1.0).....	10
Figure 2.1 Overall Design of the Utokyo TSTM.....	13
Figure 2.2 3D model of Utokyo TSTM Ver. 1.1 (model built in SolidWorks and rendered by KeyShot) 14	
Figure 2.3 Measurement and automation of Utokyo TSTM (Ver. 1.1).....	16
Figure 2.4 Real-time remote access and control (Ver. 1.1)	16
Figure 2.5 Methods for Displacement Measurement	17
Figure 2.6 Crosshead deformation and rotation under large tension.....	18
Figure 2.7 Details and Modifications of UTokyo TSTM (Ver. 1.1)	19
Figure 2.8 (a) Full-restraint Condition (b) Free Deformation Condition	20
Figure 2.9 Experimental Procedures for stress/strain measurement using TSTM	23
Figure 2.10 Photo of materials used for TSTM experiments	25
Figure 2.11 Full-restraint stress and free deformation of OPC concrete with w/c:0.45 and 0.30	27
Figure 2.12 Effect of volume ratio of aggregate on deformation and stress development.....	29
Figure 2.13 Mesh and geometry of the simulated OPC concrete beam	30
Figure 2.14 Boundary conditions: free deformation and full-restraint at end surfaces	30
Figure 2.15 Simulation results on the temperature and free deformation using DuCOM.....	32
Figure 2.16 Simulation of full-restraint stress of C45 under low and high temperature	33
Figure 2.17 Simulation of full-restraint stress of C30 and C45V0.5 under high temperature	33
Figure 2.18 Constitutive law between aggregate and cement paste during stress development	34
Figure 2.19 Theoretical elastic stress and restrained stress	36
Figure 2.20 Elastic Modulus of OPC, CSA and CSA concrete with LA under varied conditions (Lin, 2006)	38
Figure 2.21 Reduced Tensile Modulus and Microcracks	38
Figure 2.22 Computation Flow of the Constitutive Law	39

Figure 2.23 Simulation of semi-adiabatic temperature conditions for OPC and CSA concrete	40
Figure 2.24 Schematic diagram of free deformation	41
Figure 2.25 The modeled free deformation of OPC concrete and experimental validation	42
Figure 2.26 Model validation of the restrained stress by proposed constitutive law	43
Figure 2.27 Deformation and stress development of CSA concrete and combination with LA	45
Figure 2.28 Visualization of internal curing effect of lightweight aggregate (after (Lura, 2003))	46
Figure 2.29 Visualization of internal curing effect using a new method.....	46
Figure 2.30 Parameter of free water availability	50
Figure 2.31 The prediction of free deformation of CSA concrete with/without LA. Left: High Temperature, Right: Low Temperature	51
Figure 2.32 The prediction of full-restraint stress of CSA concrete with/without LA. Left: High Temperature, Right: Low Temperature.....	52
Figure 2.33 Full-restraint stress development of MgO concrete with varied mix proportions	54
Figure 2.34 Stress development and free deformation of Type-II MgO concrete.....	55
Figure 2.35 Comparison of free expansion of type-II MgO under varied temperature conditions	57
Figure 2.36 Color change from yellow to light green as an indicator of neutralization (After Wikipedia).	58
Figure 2.37 Measurement of TEC using TSTM.....	59
Figure 2.38 Stress development of MgO concrete and CSA concrete under wetting/drying cycle	61
Figure 3.1 An example of computed moisture state in a random pore size distribution profile	65
Figure 3.2 Overall flow of the multi-scale model	67
Figure 3.3 The nonlinear coupling of the thermo-hygro-mechanical model.....	68
Figure 3.4 Homogenous nucleation of outer products (Hydration Degree:0, 0.72, 0.85).....	75
Figure 3.5 Heterogenous nucleation of outer products (Hydration Degree:0, 0.72 and 0.85)	75
Figure 3.6 Porosity deviation of homogenous case	76
Figure 3.7 Comparison of the heterogenous case with the experiments	77
Figure 3.8 A two-dimensional slice of homogenous (left) and heterogenous case (right), with hydration degree=0.72.....	77
Figure 3.9 Left: Computed amount of chemical component; Right: Pixel numbers of both cases.....	78
Figure 3.10 Schematic diagram of simulated densification	79
Figure 3.11 Computed pore size distribution with varied w/c using densification model (Age=60 days)	80
Figure 3.12 Left: Porosity of cement paste (w/c:0.5) tested by NAD, after (Ma and Li, 2013). Right: Derivative plot (w/c:0.5) tested by NAD, after (Zeng <i>et al.</i> , 2016).	82

Figure 3.13 Schematic representation of combined effect between densification and expansion	85
Figure 3.14 Fitting curve and computed densification rate with varied w/c and hydration degree	87
Figure 3.15 Flow chart of the computation of the pore structure development	88
Figure 3.16 Computed Mass ratio of LD and HD CSH in the proposed model (Left: w/c:0.30; Right: w/c: 0.50)	89
Figure 3.17 Loosely-packed CSH found by TEM image (After (Mathur, 2007))	89
Figure 3.18 Computed volume of two groups of C-S-H under for varied w/c under normal temperature	92
Figure 3.19 Validation of capillary porosity (left) and surface area (right) through a variety of studies...	93
Figure 3.20 A schematic diagram of correlation between densification and volume expansion (Modified from (Ioannidou, Kanduč, <i>et al.</i> , 2016))	94
Figure 3.21 Relationship between measured surface area and total pore volume by NAD test.....	95
Figure 3.22 Relationship between measured surface area and finer pores by NAD test.....	95
Figure 3.23 Pore size distribution of nitrogen-accessible pores. Left: w/c=0.3, Right: w/c=0.5.	96
Figure 3.24 Effect of temperature on the surface area development of cement paste.....	97
Figure 3.25 The Relationship between measured surface area and total pore volume (HighTemp).....	97
Figure 3.26 The pore structure of OPC, MgO and CSA paste samples measured by MIP.....	98
Figure 3.27 Fine pores of OPC, MgO and CSA paste samples detected by NAD tests.....	99
Figure 3.28 A new proposal of three-dimensional nanostructure of C-S-H.....	101
Figure 3.29 A multi-scale schematic diagram of C-S-H structure	102
Figure 3.30 Multi-cycle MIP on sealed-curing paste with w/c:0.45 (after (Kishi and Yoshida, 2008))..	103
Figure 3.31 Development of Pore Structure and Moisture State for OPC, MgO and CSA concrete.....	104
Figure 3.32 Hysteresis behavior of the 1 mm-thick C ₃ S sample during drying (After (Grudemo, 1979))	106
Figure 5.1 Modelling of Cracking Frame	111
Figure 5.2 Creep and Free shrinkage in Kovler's Method	114
Figure 5.3 Before activation of adjustment	115
Figure 5.4 After activation of adjustment.....	115
Figure 5.5 Experimental data on displacement restoration process (Left); Virtual evolution pattern if machine stiffness is doubled (Right).....	117
Figure 5.6 The large discrepancy on measurement of specific creep using different TSTM devices (Kovler, Igarashi and Bentur, 1999; Tao and Weizu, 2006)	118
Figure 5.7 Validation of hydration heat model on adiabatic temperature rise	119

List of tables

Table 2.1 Materials Type and Density.....	24
Table 2.2 Chemical composition of OPC cement	25
Table 2.3 Chemical component of CSA	25
Table 2.4 Mix Proportions for TSTM Experiment.....	25
Table 2.5 Compressive strength of different mix proportions (1D, 3D, 7D and 28D).....	26
Table 3.1 Density of Reactants and Products (g/cm ³) used in the Mic Model.....	74
Table 3.2 Properties of compounds and hydrates	83
Table 3.3 Experimental factors.....	90
Table 3.4 Nitrogen-accessible surface area for varied w/c and drying condition cured at 22 °C.....	91
Table 5.1 Mix Proportions for OPC and SF concrete used by two studies	117
Table 5.2 Concrete mix proportions in adiabatic temperature test.....	118

1. INTRODUCTION

1.1 Background

1.1.1 Early-age Cracking

Early-age cracking of concrete can significantly jeopardize the durability performance of concrete structures in a long term. Once these early-age cracks are initiated and propagated, it greatly accelerates the deterioration of concrete structures at later age, through easier penetration of a variety of aggressive substances (e.g., water, chlorides, sulphates and carbon dioxide) and is accompanied by the corrosion of embedded reinforcement. It may further result in premature failure or even collapse of concrete structures. The early-age cracking problem is not always been paid with enough attention because sometimes it does not impose any visible effects in a short term, nevertheless, if treated carelessly, the propagation and widening of these cracks could result in costly repairing and maintenance at later stages, which is sometimes estimated to be several times of the initial construction cost, along with huge energy consumption.

It is shown in Figure 1.1 that, varied types of early-age cracking exert great impacts on the durability performance of the structural over the whole service life. If these early-age cracks are well controlled at the initial period, the rapid propagation period of cracks can be retarded, beneficial to both the safety and durability of the structure.

Strength and workability of concretes have been assumed to prevail in the past design concepts for consideration of safety and serviceability. While for contemporary concrete structures, apart from required strength and fresh properties, the durability performance-based designs call for a comprehensive understanding on the cracking and deterioration mechanisms, which highlights the structural performance over the entire life span (Maekawa, Chaube and Kishi, 1999; Maekawa, Ishida and Kishi, 2009). This design strategy has more economical and environmental-friendly outcomes. It does not only focus on the initial construction cost, but also underscores the improved durability performance in a long term. In consideration of this scheme, the design of concrete material with minimum early-age cracking sensitivities will be a preliminary but also fundamental step for better long-term performances. It could decelerate the deterioration process and extend the life span of concrete structures.

The early-age cracking problems has been widely and intensively studied since 1990s (R. Springenschmid, 1994) due to its enormous engineering significances. Cracking mitigation techniques like using low-heat cements, shrinkage-reducing agents (SRA), varied types of

1. INTRODUCTION

expansive additives (calcium sulfoaluminate type or magnesium oxide type) have been developed and advanced to mitigate the cracking sensitivity of concrete in the past decades. However, owing to the dynamical and complex evolution of the strain and stress fields during early-age hydration, the applicability and effectiveness of these upcoming new materials/mix designs are still questionable and not fully understood, which remain as tough and daunting tasks for researchers and engineers. Especially, it has been found that the commonly-used expansive additive, like the calcium sulfoaluminate type (CSA type) and slag-blended concrete fail to compensate the rapid thermal shrinkage during semi-adiabatic temperature conditions (Lin, 2006; Lim, Lin and Kishi, 2008).

In most of the countries (e.g., Japan and China), the experience-oriented methods are adopted on site for usage of different admixtures or mix designs. But such empirical methods may not always be effective, since the engineering conditions (including varied temperature conditions and restraint degree) of the concrete structures will vary from one to another. Moreover, without theoretical understanding or adequate experimental technique to quantify the cracking sensitivity of concrete, it is difficult to optimize the mix design for vastly different engineering conditions. Therefore, in order to provide practical solution and guidance, it is crucial for us to both experimentally examine the strain and stress development of contemporary concrete materials and numerically model its cracking performance.

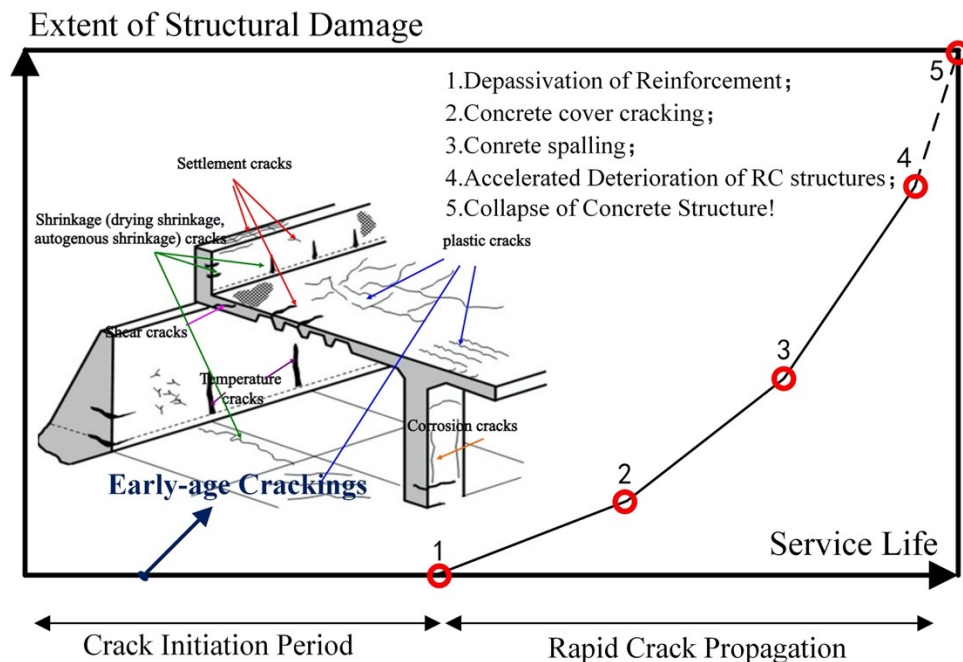


Figure 1.1 Impact of early-age cracking on life span of concrete structures, corrected from (*Non-structural Cracks in Concrete, Cement and Concrete Society, United Kingdom, 1978*)

1. INTRODUCTION

1.1.2 The Coupled Thermo-hygro-mechanical Process during Hydration

The hydration of cement greatly determines the early-age transformation of concrete from a viscous suspension to a porous load-bearing media. The interacted chemical and physical processes during hydration, coupled with the environmental condition (e.g., varied temperature and humidity field, restraint degree of the concrete members), result in rather complicated early-age stress evolution of cement-based materials. Since the volume changes during early age will be partly or fully restrained according to different boundary conditions in-situ, the stress build-up or stress relaxation of concrete may create residual stress that reduces structural members' load-carrying capacities or cause early-age cracking. Therefore, early-age stress evolution process plays a crucial role in the initiation and development of thermal cracking in concrete. In the following sections, the primary factors governing the early-age cracking problem will be discussed.

1.1.2.1 Heat of Hydration

Heat of cement will be generated after cement powders are mixed with water, which leads to temperature rise of the concrete. If the generated heat cannot dissipate into environment easily, it could lead to a temperature increase up to ~ 70 to 80 °C, e.g., massive concrete structures like dams, thick transfer slabs or large structural components of substructure. When this generated high temperature starts to decline, a considerable thermal shrinkage will be induced. Supposed this thermal shrinkage is restrained by the boundary condition (e.g., two end fixed beam), tensile stress develops. Once this tensile stress exceeds the tensile strength of concrete, it brings about the thermal cracking of concrete.

1.1.2.2 Autogenous Shrinkage

When un-hydrated cement particles contacts with water, hydration products will be formed inside the pore system. Chemical shrinkage is defined as the absolute volume change in hydration products from un-hydrated cement and water (Tazawa *et al.*, 2000). Generally, this amount will be 6-7 ml/100 g of reacted cement. When cement paste is still in a liquid phase, the chemical shrinkage is totally converted into external volume change. Once the hydrates percolate and the solids are formed inside the larger pores, the formation of water-vapor meniscus will also be present (Lura, Jensen and Van Breugel, 2003). The relative humidity (RH) of the whole system will also drop, signified by the physical phenomena called self-desiccation. It also leads to the change of saturation condition inside the pore structure, mainly governed by Kelvin-Laplace law. Herein, the definition of the autogenous deformation conforms to that proposed by JCI standard (Tazawa *et al.*, 2000):

- Autogenous deformation: The bulk deformation of a closed, isothermal cementitious material system not subjected to external forces.
- Chemical shrinkage: Absolute volume reduction associated with hydration reactions in a cementitious shrinkage, generally accompanied by self-desiccation (Luan and Ishida, 2013).

1. INTRODUCTION

At this very early-age of hydration, the stiffness of cement paste is so low that any slight stress applied on the system will form a large deformation. Thus, noted that in the modeling of autogenous shrinkage of the current study, only the shrinkage after setting of concrete will be computed. Also, this portion of deformation can be measured experimentally and compared with the model.

1.1.2.3 Artificial Expansion by Addition of Expansive Additives

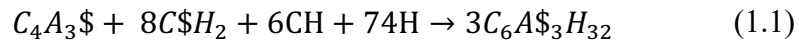
Generally, the expansive additives are added into the concrete to compensate shrinkage of concrete. It is expected that once this shrinkage is reduced effectively, the tensile stress development can be mitigated and cracking sensitivity also lowered accordingly. Currently, there are two major types of expansive additives used in Japan. The calcium sulfoaluminate type additive (CSA) and the free-lime-expansive additive (FLE). Recently, another new type of expansive material magnesium (MgO) has also gained more attention (Mo *et al.*, 2014), which has been used in more than 30 dam structures in China.

1) CSA-type Expansive Additive

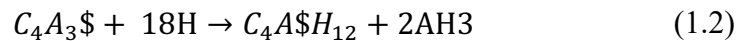
For CSA type, it mainly composes of $C_4A_3\$$ (termed as Hauyne or Ye'elimite), f-CaO (or free lime), C\$ (or anhydrite). It was pointed out that, the reactants of CSA reacts with water and form ettringite, whose density is half of the reactants, and thus forming very loose structure and occupies a large pore volume. The FLE type additive mainly generate calcium hydroxide ($Ca(OH)_2$) to occupy the volume and the density of calcium hydroxide is also around half of the reactants. The CSA type will be discussed and modeled in this study. The FLE type and CSA type share some similar characteristics: (1) The formation of loose and low-density structure (2) The reaction needs a relatively high amount of water, which is around 0.85-0.90 g for full hydration of per gram of unreacted CSA additive. The main stoichiometric reactions for CSA are listed as follows (Chen, Hargis and Juenger, 2012):

- Reaction of Hauyne

- Reaction of Hauyne to produce ettringite:



- Reaction of Hauyne to produce monosulfate:



- Reaction of Lime:

- Reaction of Lime to produce portlandite:



- Reaction of Anhydrite:

- Reaction of Anhydrite to produce gypsum:



Where $C_4A_3\$$, $C\$H_2$, CH, H, $C_6A\$_3H_{32}$ denotes Hauyne, gypsum, calcium hydroxide, water and ettringite, respectively. $C_4A\$H_{12}$ and AH_3 mean monosulfate and aluminum hydroxide, respectively. C represents calcium oxide and C\$ is the anhydrite.

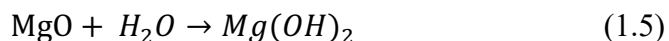
1. INTRODUCTION

Even though its expansion is considered by many researchers to be greatly associated with the formation of loose reaction products, e.g., ettringite (Cohen, 1983a, 1983b; Flatt and Scherer, 2008), the actual mechanisms of the expansion are still controversial up to now. Several possible mechanisms are summarized as:

- The production or precipitation of ettringite results in the increase of solid volume (Polivka, 1973). However, it is argued that there is a lack of evidence to correlate the amount of ettringite with the expansion (Taylor, Famy and Scrivener, 2001). According to Mehta (Mehta, 1972), it is also pointed out that the expansion fails to be directly accounted by the increased volume of solids, on the basis of stoichiometric equations. Moreover, the formation of other hydrates (especially C-S-H) will also increase its solid volume, but their formation is not taken as the source of expansion.
- The expansion is related to the adsorption of water by the colloidal sized ettringite crystals (Mehta, 1973). But it was also argued that crystalline ettringite will not show gel-like swelling behavior and such behavior has not been reported for synthetic specimens (Bizzozero, Gosselin and Scrivener, 2014).
- Expansion can be ascribed to the formation of crystallization pressure when ettringite crystals are generated (Bizzozero, Gosselin and Scrivener, 2014; Kolneath, 2021). This theory emphasizes the role of saturation degree of the solution. Supersaturation is considered to be the driving force for the development of crystallization pressure.

2) MgO-type Expansive Additive

In terms of MgO-type expansive additive, the stoichiometric reaction can be expressed by Eq. (1.5).



For a long time in the past, the content of MgO has been limited in many specifications due to the excessive amount of long-term delayed expansion. It was found that several bridges in France with 16-30% of periclase added into the concrete had been damaged by this delayed expansion. In Germany, the city hall of Kassel was also found to be destroyed due to the same reason. Since then, the content of MgO has been limited to be less than 5.0% in China (Standard, 2009) and UK (Standard, 2007), 6.0% in USA (Standard, 2012).

In 1970s, the Baishan concrete dam structure in China had surprisingly shown no cracks even without taking any temperature-control countermeasures (e.g., cooling pipes) to control thermal shrinkage. As a consequence, a series of research on the preparation and expansion behaviors of MgO-based expansive additive had been subsequently conducted. It has been reported that mystery of the beneficial expansion or deleterious expansion relies heavily on the calcination condition (Mo, Deng and Tang, 2010). Carefully calcined MgO (temperature: 900-950 °C) possesses the beneficial potential for shrinkage compensation, whereas if the clinkering temperatures reaches up to or above 1400 °C, MgO will become dead-burnt and show very low reaction rate (Mehta, 2009). This kind of dead-burnt MgO will lead to delayed expansion, this

1. INTRODUCTION

expansion occur at very late time and may lead to harmful expansion to the structure. Therefore, generally MgO with much lower calcination temperature from 900 to 1200 °C is used to produce the MgO-based expansive additive. The lightly-burnt MgO produced from lower calcination temperature and shorter time has higher reaction activity and expands earlier (Lingling and Min, 2005). While for dead-burnt MgO, much slower and smaller expansion takes place in early age with larger expansion at later age. Especially, due to the tunable expansion property by various calcination conditions, a gradient of MgO can also be produced for different engineering purposes accordingly. The relationship between the expansion property and its calcination condition is shown in the schematic representation in Figure 1.2. The source of MgCO_3 normally comes from Magnesite or Dolomite.

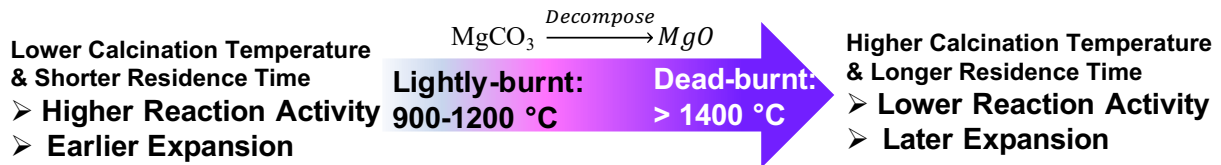


Figure 1.2 Calcination Temperature and Expansion Property

Nowadays, in China, more than 30 concrete dams have been constructed using MgO, with ~40 years of experiences for preparation of properly-tailored MgO (Even though most of the relevant papers/specifications are published in Chinese). In comparison with CSA-type, several important features of MgO-type expansive additives are listed as follows:

- The customizable expansion properties of MgO: The expansion activation time can be tuned according to the engineering purposes.
- Much less amount of water is needed for complete hydration: It enables MgO to expand even under non-wet or sealed condition. According to Eq. (1.5), around 0.45 gram of water is needed for the complete hydration of per gram of MgO expansive additive.
- Slower, smaller but longer-term expansion: Generally, expansion of CSA-type mostly ceases within 7 days due to high demand for water, but lightly-burnt MgO can expand until several months (Mo, Deng and Tang, 2010).

1.1.2.4 Drying Shrinkage and Creep

In comparison with autogenous shrinkage, drying shrinkage is generated by water evaporation when concrete specimen is exposed to the external environment. When drying is taking place, evaporable water will gradually be lost from large capillary pores first. When RH decreases to very low value, e.g., <10%, even interlayer water will be lost (Maekawa, Chaube and Kishi, 1999). Drying shrinkage is very common cause of volumetric shrinkage in hardened concrete materials. It is well-acknowledged that low w/c concrete has higher autogenous shrinkage, while for drying shrinkage, generally high w/c concrete has higher drying shrinkage, since more evaporable water is left inside concrete, and the loss of the evaporable water will lead to the shrinkage (Ishida and Chaube, 1997).

1. INTRODUCTION

Creep is discussed together with drying shrinkage, since the cause that affects drying shrinkage will also affect creep generally. It has been pointed out that when a hydrated cement paste is subjected to a sustained stress, a large amount of physically absorbed water will be lost, this part of lost water results in the creep in concrete. Both drying shrinkage and creep are related to loss of water inside the pore structure of cement-based materials, and the difference is that: for drying shrinkage, water is lost due to the humidity gradient between external environment and the concrete inside, while for creep phenomenon, the water movement is related to applied stress. Additionally, the strain-time relationship of drying shrinkage and creep is found to be quite similar (Mehta and Monteiro, 2006). The creep phenomena, however, has been very complex and intriguing. It still remains as one of the most heated topics, though it has been studied for decades. The visco-elastic and visco-plastic properties render the realistic deformation and stress quite hard to be predicted accurately, no matter for macroscopic behavior and microscopic behavior. The basic creep has been termed as the time-dependent deformation when concrete is subjective to the load under sealed condition. While drying creep is the phenomena that another part creep will take place in addition to basic creep when drying happens. The total creep is the summation of these two. In this study, only the early-age creep effect is discussed, which does not involve the long-term creep effect that generally associates with the drying and sustained load (Bažant, 1988). Early-age creep effect is induced by self-induced stress when the early-age deformation is restrained. It is quite pronounced in the transformation process of hydration from liquid-like suspension to the solid state, especially for expansive concretes. It has become a formidable problem for both researchers and engineer to understand to which extent the elastic stress is relaxed and furthermore, to predict stress development and cracking in early-age concrete (Bažant, 2001).

1.1.2.5 Total Free Deformation

The total free deformation of concrete can be decomposed into several parts: Thermal deformation, autogenous shrinkage, drying shrinkage, artificial expansion (which is expansion due to the addition of expansive additives). The decomposition is given in the Eq. (1.6).

$$\epsilon_f = \epsilon_{th} + \epsilon_a + \epsilon_{dry} + \epsilon_{EA} \quad (1.6)$$

Where ϵ_f , ϵ_{th} , ϵ_a , ϵ_{dry} , ϵ_{EA} denote strain values (non-dimensional) of free deformation, thermal deformation, autogenous shrinkage, drying shrinkage and artificial expansion caused by expansive additive, respectively. When the specimen is cured under sealed condition, drying shrinkage is eliminated, and the following Eq. (1.7) holds true:

$$\epsilon_f = \epsilon_{th} + \epsilon_a + \epsilon_{EA} \quad (1.7)$$

1.2 Review on Experimental Techniques

Up to now, there are several experimental methods to evaluate the cracking sensitivities of cement paste/mortar/concrete materials. In this section, a systematic review on the benefits and

1. INTRODUCTION

disadvantages of each of these commonly used methods will be unfolded. Among them, the role and significance (both from the perspectives of research and engineering) of a temperature stress testing machine (TSTM) will be emphasized, which is served as an ideal tool for quantitative evaluation of early-age deformation and stress (R. Springenschmid, 1994; Lin, 2006; Nguyen *et al.*, 2019a).

1.2.1 Determination of Free Strain using Length Comparator

The ASTM C157 standard test method can be used to determine the length changes that are produced by causes exclusive of applied external forces or temperature changes (ASTM, 2017). In this standard method, the length change of the specimen at specific time can be recorded and compared to derive the free strain of the specimen. This method can be used for cement paste/mortar/concrete specimens. The advantage is the very easy operation. But the early-age deformation before demolding (generally one day) could not be captured. A photo for this method is given in Figure 1.3 (a).



Figure 1.3 (a) Experimental set-up for ASTM C157 standard (b) ASTM C1698 standard

Another similar standard test method for autogenous strain is the ASTM C1698 (ASTM, 2019), which also utilizes the length comparator for length determination. The cement paste/mortar is casted into a corrugated plastic tube, as shown in Figure 1.3 (b), with one end fixed and the other connected to a displacement sensor. The disadvantage of this set-up is that it could not measure the deformation of concrete, but only cement paste or mortar. Additionally, the drying shrinkage cannot be measured, since the specimen is sealed by the plastic tube.

1.2.2 Determination of Restrained Deformation and Restrained Stress

1.2.2.1 Dual Ring Test

One common standard method for evaluating the restrained deformation is using the dual ring test (ASTM, 2004; AASHTO, 2017). The degree of restraint is achieved by the dual steel rings, between which the cement paste/mortar/concrete is casted into. This method is able to quantify the restrained deformation, but the temperature history due to the hydration heat of the material itself cannot be considered. Also, the restraint degree is fixed, which is attributed only to the

1. INTRODUCTION

stiffness of the steel ring. Photos of this set-up with cover or without cover is shown in Figure 1.4(a) and Figure 1.4(b), respectively.



Figure 1.4 (a) the covered dual ring and (b) the uncovered dual ring

1.2.2.2 Cracking Frame

Beside the aforementioned conventional methods, the uniaxial restraint test is considered as a more useful and reliable method, which has been developed for the past three decades. The design of cracking frame provides a high degree of restraint to the specimen in one dimension (the longitudinal direction). Two T-shaped crossheads were firmly held by the steel frame. Deformation of the invar bar is used to measure the longitudinal stress (Since invar steel has very low thermal expansion coefficient, i.e., $\sim 1.2 \mu\epsilon/^\circ\text{C}$). The formwork can be designed to be an insulated one which offers certain extent of insulation effect. But the cracking frame cannot simulate the condition of varied restraint degrees. The very strict criteria for early-age cracking under a full-restraint degree is not able to be achieved. Also, even though insulation materials are used for the formwork, the high temperature rise condition cannot be fulfilled due to the lack of a temperature control system (e.g., a heater). The schematic representation of a cracking frame is given in Figure 1.5.

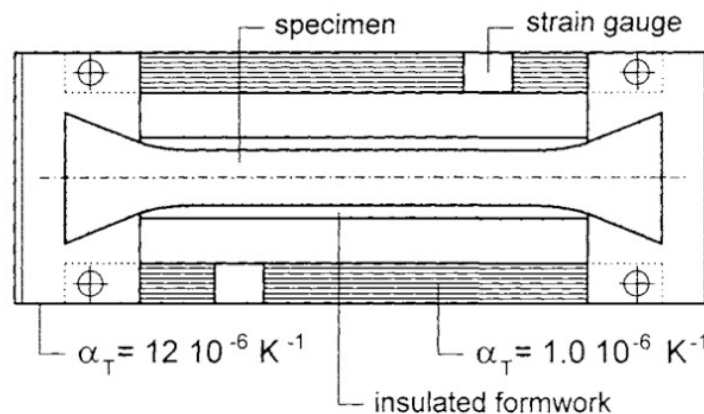


Figure 1.5 Schematic representation of a rigid cracking frame (Springenschmid, 1998)

1.2.2.3 Temperature Stress Testing Machine

Temperature Stress Testing Machine (TSTM) is regarded as the most effective and powerful evaluation tool for early-age behaviors (R. Springenschmid, 1994; Lin, 2006; Nguyen *et al.*,

1. INTRODUCTION

2019a). It can simulate the semi-adiabatic temperature rise condition caused by the hydration of each mix proportion, test the restrained stress/deformation under varied restrained degree, and evaluate the development of other mechanical/physical properties including elastic modulus and thermal expansion coefficient, etc. However, to design a proper and accurate testing system, a well-considered and proper mechanical design, signal conditioning, displacement control, measurement and automation programing are all required. Since at the early-age, the concrete materials will witness drastic change from semi-liquid state to the solid state, along with the change of its thermo-hygro-mechanical properties, this complexity also hinders its development and practical application. The reliability of TSTM developed in different institutions may also vary largely due to theoretical biases or inappropriate design. In principle, given the same mix proportion, thermal insulation, restraint and curing condition, experimental results from TSTMs in different institutions should yield reproducible results.

In 1984, Gierlinger and Springenschmid (R. Springenschmid, 1994) developed the first TSTM with a closed-loop system, which has been used to discuss about the thermal behaviors mainly. Subsequently, due to its crucial role in quantifying early-age behaviors, various types of TSTM have been developed worldwide even until now, including the Kovler's TSTM (Kovler, 1994), Mizobuchi's TSTM (Mizobuchi, 1998), Delft TSTM (van Breugel, 1999), Altoubat and Lange's TSTM (Altoubat and Lange, 2001), Maruyama's TSTM (Maruyama, 2003), Tsinghua TSTM (Lin, 2003), the UTokyo TSTM (Lin, 2006), UQ TSTM (Nguyen *et al.*, 2019a), etc. A more detailed history review and discussion on the for and againsts of each machine can be referred to the thesis (Lin, 2006).

The UTokyo TSTM has been previously constructed to quantify cracking sensitivities of mixtures with varied types of cement (OPC or rapid hardening cement), types of aggregates (light-weight or normal aggregates), SCMs (fly ash or slag) successfully, yielding reliable testing results and good reproducibility (Lin, 2006; Lin and Kishi, 2006; Lim, Lin and Kishi, 2008). The outline of the UTokyo TSTM (Version 1.0) is shown in Figure 1.6.

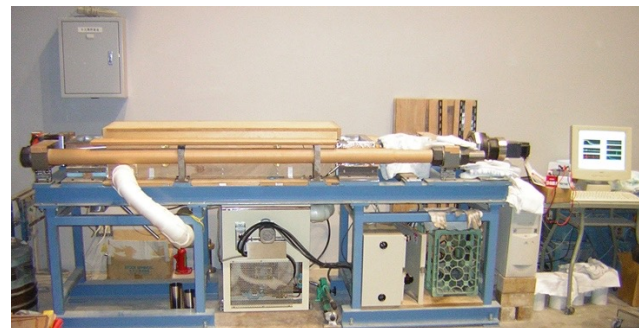
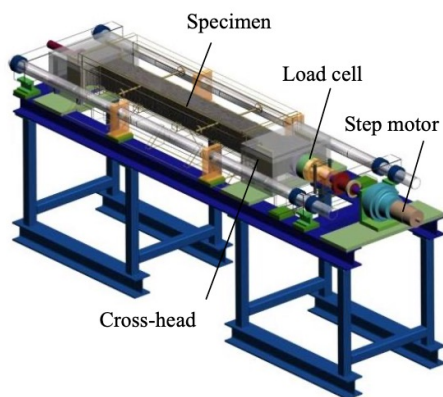


Figure 1.6 Outline of UTokyo TSTM (Ver. 1.0)

1. INTRODUCTION

On account of the viability and excellent performance of UTokyo TSTM (to the author's knowledge), it is used as the main experimental technique. In this study, several modifications on the UTokyo TSTM are also made, with updated features (Version 1.1) discussed in the next section. It is used in the current study to conduct experiments on free deformation, restrained stress, thermal expansion and optimization of mix designs.

1.3 Research Significance and Objective

The cracking problem on-site leads to reduction of safety margin and deterioration of durability performance of concrete structures in a long term. To prevent cracking in practice, the effective use of expansive additive under various engineering conditions (temperature and restraint condition) is of great importance. It requires reliable and effective testing method, along with deeper understanding on the mechanism of expansion. In this study, it aims to both experimentally and analytically study the effectiveness of expansion concrete on compensating shrinkage. The experimental data and analytical model can offer us insights on the reason of ineffective expansion and practical solutions for it. It can provide some guidance on the optimization of mix design in practice.

To achieve this goal, it consists of one experimental objective and one analytical objective. The experimental objective aims to comprehensively study the deformation and stress development OPC concrete, a type of commonly-used expansive concrete (CSA concrete) and a type of relatively new expansive concrete (MgO concrete). Well-designed TSTM (temperature stress testing machine) is used as a reliable and effective experimental to evaluate and compare their cracking performances under varied temperature and restraint conditions.

The analytical objective consists of two parts: (1). It attempts to understand the mechanism of ineffective expansion of CSA concrete under high temperature condition, which has also been found in the realistic construction sites. By a coupled thermo-hygro-mechanical model, the pore structure development and the moisture state inside can be quantified, which offers us significant insights on the reason of ineffective expansion. (2) This study also provides a numerical method to quantify the deformation and stress development of OPC and CSA concrete. The modeling of these properties is a difficult task, which is associated with the temperature condition, the pore structure development and the moisture state inside these pores. Therefore, it requires a coupled model to comprehensively understand the thermo-hygro-mechanical process during hydration. It highlights the necessity of modeling the pore structure of CSA concrete, so that the moisture state inside can also be evaluated reasonably, which turns to be linked with the expansion properties.

1. INTRODUCTION

1.4 Outline of Dissertation

Chapter 1 offers a brief review on the background information of varied types of expansive additive, and varied types of deformations (like thermal deformation, autogenous shrinkage, artificial expansion and drying shrinkage). It is followed by a discussion on advantages and disadvantages of various experimental techniques used for deformation and stress development.

Chapter 2 discusses the features and working principles of TSTM. Then, the experimental scheme using TSTM will be introduced. It is followed by experimental results and the analysis on OPC, CSA and MgO concrete. A constitutive relationship which can transform the deformation into stress is proposed. This chapter focuses mainly on the macroscopic behavior of concrete materials. For the modeling of deformation and stress development of CSA concrete, it is resolved by a newly proposed concept of free water availability.

Chapter 3 formulates a coupled thermo-hygro-mechanical model. A new pore structure model is proposed and implemented into the coupled model, which forms as the basis for quantification of moisture state inside pores. Then the pore structure of CSA is also modeled, so that the reason for its ineffective expansion could be analytically studied.

Chapter 4 is the conclusions and future perspective of this study.

Chapter 5 is the appendix. The appendix offers us a more rigorous and comprehensive mathematical derivation on of working principles of cracking frame, TSTM and the Kovler's evaluation method on early-age creep (enhanced after Lin, 2006). The prediction of adiabatic temperature is also attached, which successfully reproduces important outcomes of the hydration heat model in DuCOM (Kishi, 1999). The porosity computed from some recently reported bulk density is attached as well.

2. Early-age Deformation and Stress Development

2.1 Experimental Device-TSTM

2.1.1 Overall Design

In the previous chapter, by a comparison with other experimental techniques, the significance of TSTM on the evaluation of early-age thermo-hygro-mechanical behaviours have been pointed out. In this section, basic features of the Utokyo TSTM used in this study will be unfolded, more detailed design can be referred to the Utokyo TSTM Ver. 1.0 (Lin, 2006).

The specimen has a dimension of $120\text{mm} \times 120\text{mm} \times 1200\text{mm}$. And thus, the slenderness ratio of the specimen is 10:1, meaning that the free deformation in the longitudinal direction is much larger than other directions. To push/pull the specimen with sufficient grip, two T-shaped crossheads are used at the ends of the specimen, as shown in Figure 2.1. One crosshead of the specimen is attached to the fixed end, which has been firmly constrained by steel frame with high stiffness. The other crosshead is the movable crosshead, and its movement can be controlled by the connected computer system. Two load cells are installed in two ends of the specimen, the free end and the fixed end. The specimen is surrounded by a chamber, in which the temperature is controlled by a heater and refrigerator. Hot or cold air is circulated inside the chamber to simulate varied temperature rise conditions. The movable crosshead is pulled or pushed by a differential twin-screw mechanism. The step speed and speed reducing ratio can be controlled by the PC, in this study, a minimal displacement of $0.01\text{ }\mu\text{m}$ for one rotation step of the electric motor is used.

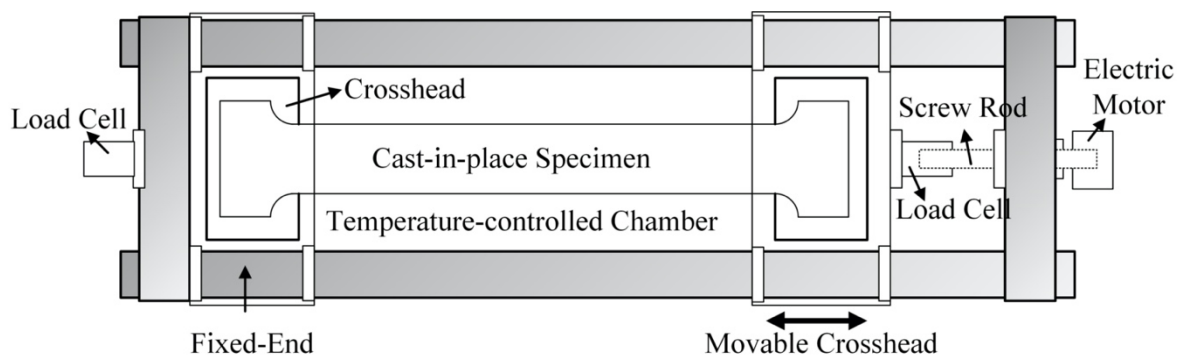


Figure 2.1 Overall Design of the Utokyo TSTM

2. Early-age Deformation and Stress Development

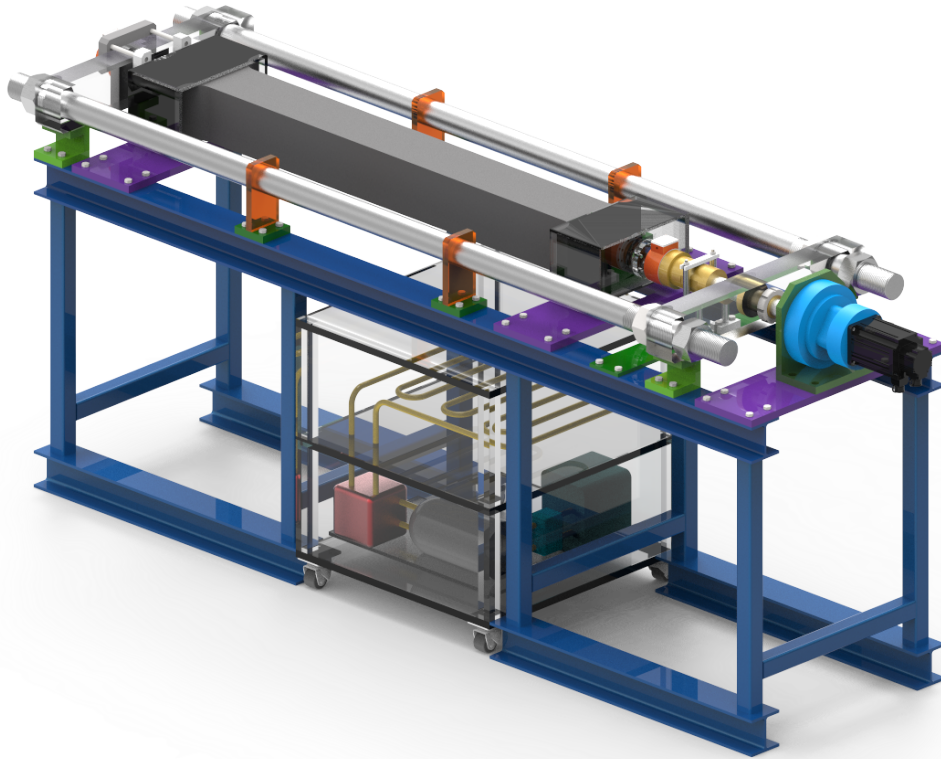


Figure 2.2 3D model of Utokyo TSTM Ver. 1.1 (model built in SolidWorks and rendered by KeyShot)

For clear depiction of some details, a rendered three-dimensional model is also shown in Figure 2.2.

2.1.2 Sensors, Load Cell, Heater and Refrigerator

2.1.2.1 Temperature Sensor

From Ver. 1.0 to Ver.1.1, the original four old temperature sensors are replaced by new types of smaller and more accurate temperature sensors (Pt 100, R610-3 from the CHINO company) with a diameter of 1.6 mm only, and a length of 23 mm only. The smaller size can guarantee that the embedded sensors inside the concrete will not cause significant loss of the cross section, so that the concrete will not preferentially crack at the cross section where we embed the sensors.

2.1.2.2 LVDT Displacement Sensor

The accuracy of displacement sensors is of crucial role, since the restraint condition is achieved by displacement control. Highly sensitive displacement transducer (CDP-5 from the Tokyo Measuring Instrument Lab) is used.

2.1.2.3 Load Cell

The load cells (TCLM-50KNB) at both ends have a capacity of 50KN (sufficient for concrete materials), and a resolution of $2.5\text{mV/V} \pm 0.5\%$.

2. Early-age Deformation and Stress Development

2.1.2.4 Heater and Refrigerator

The heater and refrigerator will generate hot or cool air to circulate quickly inside the temperature-controlled chamber to achieve semi-adiabatic temperature condition. The program can control the temperature compensation effect based on user's definition. In order to simulate a high temperature rise condition (or semi-adiabatic temperature condition), generally the air inside the chamber should trace the temperature of the specimen with difference of around 0.1 degree Celsius only. The outer formwork is made by wood, with several cm thick of polystyrene for insulation purposes. Even though the current set-up cannot achieve perfect insulation condition (with gaps existing between the formwork and the frame, etc.), it is sufficient to simulate the semi-adiabatic temperature condition caused by the heat of hydration of the mixture.

2.1.3 *Design of Friction Reduction*

Several friction reduction designs are implemented. Firstly, the support which sustains the weight of the specimen is designed to be roller support. Secondly, the detachable mould is used. That is to say, after the specimen is hardened, the mould can be detached by a screw mechanism, and thus, the side and bottom moulds could all be detached from the specimen to reduce the friction to the minimum level, with the self-weight of the specimen resting on three roller supports only. Thirdly, the crosshead is also resting on a roller support system, which facilitates the smooth forward and backward movement.

2.1.4 *Measurement and Automation*

There are totally five sections of the measurement and automation: Sensors, Signal Conditioning, DAQ (data acquisition) interface and the computer (PC). The schematic representation clearly depicts how these five sections are connected and interacted with each other, as shown in Figure 2.3. The signal conditioning block and data acquisition interface is mainly responsible for conversion of the digital signals from the sensors to the analog signal, so that an interaction of the close-looped system can be achieved. The computer system is also updated as a Windows 10 system from the previous XP system. Since there will be incompatibility between the original signal conditioning block, DAQ interface and a new Windows 10 system, the original DAQ interface PCI-6036E is also upgraded and replaced by a PCIe-6341 from the National instrument (NI) Company. Additionally, it is found out that data acquisition is much more stable with a RAM ≥ 16 GB, while when RAM is only 8 GB, data loss sometimes happens. The control program in the PC is using NI MAX and LabVIEW 2018, for the reason of compatibility between old devices and new system. Furthermore, other convenient features like remote access, real-time monitoring and control can also be implemented. The front panel of the program and the real-time remote control can be seen in Figure 2.4.

2. Early-age Deformation and Stress Development

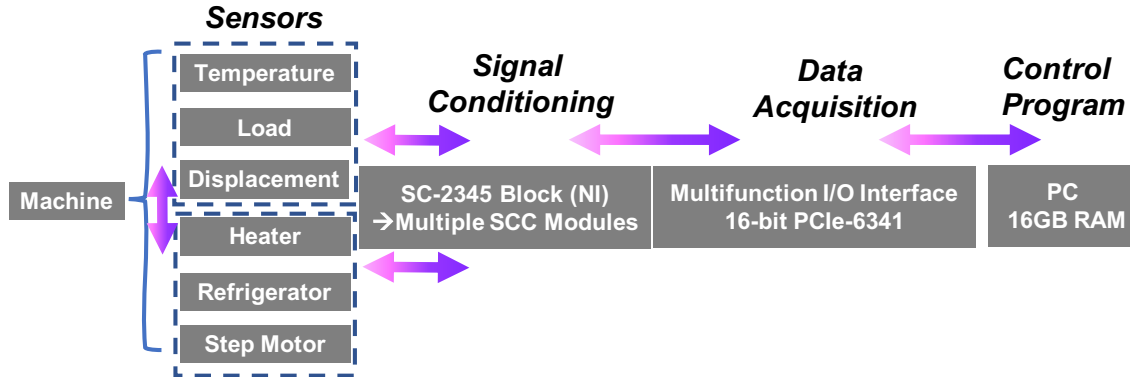


Figure 2.3 Measurement and automation of Utokyo TSTM (Ver. 1.1)

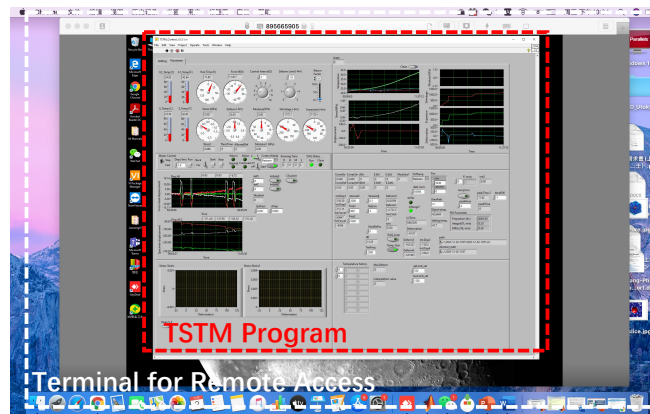


Figure 2.4 Real-time remote access and control (Ver. 1.1)

2.1.5 Displacement Control System

The movable crosshead is controlled in the displacement mode in order to achieve precise control and fulfill different restraint degrees. Differential screw mechanism is used to achieve tiny relative displacement between nuts. As for modification to Ver. 1.0, the screw rod which pushes and pulls the specimen is redesigned to the length of 360 mm, which is able to detect larger displacement while maintaining required stiffness. The thread pitches between the twin-screw has been changed to be 4.5 mm and 4.0 mm, respectively. In other words, by rotating the screw rod for one circle, the actual displacement applied on the cross head will be 0.5mm. In this way, the precise displacement control can be achieved. The minimal displacement for one rotation step of the step motor will be $0.01 \mu\text{m}$, and the minimum controllable displacement of the system will be $0.5 \mu\text{m}$, which has been proven to be accurate enough for the simulation on any restraint degrees (Lin, 2006). Please noted that, another proof for the required minimum displacement control can also be testified by the restrained stress. One can easily envisage that, higher accuracy will lead to smoother restrained stress development, and vice versa. In the later discussion of experimental results, it will be shown that the experimental results for stress development curves are adequately smooth.

2. Early-age Deformation and Stress Development

Currently, there are mainly two ways for measuring the displacement of the specimen.

- Two LVDT sensors are installed to measure the relative displacement of two sides of the movable crosshead, i.e., the Dc-1 and Dc-2. Then, the average value of Dc-1 and Dc-2 is used as the displacement of the crosshead, as shown in Figure 2.5 and the following Eq. 2.1.

$$D_c = \frac{1}{2} \times (D_{c-1} + D_{c-2}) \quad (2.1)$$

Where c denotes cross head and D_c means the displacement at the movable crosshead.

- Two steel rods are inserted into two ends of the specimen (shown as two red boxes in Figure 2.5), then the relative displacements of both left and right sides are summed and used as the displacement of the specimen, as expressed in the Eq. (2.2):

$$D_s = (D_{sL} + D_{sR}) \quad (2.2)$$

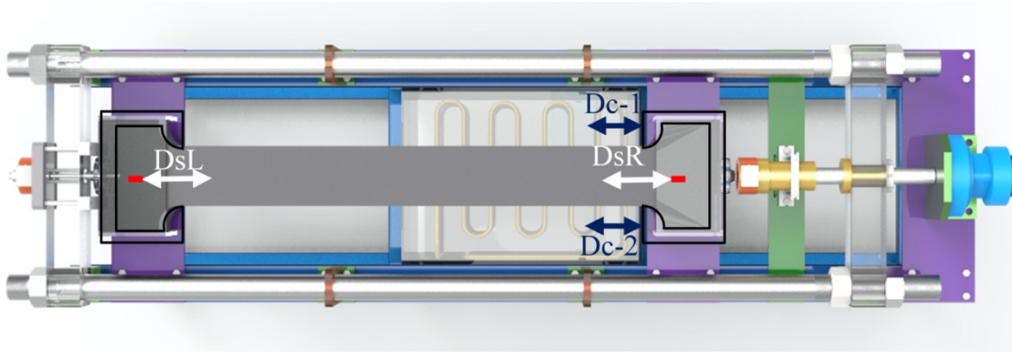


Figure 2.5 Methods for Displacement Measurement

The problem of the first method is that, the displacement of the crosshead may be affected by the deformation and rotation of the movable crosshead, especially when the internal tensile stress of the concrete is very large (e.g., several MPa), then the crosshead may deform to some extent (even though the crosshead is made of stainless steel). A schematic diagram is shown in Figure 2.6 to illustrate these problems. Under large tension, the crosshead will be distorted and rotated to some degree. One way to reduce its effect is to employ adequate restriction in the transverse direction to mitigate the rotation using springs or roller support. Please noted that this restriction should be properly designed, too small restriction will not be effective while overlarge restriction can exert too large friction and affect the tested longitudinal deformation of the specimen.

2. Early-age Deformation and Stress Development

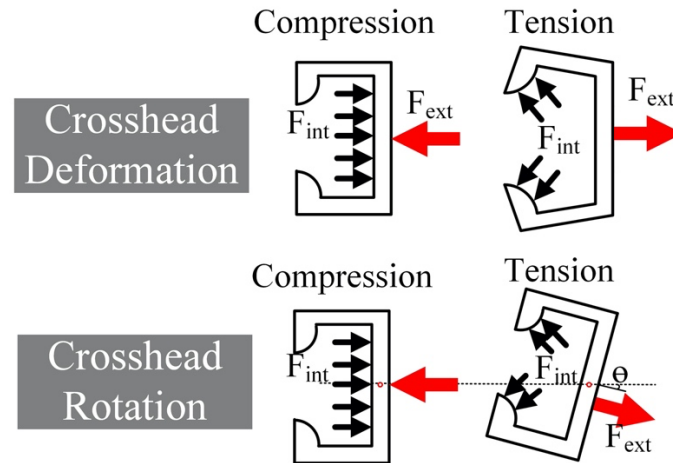


Figure 2.6 Crosshead deformation and rotation under large tension

The way of inserting steel rods or bars inside the concrete is generally used by many researchers (Springenschmid, 1998; Nguyen *et al.*, 2019b) to measure the displacement of the specimen. But it brings about another problem that, before the concrete has been hardened and gained enough strength, the embedded rods are generally not connected stably with the semi-liquid like concrete and their tiny vibrations will affect the control system. Also, the compaction of fresh concrete at the interface between steel rods and concrete is important, and attention should be paid especially when dealing with concrete mixtures with low flowability, since large voids at the interface are easily introduced in this case. These voids should be avoided, which render the displacement control invalid.

By considering the pros and cons of these two methods, in our full-restraint experiments, before the concrete has been hardened the crosshead deformation (D_c) is used for controlling, while after concrete has gained enough strength to hold the embedded steel rods (e.g., 24 hours after casting), the specimen deformation (D_s) is used. A comparative analysis of both of the methods is also conducted, and it is found the difference of using D_c for the whole testing and the aforementioned “ D_c - D_s ” method will be less than 8% of the total free deformation.

2.1.6 Summary on Updated Features

As a summary for the new features of the Ver. 1.1, several slight modifications were made on the Ver. 1.0 (Lin, 2006), these modifications and some of the details can be seen in Figure 2.7:

- The screw rod is changed into a longer one for larger detectable free strain, currently the maximum detectable free strain can be $\sim 2000 \mu\epsilon$.
- Snap-action switch (Microswitch) has been installed as a physical protection mechanism for the machine, whenever the deformation is out of applicable range, the microswitch will be activated to avoid damage of the machine (e.g., the malfunction of the control system).

2. Early-age Deformation and Stress Development

- Springs with proper stiffness have been applied in the transverse direction of the crosshead to achieve more stable displacement control and measurement (to avoid overlarge rotation of the crosshead).
- Roller support system under the crosshead has also been slightly changed, for smooth movement of the crosshead.
- The jack system for popping out the specimen after testing has been changed to new one with larger stroke for easier labor work.
- New sensors, DAQ and PC system has been rewired and connected, with function of remote real-time control added on.

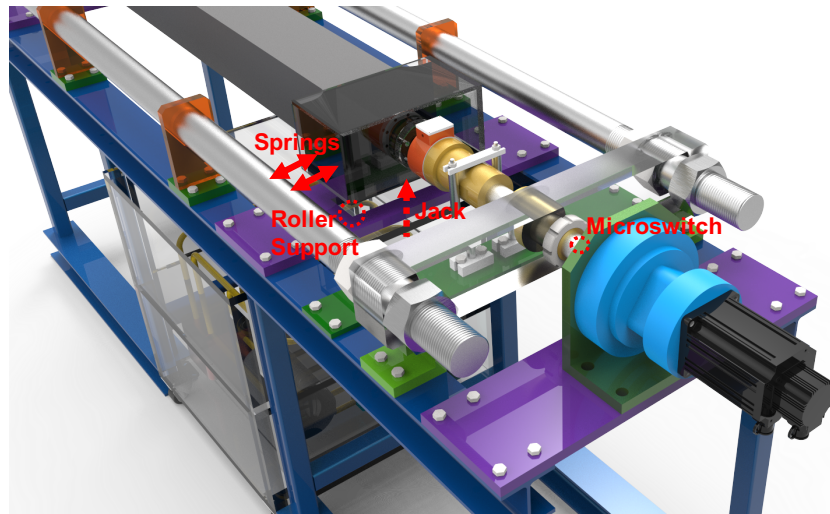


Figure 2.7 Details and Modifications of UTokyo TSTM (Ver. 1.1)

2.2 Experimental Scheme for TSTM

2.2.1 Full-Restraint Condition

As mentioned above, the current specimen size between two crossheads is 1200 mm. In the full-restraint condition, the deformation of the specimen is not allowed to exceed a pre-set threshold value ($0.5 \mu\text{m}$). In other words, once the deformation of the specimen is reaching $\pm 0.5 \mu\text{m}$, the step motor will drive the specimen back to the original position. In this case, the full-restraint condition in the longitudinal direction can be achieved. In Springenschmid's TSTM, this threshold value is set as $1.0 \mu\text{m}$ for 1500mm long specimen (Springenschmid, 1998). Since the specimen is not allowed to deform freely, internal stress will be generated and accumulated. The stress development can be tested, as shown in Figure 2.8 (a). Please noted that a cracking frame cannot achieve a full-restraint condition, the mathematical derivation is also given by Lin (Lin, 2006). Herein, the modelling of the working principle of cracking frame and TSTM can be referred to **Appendix** (Modified on Lin's derivation). The principles regarding how TSTM achieves full-

2. Early-age Deformation and Stress Development

restraint stress measurement will be revealed, it serves as a preliminary but also fundamental step for the consistent experimental results between different TSTMs from different organizations.

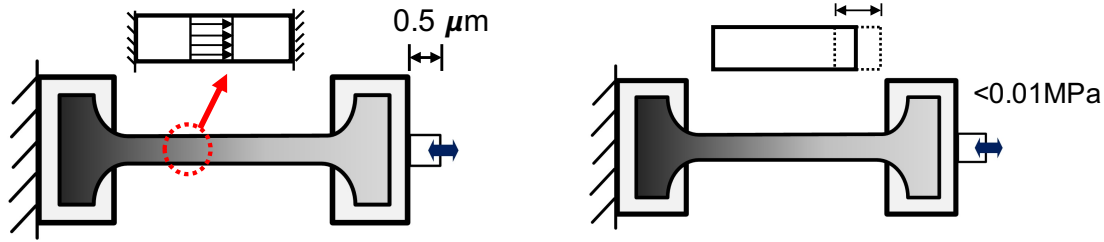


Figure 2.8 (a) Full-restraint Condition (b) Free Deformation Condition

2.2.2 Free Deformation Condition

In the free deformation condition, the specimen is allowed too freely move forward and backward. Under this condition, the tested stress will not be larger than 0.01 MPa, whenever the stress reaches to this value, step motor will be activated, and specimen can freely deform. The frictions incurred in this condition only comes from contacts between specimen and roller supports, and thus, it can be taken that a satisfactory free condition is fulfilled (Figure 2.8 (b)).

2.2.3 Measurement of Elastic Modulus

The measurement of young's modulus can be conducted in the following procedure: the specimen is pulled and compressed around 20 μm, the Young's modulus was then computed as in Eq. (2.3), as proposed by Lin (Lin and Kishi, 2006)

$$E(t) = \frac{\Delta\sigma(t)}{\Delta D(t)} l \quad (2.3)$$

Where $\Delta\sigma(t)$ is stress variation, $\Delta D(t)$ is the deformation variation and l the specimen length.

2.2.4 Evaluation of Early-age Creep

For the evaluation of early-age creep using TSTM, many researchers (Maruyama, Park and Noguchi, 2003; Tao and Weizu, 2006; Choi *et al.*, 2015; Zhao *et al.*, 2020) used the Kovler's method (Kovler, 1994; Kovler, Igarashi and Bentur, 1999). However it was pointed out by Lin (Lin, 2006) that it does not take into account the effect of stiffness of machine. The cumulative curve of restored elastic displacements at each cycle was regarded as the total elastic deformation of the specimen by Kovler, however, another “invisible” part of elastic deformation due to the confinement of machine was omitted, which was converted to the restrained stress. Because of this setback, the evaluated creep effect from varied researches on similar mix proportions reveal large discrepancies. A more comprehensive discussion on Kovler's method and mathematical derivation can be referred to the **Appendix**.

Therefore, Lin used another method to evaluate the early-age creep, as described in the following. The free deformation of concrete specimen can be tested, which is denoted as $\varepsilon_{free}(t)$ and the development of elastic modulus $E(t)$ can also be measured based on the method described

2. Early-age Deformation and Stress Development

previously. Therefore, the theoretical elastic stress can be determined by the following Eq. (2.4), which means the elastic stress that can be accumulated, supposed the whole free deformation is all converted to stress:

$$\sigma_e(t) = \sum_{t=0}^t [\varepsilon_{free}(t + \Delta t) - \varepsilon_{free}(t)] \times E(t) \quad (2.4)$$

Then, the full-restraint stress for the same mixture can also be tested by a full-restraint test, which is denoted as $\sigma_{res}(t)$ in Eq. (2.5). The difference between the theoretical elastic stress and actual restrained stress is the relaxed part, as expressed in Eq. (2.5):

$$\sigma_{rlx}(t) = \sigma_e(t) - \sigma_{res}(t) \quad (2.5)$$

Where $\sigma_{rlx}(t)$ represents the stress due to the effect of relaxation. This relaxed stress can be used to evaluate the early-age creep effect which overcomes the problem of Kovler's method related to the "omitted" part of elastic deformation. This method is also implemented in the current study.

2.2.5 High Temperature Condition (Semi-adiabatic Condition)

In the high temperature condition, the temperature of the temperature-controlled chamber will trace the temperature of the central part of specimen, with only difference of around 0.1-0.3 Celsius degree. Whenever the temperature of the chamber sensor reveals a difference with the sensor inside the concrete specimen, which exceeds a pre-set threshold value, the heater will run and increase the chamber's temperature by circulating the hot air. In this situation, the heat of the specimen cannot be lost easily owing to the very tiny temperature difference. The outside part of the chamber is also covered by a wooden formwork filled with several cm thick polystyrene. In this manner, the semi-adiabatic condition can be simulated, with around 30 °C of the temperature increase for normal OPC concrete. The full-restraint with high temperature condition can be taken as a strict criterion for cracking performance of concrete material. If a mixture reveals only small tensile stress (much lower than its tensile strength) during this condition, the early-age cracking performance of such a material is excellent.

2.2.6 Low and Medium Temperature Condition

With respect to the low temperature condition, the heater is not activated and heat of specimen can naturally release to the environment without any insulation formworks. In this condition, without the temperature compensation effect, the heat loss is much larger, and only ~10 °C of the temperature increase will be found. The medium temperature condition is defined as that heater is turned off with only insulation formworks covering the specimen. In this medium temperature condition, ~15 °C of the temperature increase can be achieved.

2.2.7 Curing Condition

The wet curing condition, sealed curing or drying condition can all be simulated. In this study, at the early-age testing period, the specimen is sealed by double layers of plastic sheet using gum

2. Early-age Deformation and Stress Development

tape. No other source of water is supplied (like covering with wet cloth or cottons). Therefore, specimen sealed by double-layer plastic sheet is regarded as the sealed curing condition.

2.3 Experimental Method for TSTM

2.3.1 *Experimental Procedures*

- S1. Before each set of experiment, the surfaces of the steel mould of TSTM will be cleaned using sandpaper. Then double layers of plastic sheet is applied and put inside the mould.
- S2. Concrete mixture will be casted inside the mould. After casting half of the volume, concrete mixture will be compacted thoroughly and steel bars ($\varnothing 10$) will be placed at the crossheads of both the fixed end and the movable end. Noted that these steel bars are embedded just for the purpose of strengthening the crosshead. Since the region of the crosshead is not where we are concerned with, such a treatment can prevent cracks taking place at the position of the crosshead.
- S3. The second half volume of the concrete will be casted and compacted sufficiently. Then one temperature sensor will be inserted inside the center part of the concrete specimen. Another temperature sensor will be installed in the temperature-controlled sensor. The installation of these two sensors is to realize function of temperature control. The third temperature sensor can be installed on the steel frame of TSTM, and the fourth sensor can be installed somewhere exposed to the room air. The third and fourth sensors are installed just to record the variation of room temperature during testing. After installing the sensors, the surface of the specimen will be smoothed using shovel.
- S4. This step is to seal the specimen using gum tape thoroughly, so that water evaporation can be avoided. It means that drying shrinkage can be avoided. Other curing conditions can also be used, but in this study, sealed condition is kept for each test to investigate early-age stress/strain evolution without effect of drying shrinkage.
- S5. After sealing the specimen, the wooden formwork with polystyrene foam inside will be covered on the specimen. Then the sensors for measuring the displacement of the specimen can be installed. At this stage the concrete is still in liquid-like state, and the connection between the embedded rods and concrete is not stable. Once concrete has been cured for ~ 24 hours and the connection becomes strong, the leveling work, calibration of direction and position of the sensors could be conducted. And the displacement control mode can be changed from using displacement of crosshead to the displacement of steel rods of specimen. Also, the side mould and bottom mould can be detached from the specimen using screw mechanism to reduce the friction to the minimum value. As shown in Figure 2.9, the two displacement measurement methods are marked, corresponding to the set-up mentioned in Figure 2.5.
- S6. After the testing is completed, the specimen can be popped out using a jack system underneath.

2. Early-age Deformation and Stress Development



S1. Preparation



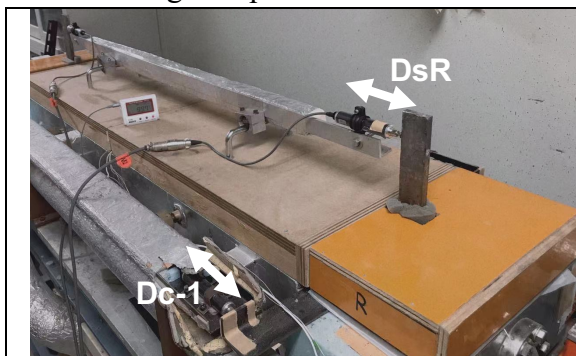
S2. Casting and Placing Steel Bars



S3. Placing Temperature sensors



S4. Sealed by gum tape



S5. Set-up of displacement sensors



S6. Pop out specimen after testing

Figure 2.9 Experimental Procedures for stress/strain measurement using TSTM

2. Early-age Deformation and Stress Development

2.4 Materials and Mix Proportions

In this study, the effect of two kinds of expansive additive materials on (CSA and MgO) compensating early-age shrinkage is investigated. The calcium sulfoaluminate additive (CSA) is a commonly used expansive additive in Japan. While MgO expansive additive is relatively new and mainly applied in dam structures (including the Three Gorges Dam Structure) in China. But the stress development of MgO concrete using TSTM is rarely reported, especially for a systematic characterization (to the author's best knowledge). As mentioned in the introduction part, TSTM is a powerful and ideal evaluation tool for examining the early-age cracking sensitivities, and thus, it will be used for understanding the stress and deformation development of this type of relatively new material.

Additionally, normal OPC concrete considering varied w/c (e.g., high strength concrete) and varied volume ratio of aggregates will also be studied. The specification of materials (including type of cement, expansive additive, sand, coarse aggregate and light aggregate) is listed in Table 2.1. A photo of all of these materials is given in Figure 2.10. The mineral composition for the OPC and CSA is listed in Table 2.2 and Table 2.3, respectively. Finally, the mix proportions is listed in Table 2.4. The water content of lightweight aggregate used in this study is around 26% by weight.

Table 2.1 Materials Type and Density

Materials	Symbol	Type	Density(g/cm ³)
Ordinary Portland cement	C	JIS	3.16
CSA	E	Denka#20	2.98
Type-I MgO (Purity:85%)	M	*HuaFengMeiYe (Reactivity: 90-120s)	--
Type-II MgO (Purity:85%)	M'	*From Mo (Reactivity: 90-120s)	--
Sand	S	Crushed stone fines	2.65
Coarse Aggregate	G	Sandstone	2.67
Lightweight aggregate	LA	Mesalite	1.67 (Surface dried) 1.33 (Fully dried)
Superplasticizer	SP	SP8N (BASF)	1.08

*Note: Type-I MgO is offered from one Chinese supplier of MgO, which is one of the suppliers to the Three Gorges Dam.

*Note: Type-II MgO is provided from Mo (Mo, Deng and Tang, 2010)

2. Early-age Deformation and Stress Development



Figure 2.10 Photo of materials used for TSTM experiments

Table 2.2 Chemical composition of OPC cement

Type	C ₃ S	C ₂ S	C ₃ A	C ₄ AF	Equivalent Alkali Na ₂ O _{eq} (%)	Blaine Fineness (cm ² /g)
	% (mass)					
JIS	59.0	17.0	7.0	10.0	0.61	3260

Table 2.3 Chemical component of CSA

Type	f-CaO	C ₄ A ₃ \$ (Hauyne)	C\$ (anhydrite)
	% (mass)		
CSA	17.0	27.0	46.0

Table 2.4 Mix Proportions for TSTM Experiment

Notation	C	Expansive Additive	W	G	LA	S	SP	W/B
	kg/m ³							
C45	400	--	180	950	--	855	3.2	0.45
C45V0.5	651	--	293	685	--	617	--	0.45
C30	496	--	149	950	--	855	5.71	0.30
E40C45	360	40 (CSA)	180	950	--	855	2.4	0.45
E40C45L	360	40 (CSA)	180	--	570	855	2.1	0.45
M40C45	360	40 (Type-I MgO)	180	950	--	855	3.33	0.45

2. Early-age Deformation and Stress Development

M'40C45	360	40 (Type-II MgO)	180	950	--	855	3.33	0.45
M20C45	360	40	180	950	--	855	3.33	0.45
E20M20C45	360	20(CSA)+20(MgO)	180	950	--	855	3.33	0.45

2.4.1 Notations

In the table for mix proportions (Table 2.4), E represents the CSA type expansive additive, M represents type-I MgO type expansive additive and M' the type-II MgO additive. The following number 40 means that 40kg of the expansive is used (or 10% of total weight of binder). C45 denotes that the water-to-binder ratio is 0.45, and C30 is the high-strength concrete with w/b=0.30. V0.5 means that the aggregate volume ratio is reduced to 50% on purpose to study the effect of aggregate, since normal C45 concrete will have a volume ratio of aggregate around 70%. L means that lightweight aggregate is used instead of normal aggregate.

2.4.2 Fresh Properties and Compressive Strength

The slumps of the mix proportions are controlled within 180mm-210mm, with suitable workability in practice. Except for the C45_V0.5, which is designed on purpose to reduce the amount of aggregate and showing a slump of more than 230mm. The air contents of all mixtures are within 1.5 to 2.5%. The compressive strength for 1 day, 3 day, 7 day and 28 day are all listed in Table 2.5. It indicates that the use of lightweight aggregate (E40C45L) will reduce the compressive strength, compared to the C45 with same w/c. C30 is the high strength concrete with a 28D compressive strength of around 68.19 MPa. The usage of either type of MgO expansive additive does not change the compressive strength, in comparison with C45. The usage of CSA does not change the compressive strength much.

Table 2.5 Compressive strength of different mix proportions (1D, 3D, 7D and 28D)

Notation	1D	3D	7D	28D
	MPa			
C45	10.87	22.57	29.37	37.70
C30	31.66	37.31	58.77	68.19
E40C45	14.35	20.79	31.38	40.54
E40C45L	9.00	15.99	23.14	29.04
M40C45	12.14	20.32	33.06	36.92
M'40C45	11.26	20.47	29.44	37.47

2.5 Experimental Results for OPC Concrete

This section provides systematic experiments on deformation and stress development of OPC concrete using TSTM. The variables of both w/c and aggregate volume ratio are studied.

2.5.1 Effect of w/c on deformation and stress development

Currently, with the development of high-rise buildings, high-strength concrete and high-performance concrete (HPC) are used more frequently in tall buildings to reduce the dimension of structural members and release more space for commercial purposes. However, the problem associated with high strength concrete is the much intensified autogenous shrinkage under low w/c, which may greatly increase the cracking sensitivities during early-age (Springenschmid, 1998). To quantify the effect of w/c on free deformation and stress development, TSTM is used in this study. Experimental results on the full-restraint stress and deformation development under sealed curing and high temperature condition are shown in Figure 2.11. The upper and bottom figures of left panel is one set of full-restraint experiment while right panel is the free deformation experiment.

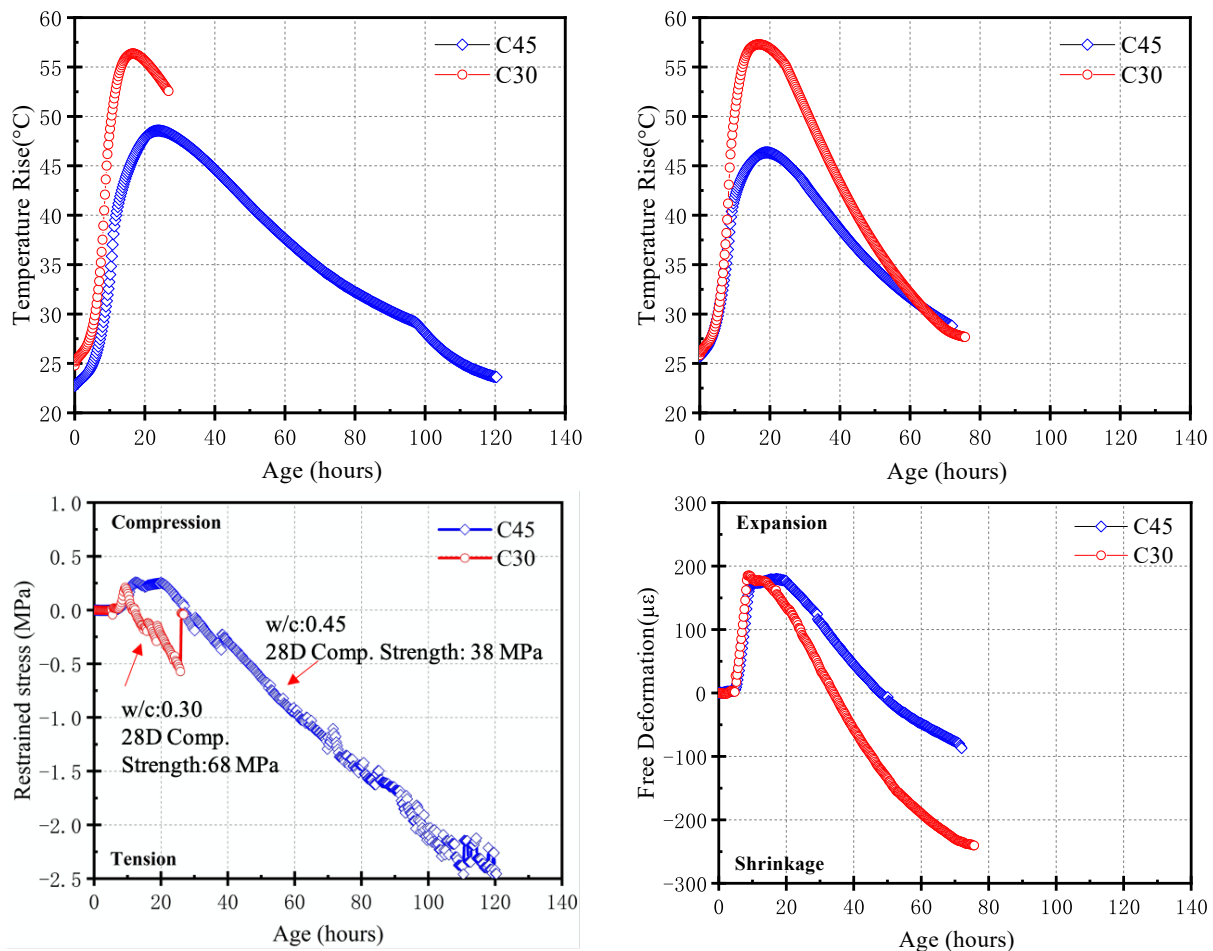


Figure 2.11 Full-restraint stress and free deformation of OPC concrete with w/c:0.45 and 0.30

2. Early-age Deformation and Stress Development

The experimental results reveal that for normal concrete with w/c:0.45, the maximum increase of temperature is $\sim 27^{\circ}\text{C}$, while for C30 with w/c:30, the increase of temperature is $\sim 33^{\circ}\text{C}$. Since hydration of larger amount of cement will generate more heat, which leads to a higher temperature increase. Under the semi-adiabatic temperature condition, the compressive stress will firstly evolve, followed by the development of tensile stress attributed to the coupled effect of thermal shrinkage and autogenous shrinkage. It is found out that even though C30 has a larger temperature increase (which means a larger thermal expansion), the development of tensile stress is very rapid. Shrinkage develops even before temperature starts to drop, because of the much larger autogenous shrinkage under a low w/c. Even though C30 is the high strength concrete with 28-day compressive strength reaching up to 68 MPa, the development of tensile strength cannot catch up with the rapid development of tensile stress, resulting in cracking at only around one day. This result indicates a much larger cracking sensitivity of high strength concrete under high temperature and full restraint condition. Noted that there are several small stress recovery periods shown in the experimental results. Those are microcracking formed at the stage of rapid development of tensile stress.

In order to further validate this phenomenon, the free deformation test is also conducted. As shown in the right panel of Figure 2.11, though C30 has a higher temperature increase, the maximum value of expansion is almost the same as C45, and the development of shrinkage is much earlier and sharper than C45. When temperature is decreasing back to the original room temperature, the final shrinkage value of C30 is around $250\ \mu\epsilon$, much larger than that of the C45, which is $\sim 100\ \mu\epsilon$. This result agrees with the conclusion drawn from the full-restraint test.

2.5.2 Effect of aggregate volume ratio on deformation and stress development

C45V0.5 means that only 50% volume ratio of the aggregate is used in the mix proportion, for normal OPC concrete, $\sim 70\%$ volume ratio of the aggregate will be used. By reducing the amount of aggregate used in the mixture, the concrete mixture should behave more like cement paste. As shown in Figure 2.12, due to less amount of aggregate and more amount of cement for C45_V0.5, the hydration heat will be higher, leading to a much larger temperature increase $\sim 38^{\circ}\text{C}$. The higher temperature increase brings about larger compressive stress. However, the development of shrinkage is very rapid, and the plateau period is short. After forming several microcracks, C45_V0.5 cracks at around 45 hours, with tensile stress only around 1.5 MPa. The mechanism can be interpreted as a combined effect from both the rapid temperature drop and the more serious autogenous shrinkage due to the lack of restraint from aggregate. It is concluded that, compared to C45, less amount of aggregate can lead to a higher cracking sensitivity.

Free deformation test can be conducted to confirm the mechanism. As found from the free deformation results (right panel of Figure 2.12), the temperature development is quite similar with that of full-restraint test. This is one of the evidence for reproducibility of the same mix proportion.

2. Early-age Deformation and Stress Development

The free deformation curve is sharper for C45V0.5. A faster development of autogenous shrinkage is found, which agrees with the aforementioned statement.

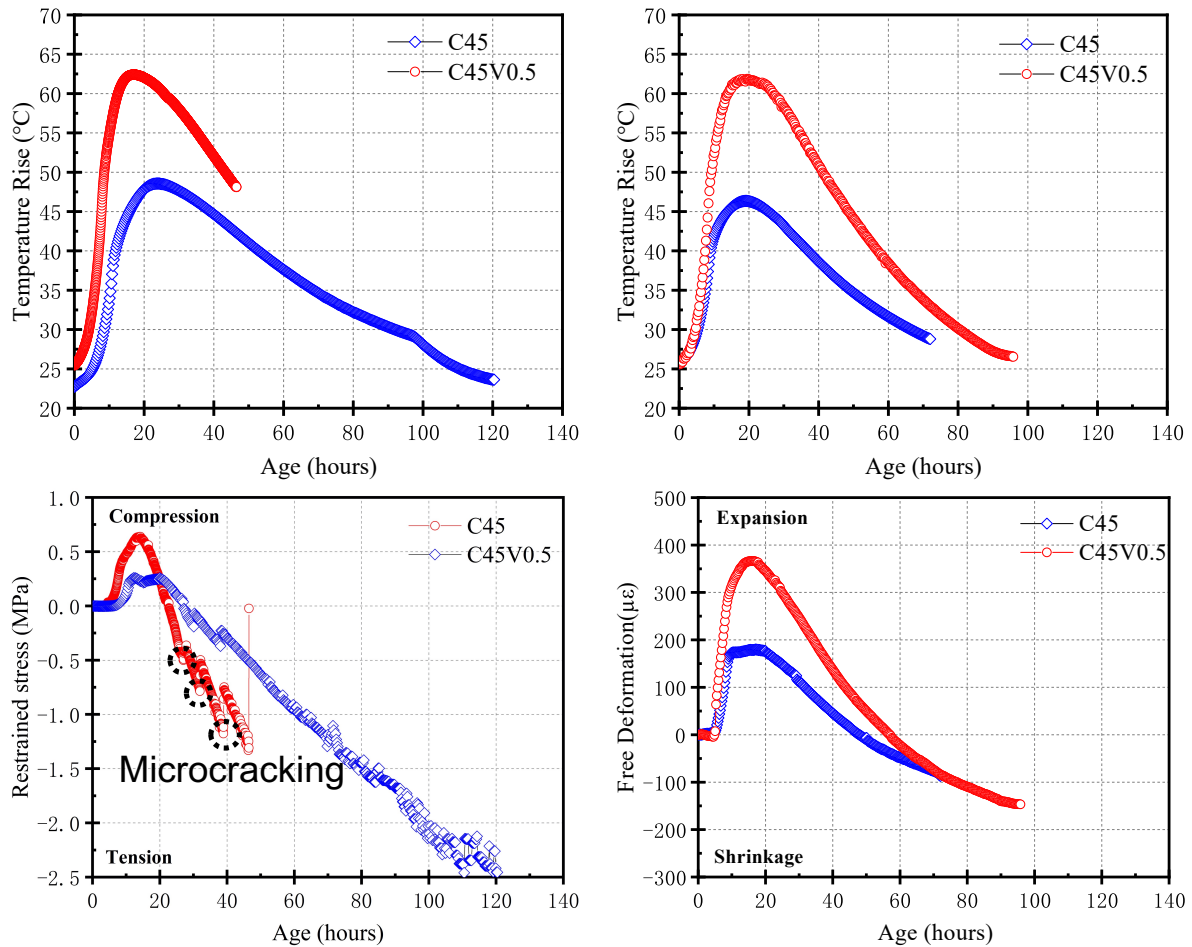


Figure 2.12 Effect of volume ratio of aggregate on deformation and stress development

2.6 Multi-scale Modeling of OPC Concrete using DuCOM

DuCOM is a multi-scale platform for life-span simulation of materials and structures using finite element method (Maekawa, Chaube and Kishi, 1999; Maekawa, Ishida and Kishi, 2009). The temperature of hydration, moisture state and pore structure development are coupled together through an interactive manner. Such a coupled thermo-hygro-mechanical process is more realistic, since the temperature field will alter the moisture state at the micro-scale (Ishida, Maekawa and Kishi, 2007), and also the intrinsic porosity of hydrates and available space for hydrate precipitation (Nakarai *et al.*, 2007). Without the treatment of coupled model, their complex interactive mechanism cannot be unfolded analytically. More detailed of this platform can be referred in the introduction section of the next chapter. In this section, DuCOM is used to study the deformation and stress development of OPC concrete only.

2. Early-age Deformation and Stress Development

2.6.1.1 FEM Mesh and Geometry

The simulated beam has the same geometry and dimension as that in the TSTM experiment. The dimension of the beam is $120 \times 120 \times 1200 \text{ mm}$, and the size of each element is $30 \times 30 \times 30 \text{ mm}$. Since the maximum aggregate size may be up to $\sim 20 \text{ mm}$, such an element size is chosen in consideration of both computation efficiency and guarantee of homogeneity.

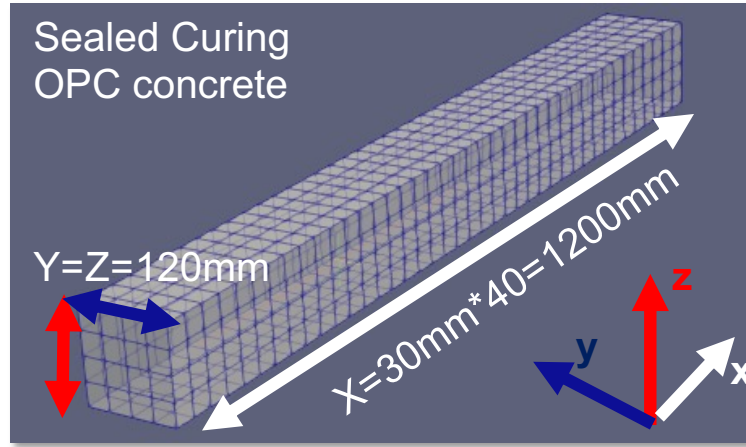


Figure 2.13 Mesh and geometry of the simulated OPC concrete beam

2.6.1.2 Boundary Condition

Two types of boundary condition are simulated: the free deformation and full restraint stress. In the free deformation case, the displacement of middle nodes at end surfaces are extracted to compute the free strain, shown as white arrow in Figure 2.14. In the full-restraint condition, all nodes at two end surfaces are fixed, and the stresses of each element at the middle surfaces are averaged, shown as the red rectangle in the figure.

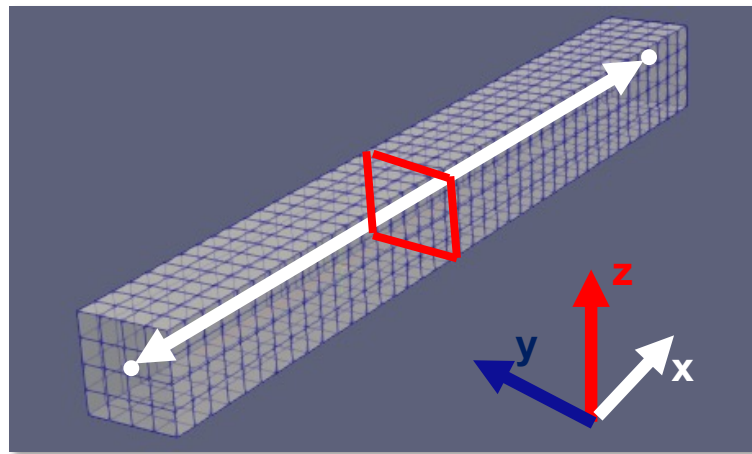


Figure 2.14 Boundary conditions: free deformation and full-restraint at end surfaces

2. Early-age Deformation and Stress Development

2.6.1.3 Curing Condition and Mix Proportion

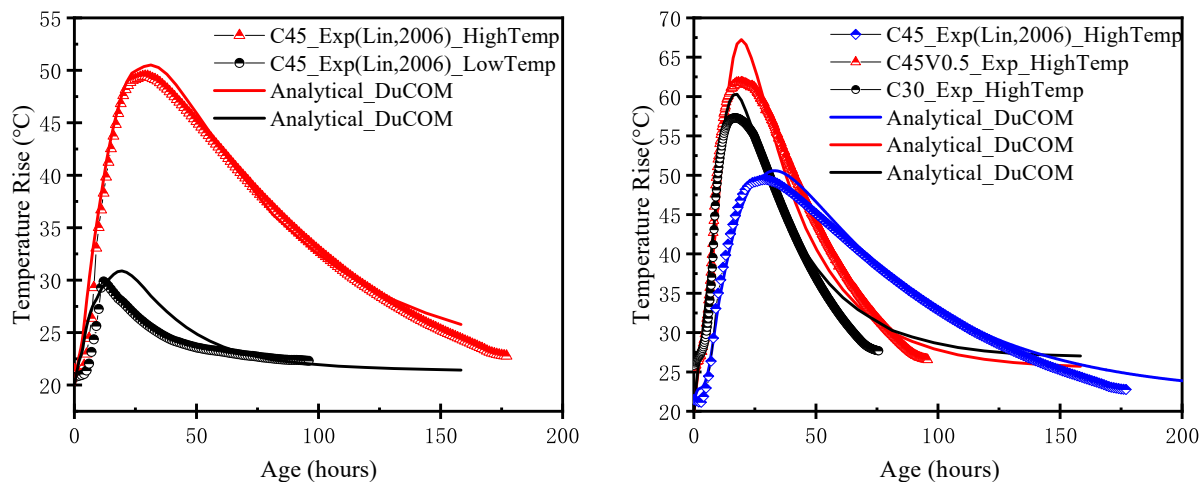
In order to achieve direct comparison between DuCOM and the experimental results from TSTM, the simulated condition is selected as sealed condition, which does not allow moisture flux into the environment. The mix proportions simulated in this study covers C45, C30 and C45V0.5, which is the same as those given in Table 2.4.

2.6.1.4 Temperature condition

Herein, the temperature histories of the chamber in the TSTM experiment are used as inputs for the model. So that the semi-adiabatic temperature condition can be simulated, with both low and high temperature conditions.

2.6.1.5 Simulation results on temperature and free deformation

Not only the experimental data in the current study is used for simulation, the data from Lin (Lin, 2006) is also collected and simulated for better comparison. The experimental data from Lin will be marked in the legend. As found in the left panel of Figure 2.15, the simulated temperature condition can agree very well with the experiment, no matter for low temperature condition or high temperature condition. Also, the predicted free deformations for C45 at both low and high temperature cases correspond well with the experimental results. The right panel of Figure 2.15 shows that the temperature history for both C30 and C45V0.5 fit well with the experiment. The free deformations for C30 and C45V0.5 also reveal good agreement with the experiments, which means that the autogenous shrinkage of low w/c concrete and the effect of aggregate could be modeled by DuCOM with adequate accuracy.



2. Early-age Deformation and Stress Development

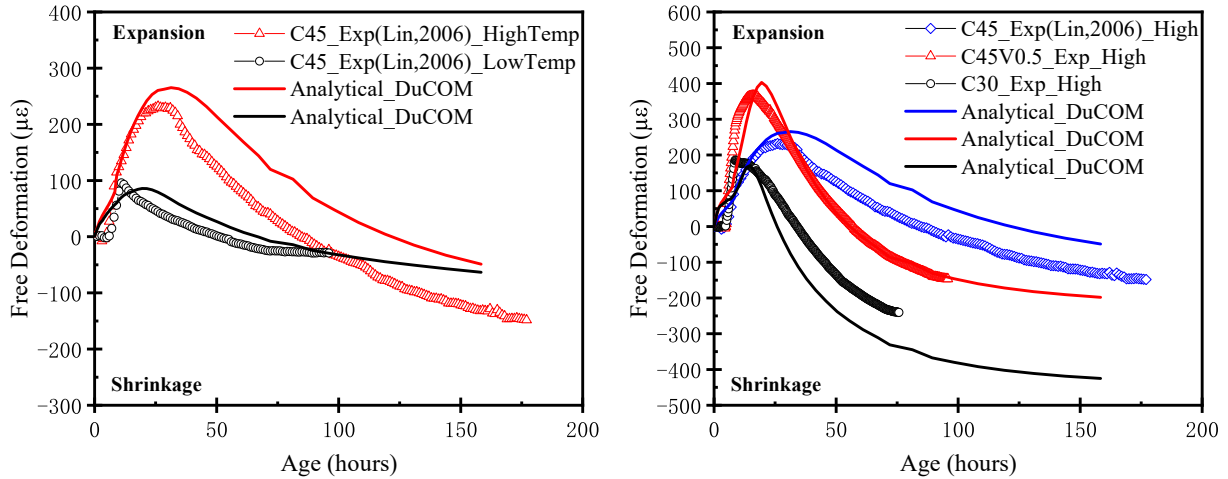


Figure 2.15 Simulation results on the temperature and free deformation using DuCOM

2.6.1.6 Simulation results on full-restraint stress development

As shown in the blue dotted line Figure 2.16, the simulation result of DuCOM is satisfactory for C45 under low temperature condition, while discrepancy is found for high temperature condition, and the stress evolution is sharper than the experimental data. The stress distribution after the cracking can also be found, with around 2.7MPa tensile stress at the middle surface. Please noted that, at this time, the region around two ends has been cracked earlier than the middle surface due to higher confinement, and after cracking, the tensile stress has been reduced lower and be more concentrated at the middle part. As shown in Figure 2.17, the simulated full-restraint stress developments of C30 and C45V0.5 under high temperature condition are both much sharper than experimental results.

The reason can be attributed to two reasons: (1) The underestimation of the early-age creep effect (2) The reduced modulus under tension is not modeled accurately. These two issues will be addressed in the following section about proposed constitutive relationship. Compared to the data regarding full-restraint stress development under high temperature condition, data about free deformation are much widely reported due to less dependence on experimental set-up. For free deformation, TSTM is not always required as some normal standard methods are capable to conduct the measurement (ASTM, 2017, 2019). As stated previously, the current DuCOM can simulate the free deformation quite well, which can be validated using many published experimental results of free deformation. Also, the creep effect on hardened samples (mostly 28 days) is adequately considered in DuCOM to model the long term mechanical behavior under loading/drying conditions (Mabrouk, Ishida and Maekawa, 2004; Asamoto, 2006; Asamoto, Ishida and Maekawa, 2006). However, the data on creep effect at very early age (with only around several days of curing age) is quite limited, and these results from TSTM can be further implemented into DuCOM in the future. The current early-age creep effect defined in DuCOM consists of the irreversible creep related to the motion of water in gel pores and delayed elasticity

2. Early-age Deformation and Stress Development

linked with the viscous flow of water in capillary pores (Asamoto, 2006). The visco-elastic behavior defined by the Kelvin-chain can be further modified/enhanced to model early-age creep effect more accurately and achieve better match with the experimental data.

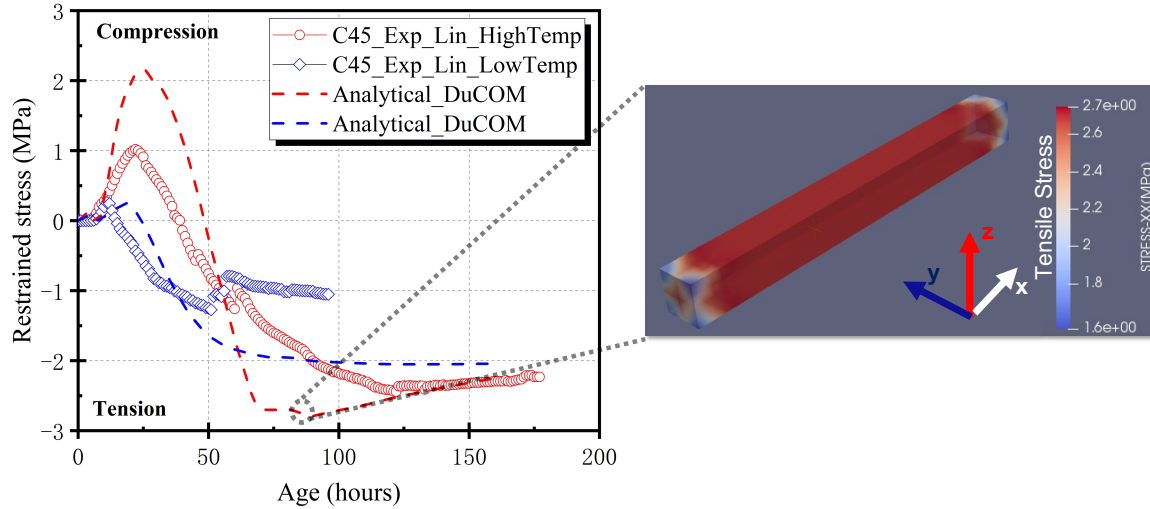


Figure 2.16 Simulation of full-restraint stress of C45 under low and high temperature

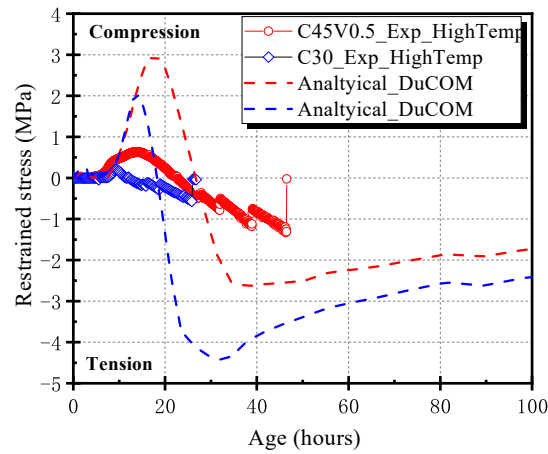


Figure 2.17 Simulation of full-restraint stress of C30 and C45V0.5 under high temperature

2.7 A Proposed Parallel-Serial Constitutive Law

This section attempts to establish a constitutive model for the early-age stress evolution of concrete, which forms on the basis of simulating the actual development of restrained stress in the TSTM test. The proposed analytical model underscores the interactive behavior between aggregate and cement matrix during varied temperature rise conditions, relating the deformation properties under free condition with stress evolution under full restraint condition. It can be served

2. Early-age Deformation and Stress Development

as an alternative to the widely-used finite element method (FEM), which offers practical value and could be applied in practice to estimate stress development.

2.7.1 The mathematical formulation

The interactive behavior between aggregate and cement matrix has been modeled by many researchers, in which the spring element with varied rheological models are considered to simulate the early age solidification process of concrete materials (R. Springenschmid, 1994; Maekawa, Ishida and Kishi, 2009). In HYMOSTRUC, cement paste is modeled as linear elastic materials with time-dependent properties and aggregate is modeled as a linear elastic material. In DuCOM, the solidification concept (Bazant and Baweja, 1997) is implemented, which treats the evolution of cement paste as a series of solidifying clusters with elastic, visco-elastic and plastic properties, aggregate is considered as linear elastic materials. In the present model, the parallel-serial relationship between aggregate and cement paste is utilized to simplify the problem in one dimension. The parallel-serial relationship (or Voigt and Reuss model) is generally applied to estimate the modulus of hardened concrete. While this concept is extended to derive constitutive law in this section (Z.H. Lin, personal communication, 2019).

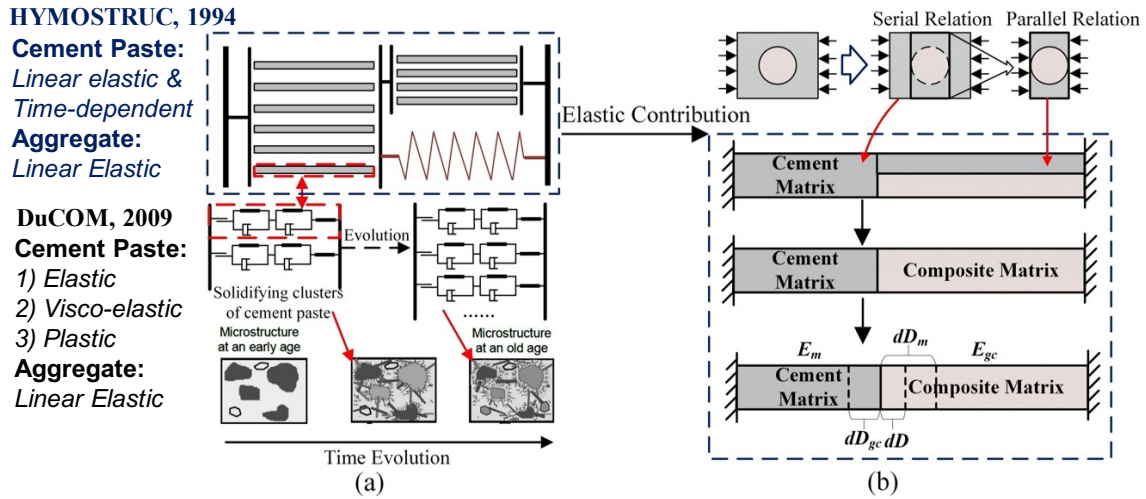


Figure 2.18 Constitutive law between aggregate and cement paste during stress development

As shown in Figure 2.18, when the concrete is subjected to external load, a portion of the cement matrix can be considered to reveal a parallel relation with aggregate while another proportion shows a serial relation. Then, the modulus of composite matrix part can be considered as Eq. (2.6):

$$E_{gc}(t) = (E_{m,p}(t)c_{m,p} + E_{ag}c_{ag}) / (c_{m,p} + c_{ag}) \quad (2.6)$$

Where E_{ag} , $E_{m,p}$, E_{gc} denotes the elastic modulus of aggregate, parallel cement matrix, and the composite matrix respectively. C_{ag} and $C_{m,p}$ represents proportions of their volume ratio. The elastic modulus of the whole system can then be calculated as the serial relation between the composite matrix and the serial matrix, determined as Eq. (2.7):

2. Early-age Deformation and Stress Development

$$E(t) = \frac{E_{gc}(t)E_m(t)}{E_{gc}(t)c_{m,s} + E_m(t)c_{gc}} \quad (2.7)$$

Where E , E_m are elastic modulus of the composite matrix and cement matrix respectively. $C_{m,s}$ represents the proportion of the serial matrix, and it always yields $c_{m,p} + c_{m,s} + c_{ag} = 1$. In this way, it could be considered as a time-dependent interaction between cement matrix and the composite matrix, as shown in Figure 2.18. Under certain temperature rise condition, if the free deformation at each time interval of composite matrix and serial cement matrix is denoted as dD_{gc} and dD_m respectively, and the balanced deformation is dD , the constitutive law in the full restraint condition can be given as

$$\frac{e(t) \cdot dD_m - dD}{l_m} E_m(t)A = \frac{dD_{gc} + dD}{l_{gc}} E_{gc}(t)A \quad (2.8)$$

In which, the dD_{gc} is the free deformation of the composite matrix, which mainly consists of aggregate, and a small portion of cement paste which behaves parallel to the aggregate. Therefore, this dD_{gc} can be easily derived by the parallel relationship. The function $e(t) = \frac{D_{elastic}}{D_{total}} = \frac{\varepsilon_{elastic}}{\varepsilon_{total}}$, $0 \leq e(t) \leq 1$ is a time-dependent function to express the elastic contribution of the total deformation (early-age creep effect). l_m and l_{gc} are the length of the serial cement matrix and composite matrix respectively. $E_m(t)$ and $E_{gc}(t)$ are time-dependent function of elastic modulus. Rearranging Eq. (2.8), it yields:

$$dD = \frac{e(t) \cdot dD_m \cdot S_m(t) - dD_{gc} \cdot S_{gc}(t)}{S_m(t) + S_{gc}(t)} \quad (2.9)$$

Where $S_m(t) = E_m(t) \cdot A/l_m$, $S_{gc}(t) = E_{gc}(t) \cdot A/l_{gc}$ and A is the area of cross section. Substituting Eq.(2.9) into $d\sigma = \frac{e(t) \cdot dD_m - dD}{l_m} E_m(t)$, the stress increment at time t yields,

$$d\sigma = \frac{e(t) \cdot dD_m + dD_{gc}}{A \left[\frac{1}{S_m(t)} + \frac{1}{S_{gc}(t)} \right]} \quad (2.10)$$

Therefore, the restrained stress at time t can be expressed as:

$$\sigma(t) = \int_0^t [e(t) \cdot D'_m(t) + D'_{gc}(t)] \cdot \frac{1}{A \left(\frac{1}{S_m(t)} + \frac{1}{S_{gc}(t)} \right)} dt \quad (2.11)$$

The equations above are formulated by consideration of $e(t)$, i.e., the elastic proportion of the total free deformation, similar to the concept of creep coefficient. If formulated in the manner of stress relaxation, the theoretical elastic stress can be given as:

$$\sigma_e(t) = \int_0^t [D'_m(t) + D'_{gc}(t)] \cdot \frac{1}{A \left(\frac{1}{S_m(t)} + \frac{1}{S_{gc}(t)} \right)} dt \quad (2.12)$$

The restrained stress can be computed by subtracting the relaxed stress $\sigma_{rlx}(t)$ from theoretical elastic stress, as determined in Eq. (2.13):

$$\sigma(t) = \sigma_e(t) - \sigma_{rlx}(t) \quad (2.13)$$

2. Early-age Deformation and Stress Development

2.7.2 Formulation of relaxed stress

In order to evaluate the early-age creep effect, the formulation of relaxed stress should be given. For the simplest form, the relaxed stress could be directly proportional to the theoretical elastic stress, as shown in Eq. (2.14):

$$\sigma_{rlx}(t) = f(\sigma_e(t)) = \sigma_e(t) \cdot f_r \quad (2.14)$$

Where f_r is a constant which denotes the proportion of relaxed stress.

However, the experimental reveals that the relaxed stress may not be simply proportional to the theoretical elastic stress. Figure 2.19 shows the restrained stress of C45 in high temperature case, as expressed by black line. The red line represents the calculated theoretical elastic stress from experimental results using Eq. (2.14). Noted that when calculating this theoretical elastic stress in Figure 2.19, both elastic modulus and free deformation are obtained directly from TSTM experiment. It implies that if the relaxed stress is expressed by Eq. (2.14), there will be a difference on the “zero-stress” time between the analytical result (the red line) and experimental result (the black line), since the red line does not intersect with the black line at the time point of “zero-stress”. It indicates there might be another time-related effect of the relaxed stress. Therefore, in order to model the early-age creep effect more accurately, the time-related term is included. It is considered that the creep effect is associated with both of the time and stress (R. Springenschmid, 1994).

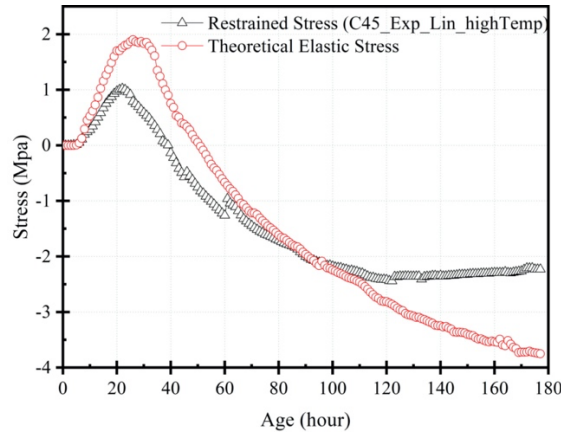


Figure 2.19 Theoretical elastic stress and restrained stress

Eq. (2.14) is then reformulated into Eq. (2.15), by adding one time-related term:

$$\sigma_{rlx}(t) = f(\sigma_e(t), t) = \sigma_e(t) \cdot f_r + R_{max}[1 - \exp(-k_r \cdot t^4)] \quad (2.15)$$

Where R_{max} denotes the maximum value of relaxed stress (MPa), and k_r is a rate constant and t is the time (days).

2.7.3 Consideration of Reduced Tensile Modulus

The early-age modulus development of concrete materials is hard to be tested, especially under varied temperature histories. With TSTM, the modulus development of concrete materials under

2. Early-age Deformation and Stress Development

varied temperature history and restraint degrees could be tested, which offers much engineering value to understand the early-age mechanical properties. The experimental data regarding modulus development from Lin (Lin, 2006) is categorized in Figure 2.20. The low temperature cases are colored in blue while high temperature in red. It can be found out from the left panel that, under a high temperature condition, the modulus tested under free condition is slightly lower than that in low temperature condition, which might be owing to the coarser pore structure under higher temperature. This effect will be further discussed in the following chapter regarding pore structure.

It is noteworthy that under a full-restraint condition, the modulus is much lower for high temperature cases, in comparison with low temperature case. It can be attributed to the much steeper temperature gradient and correspondingly, larger tension will be applied, which causes the reduced modulus. A proposed mechanism is given as Figure 2.21. It can be envisaged that, under compression (e.g., when temperature is increasing), the effect of interfacial transition zone (ITZ) on modulus development is negligible. While when subjected to tension (when concrete starts to shrink), there will be much micro-cracks formed and propagating through the ITZ. This ITZ is the weakest link in the concrete material, because at the boundary between cement paste and aggregate, the content of cement particles will be deficient. This effect is also known as the “wall effect” (Diamond and Huang, 2001). The reduced modulus under high temperature condition can also be found CSA concrete, shown in the middle panel of Figure 2.20. However, interestingly, when lightweight aggregate is used, this effect is not pronounced. It may be related to the round shape and low stiffness of the lightweight aggregate, which reduces the stress concentration at the ITZ and number of micro-cracks. And thus, there is no much difference of modulus between high temperature case and low temperature case.

In order to model the tensile modulus of concrete with normal aggregate, the following empirical relationship can be used:

$$E_{m,t} = \eta_t E_{m,free} \quad (\eta_t \leq 1.0) \quad (2.16)$$

In which η_t denotes an empirical parameter to consider the reduction of modulus under tension. After optimization, under high temperature, η_t will be 0.55, 0.60, 1.0 for OPC concrete, CSA concrete and concrete with lightweight aggregate, respectively. $E_{m,free}$ represents the modulus under free deformation, which can be upscaled from a coupled model in a smaller scale. It will be discussed in the later chapter regarding pore structure.

2. Early-age Deformation and Stress Development

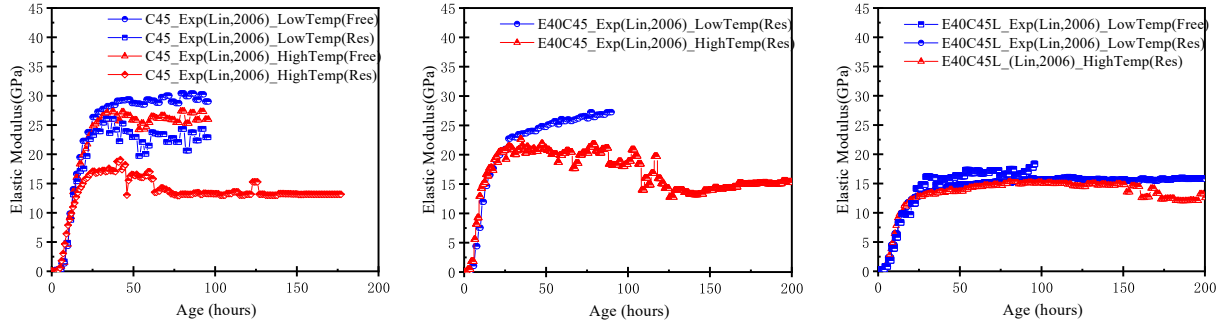


Figure 2.20 Elastic Modulus of OPC, CSA and CSA concrete with LA under varied conditions (Lin, 2006)

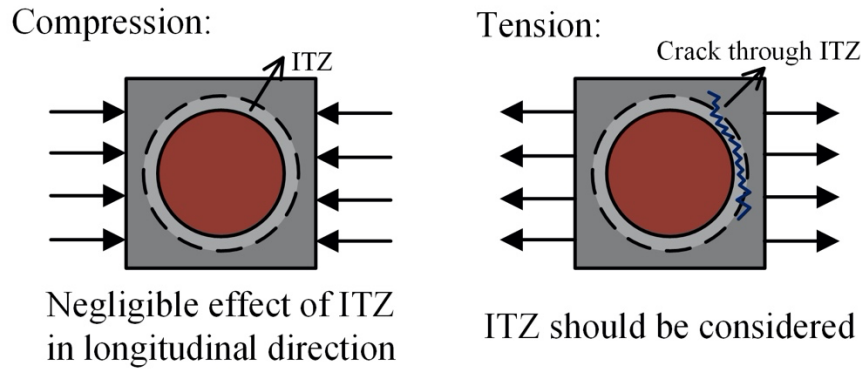


Figure 2.21 Reduced Tensile Modulus and Microcracks

2.7.4 Computation Flow of the Constitutive Law

After determining the development of free deformation, relaxed stress and elastic modulus, the stress evolution could be computed using the constitutive law (Eq. (2.12) & Eq. (2.13)). The computation flow of the whole process is also shown in Figure 2.22. In which, the stiffness-related properties, deformation-related properties could be determined using the parallel-serial relation. And then, these inputs could be used to compute the theoretical elastic stress, relaxed stress and restrained stress. This computed restrained stress can be used to compare with the TSTM results. Additionally, another advantage of proposing such a simplified model is that, only if the elastic modulus and free deformation, and temperature condition is determined in practice, the restrained stress could be estimated by the simplified model. Compared to the restrained stress which requires a well-designed TSTM set-up, the determination of free deformation, temperature history and elastic modulus are relatively easy. Only if these information are provided on site, the restrained stress could be estimated by the proposed constitutive law.

2. Early-age Deformation and Stress Development

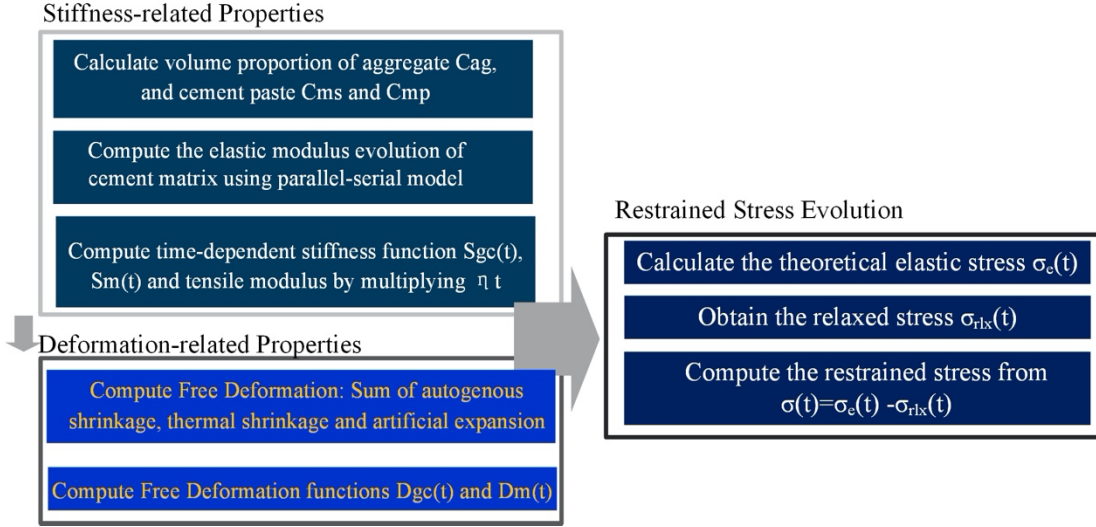


Figure 2.22 Computation Flow of the Constitutive Law

2.7.5 Model Validation for OPC concrete

2.7.5.1 Hydration heat and temperature

Kishi (Maekawa, Chaube and Kishi, 1999) proposed a multi-component model for the heat of hydration, which is able to simulate the adiabatic temperature rise of concrete with varied components, including early hardening Portland cement (EPC), ordinary Portland cement (OPC) and moderate-heat Portland cement (MC), binary blended cement with blast furnace slag or fly ash. In this study, this hydration heat model is used as one of sub-model. The temperature predictions of EPC, OPC and MC are successfully reproduced, as shown in **Appendix**. After predicting the adiabatic temperature, the semi-adiabatic temperature condition could be derived by consideration of heat loss due to the conduction and radiation.

$$\dot{Q}_{semi} = \dot{Q}_{ad} + \dot{Q}_{cond} + \dot{Q}_{rad} + \dot{Q}_r \quad (2.17)$$

Where \dot{Q}_{semi} denotes the heat rate of a semi-adiabatic temperature condition, and \dot{Q}_{ad} is the adiabatic temperature rise, \dot{Q}_{cond} and \dot{Q}_{rad} denote heat loss due to conductivity and radiation, respectively. \dot{Q}_r is a modified term which considers the non-ideal heat loss due to the gap and compensation effect of the temperature-controlled chamber, which can be optimized by matching with the TSTM experimental results.

According to Fourier's law of conduction,

$$\dot{Q}_{cond} = -kA \frac{dT}{dx} \quad (2.18)$$

Where k is the thermal conductivity ($J \cdot m/sec \cdot K$), A is the exposed surface area (m^2), x is the thickness of the layer (m). For the material of polystyrene, $0.033 J \cdot m/sec \cdot K$ will be adopted. dT represents the temperature gradient in kelvin.

2. Early-age Deformation and Stress Development

The rate of heat transfer can be determined by Stefan-Boltzmann law of radiation

$$\dot{Q}_{rad} = \sigma e A T^4 \quad (2.19)$$

In which, σ is the Stefan-Boltzmann constant equaling to $5.76 \times 10^{-8} \text{ W/m}^2 \cdot \text{K}^4$ and e the emissivity of materials, and 0.93 is used in the current model. A is the area of the surface (m^2). T represents the absolute temperature (K). As found from Figure 2.23, the simulated temperature can match well with the experimental data, which can be used as input for the derivation of thermal deformation with adequate accuracy.

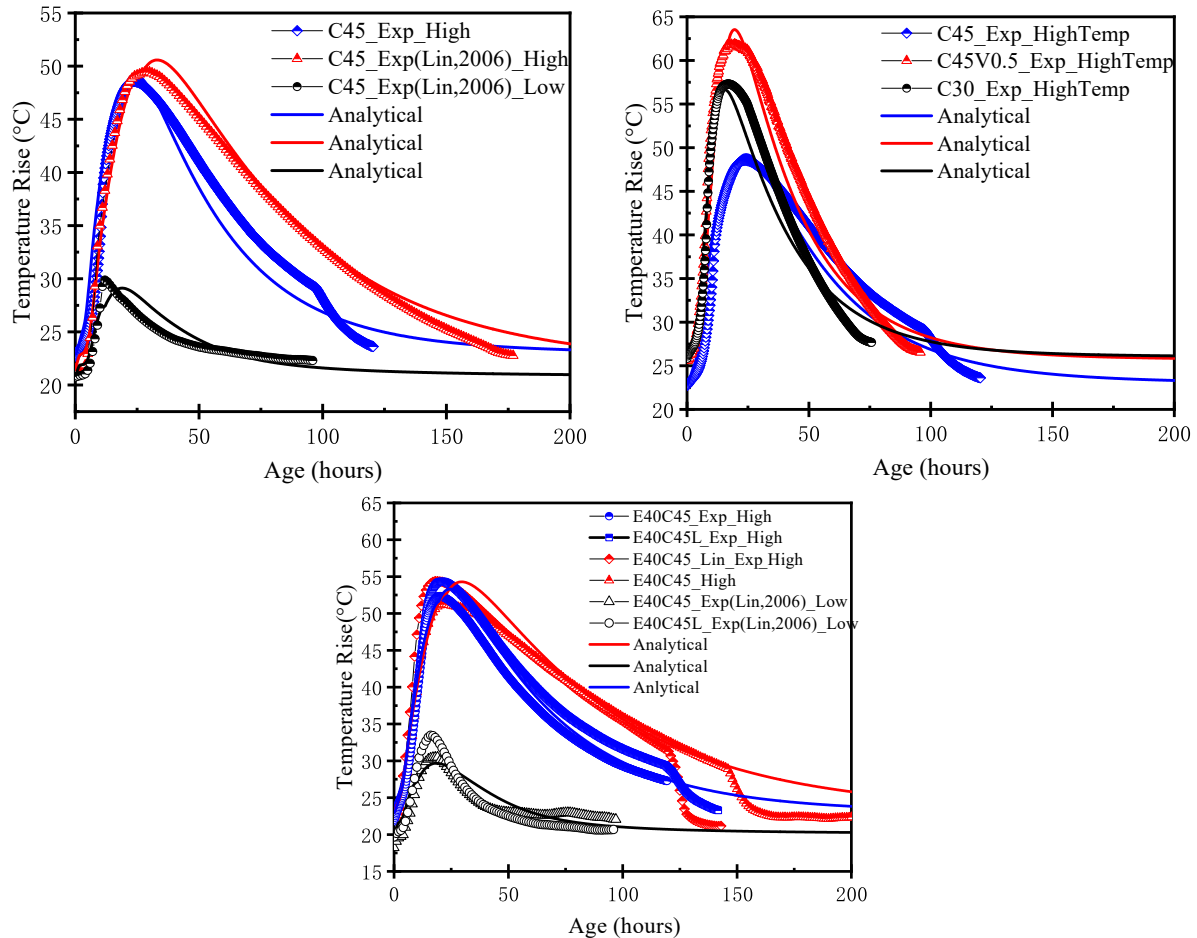


Figure 2.23 Simulation of semi-adiabatic temperature conditions for OPC and CSA concrete

2.7.5.2 Modeling results of free deformation for OPC concrete

The free deformation consists of two parts for OPC concrete, the thermal deformation and the autogenous shrinkage. The detailed computation method will be illustrated in the following chapter regarding the coupled model in a smaller scale. Herein, the free deformation of the aggregate and cement matrix could be illustrated in Figure 2.24. As formulated in the previous section, the composite matrix consists of aggregate and a small portion of aggregate, and its property is mainly governed by aggregate's property. Therefore, the free deformation of the

2. Early-age Deformation and Stress Development

composite matrix will witness an expansion and shrinkage process, due to the increase and drop of the temperature in a semi-adiabatic temperature condition. Since the thermal expansion coefficient (TEC) of aggregate is a time-invariant constant, when temperature drops back to the original value, the deformation of the composite matrix (solid red line) will return to roughly zero (small portion of cement paste will induce small shrinkage for the composite matrix). When less volume of aggregate, for example, only 50% is used, the higher amount of cement will lead to a higher temperature increase. Then, the expansion of composite matrix will be higher (dashed red line), but meanwhile, the cement matrix will reveal more shrinkage due to a larger volume ratio and less restraint from aggregate.

In another scenario, when a lower w/c is adopted (with the same aggregate volume ratio), the autogenous shrinkage of the cement matrix will be much larger, while the composite part remains almost unchanged. The summation of dashed line will lead to a similar pattern of deformation development as Figure 2.25, which shows the prediction of free deformation and has good agreement with experimental results for OPC concrete.

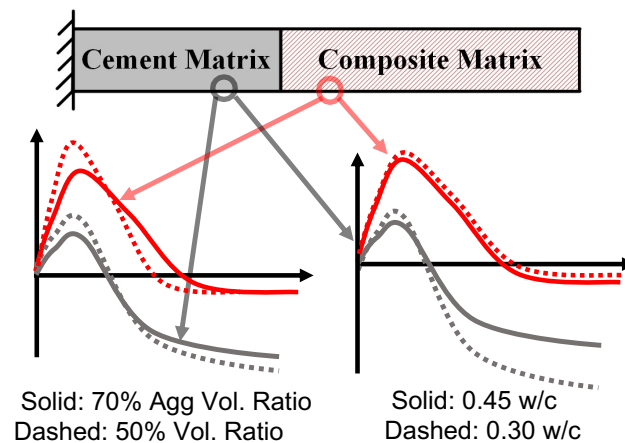
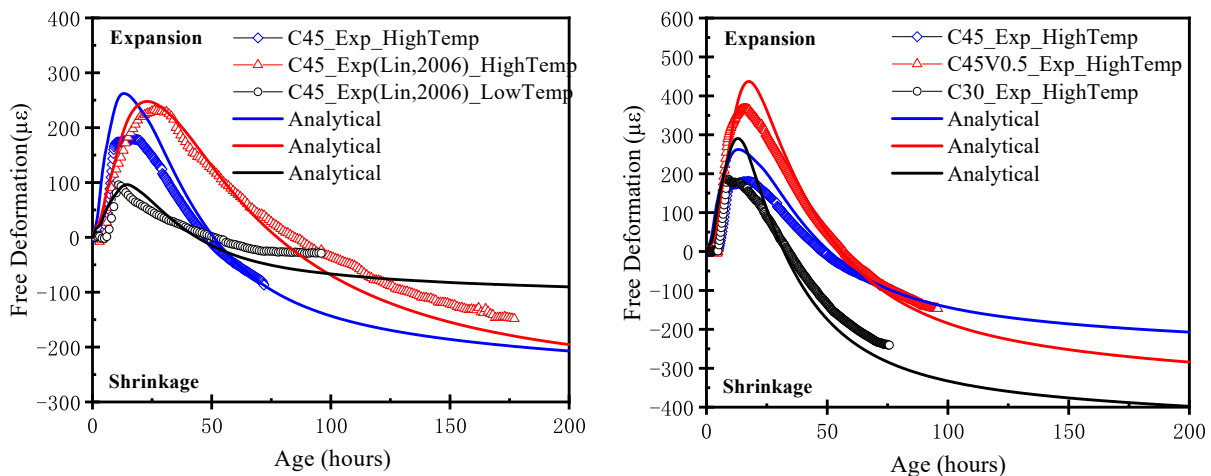


Figure 2.24 Schematic diagram of free deformation

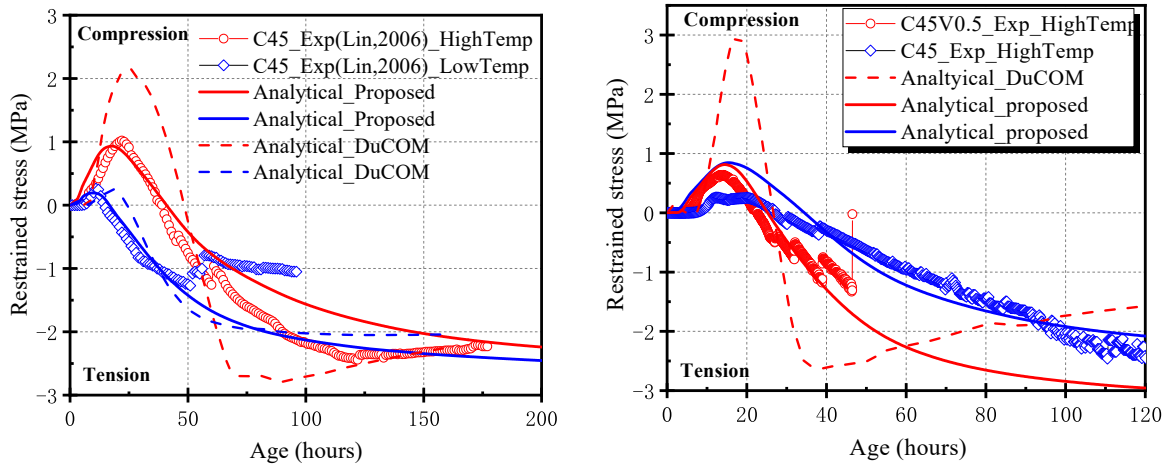


2. Early-age Deformation and Stress Development

Figure 2.25 The modeled free deformation of OPC concrete and experimental validation

2.7.5.3 Modeling results of restrained stress for OPC concrete

Following the computation flow, the determined free deformation, modulus development can be substituted into the constitutive law and acquire the theoretical elastic stress. Then by optimization, the relaxed stress could be determined: $F_r=0.4$, which signifies around 40% of the stress is relaxed due to the applied stress, $R_{max}=0.5$, which means that there is around 0.5MPa of the time-dependent relaxed stress. The rate constant is found out to be $K_r=0.1$ for high temperature condition and $K_r=10$ for low temperature condition. The modeling results of restrained stress are given in Figure 2.26. The dashed line represents the modeled results from DuCOM, and the solid lines are the modeled results from the simplified constitutive relationship. As found from the figure, the proposed constitutive relationship is able to trace the realistic stress development with adequate accuracy. The published experimental data on early-age creep effect is quite limited due to the difficulty of conducting experiment on early-age concrete which is still in a soft state, but it was pointed out creep effect at early age could be systematically higher than that at later age (Pane and Hansen, 2002; Jiang, De Schutter and Yuan, 2014). By conducting both full-restraint test and free deformation test using TSTM, the stress relaxation could be quantified. The relaxed stress is currently treated by some optimized empirical values. The author believes that with more experimental data provided, the current empirical treatment can be replaced by a more sophisticated formulation for underlying mechanism. Also, with these experimental data from TSTM, the current formulation on the elastic-viscosity given in DuCOM can also be modified to attain better agreement with the experiment.



2. Early-age Deformation and Stress Development

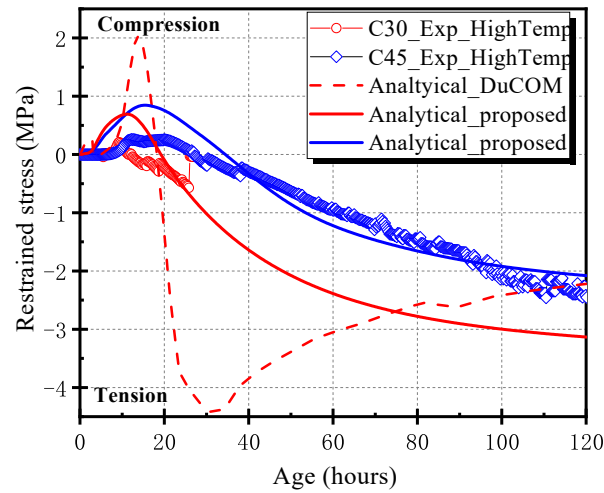


Figure 2.26 Model validation of the restrained stress by proposed constitutive law

2.7.5.4 Applicability and Extensibility

The analytical model is established on the basis of mutual interaction between cement matrix and aggregates via simplified analysis on stress and deformation balance between two mediums in one dimension. It is capable of tracing the stress evolution under varied temperature rise conditions. Certainly, the commonly-used FEM method can simulate much sophisticated scenarios with different boundary conditions and geometries. However, the validation through reliable experimental results also plays a key role in cracking sensitivity analysis. Though limited to simple boundary condition, if the analytical model is able to trace the thermal stress evolution under full-restrained and semi-adiabatic condition (which can be considered as a relatively strict criterion for evaluating thermal cracking), it will point towards a more practical and intuitive method for testing cracking sensitivities of varied mix design.

The solidification model (Bazant and Baweja, 1997; Mabrouk, Ishida and Maekawa, 2004) generally simulates increasing numbers of solidifying clusters forming gradually as hydration proceeds. The stress of each cluster is a function of strain at the present time t and time t' at which the cluster is formed, and the thermodynamic state. The historical properties of different clusters are mutually independent. In this way, the formation of clusters can be related to the hydration process more logically. The proposed model can be considered as treating the solidification process as single integrated solidifying cluster with time variables, which may be less meticulous in physics, but practically offers acceptable characterization for the deformation, stiffness and stress state.

2.8 Experimental Results for CSA Concrete

2.8.1 Deformation and Stress Development of CSA Concrete with/without LA

In this section, expansive concretes with 10% of CSA with/without lightweight aggregates are experimentally studied. Notation C45 is the normal OPC concrete, while E40C45 means that 10% of CSA expansive additive is added. E40C45L represents a combined usage of 10% of CSA additive and lightweight aggregate as coarse aggregate. From the results of temperature rise we can find out that the expansive additive will lead to slightly higher temperature increase compared to normal OPC concrete C45, as shown in Figure 2.27. An important feature of E40C45 is that, even though a much larger compressive stress of around 1.5 MPa is generated before the first day of curing, the development of tensile stress is quite rapid. At around 5 days, the tensile stress of E40C45 reaches to 1.5 MPa. It could be concluded that, under a high temperature rise case, CSA concrete could not offer enough effective expansion in a longer term to compensate the rapid development of autogenous shrinkage and thermal shrinkage. This is also the reason that, in actual engineering application, CSA concrete is found to be only effective in compensating shrinkage under low temperature condition whereas, it lacks applicability under high temperature condition.

However, very interestingly, with a combined use of CSA expansive additive and lightweight aggregate (E40C45L), the shrinkage can be effectively compensated, leading to an excellent cracking performance. As shown in Figure 2.27, at the first day, E40C45L has a higher compressive stress of around 2.0MPa. When temperature returns back to original temperature, there is still 0.3 MPa of compressive stress left. This combination of CSA expansive additive and lightweight aggregate reveals very low cracking sensitivity even under the strict criterion of a high temperature condition with full-restraint degree. The mechanism could be attributed to (1) low stiffness of lightweight aggregate (2) the internal curing effect of lightweight aggregate, which serves as water reservoir for further hydration of CSA. These experimental findings regarding CSA concretes (with/without LA) were firstly discovered by Lin (Lin, 2006), but the mechanism of ineffective expansion of CSA concrete was not fully explored and the stress/deformation development of CSA concrete were not modeled, which will be addressed in the current study.

In order to further confirm its shrinkage compensation effect, the tests on free deformation are also conducted, as shown in the right panel of Figure 2.27. The higher expansion caused by E40C45L can be attributed to the internal curing effect from lightweight aggregate, which provides more sufficient water for expansion. It can be found out that, when temperature starts to drop, the maximum shrinkage value of C45 and E40C45 is $\sim 280 \mu\epsilon$ and $\sim 290 \mu\epsilon$, respectively. The shrinkage values of C45 and E40C45 are very close to each other, which also illustrates that the single use of CSA expansive additive could not effectively compensate the shrinkage when temperature starts to decline. With respect to the E40C45L, the maximum shrinkage value is only $\sim 160 \mu\epsilon$, which supports the finding from restrained stress development that a combined usage of

2. Early-age Deformation and Stress Development

expansive additive with lightweight aggregate provide much efficient expansion effect in a longer term to compensate the early-age shrinkage.

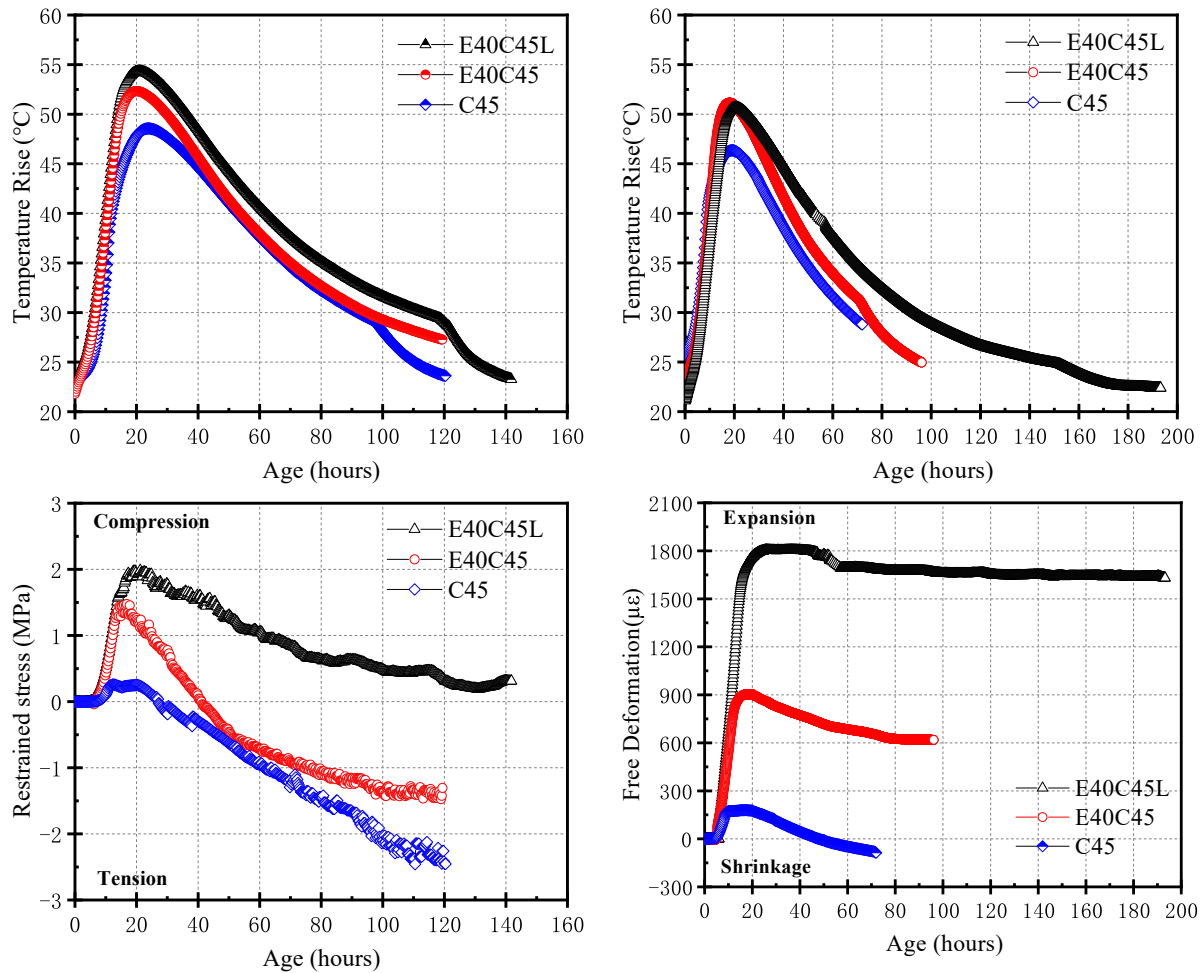


Figure 2.27 Deformation and stress development of CSA concrete and combination with LA

2.8.2 Visualization of Internal Curing Effect

In the past, there were researches (Lura, 2003) attempting to visualize the water transport from lightweight aggregate using ink. Firstly, lightweight aggregates were immersed in blue-ink solution and surface was dried, then cement paste was poured. At two weeks after casting, the blue ink corona was observed around the lightweight aggregate and the diffusion thickness reached to be 1mm. Figure 2.28 is the visualization of internal curing conducted Lura (Lura, 2003), which visualizes the water diffusion from lightweight aggregate to the cement matrix in a local region. The water transfer behavior from lightweight aggregate to cement matrix has been found by Maruyama (Maruyama *et al.*, 2009) using neutron radiography as well, which indicates the intensity of water inside the lightweight aggregate is reduced as time proceeds.

2. Early-age Deformation and Stress Development

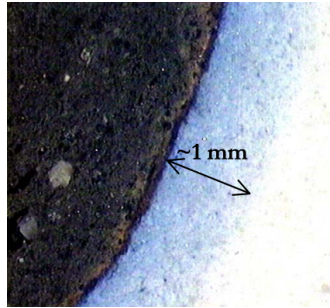


Figure 2.28 Visualization of internal curing effect of lightweight aggregate (after (Lura, 2003))

In this study, a new method to visualize internal curing effect is proposed. It is able to view the water distribution of lightweight aggregate at a larger scale, and it is easier without using ink. Firstly, the concrete beam (~6 to 7 days after casting) was broken into pieces, then the broken part was exposed to 30%~40% RH for around 4 hours. A special color agent (モレミール W from Taseto company) was sprayed on the specimen. As shown in Figure 2.29, Although being dried for some time, it can be observed that water is still left inside the large lightweight aggregates, and the water evaporation path is quite tortuous and long. Once water has been reached to the boundary, it will gradually diffuse further to the cement matrix, supplying required water for hydration of CSA to induce expansion. The diffusion depth (or thickness) is found to be around several mm. This phenomenon also implies lightweight aggregate can effectively acts as water reservoir for the CSA concrete.

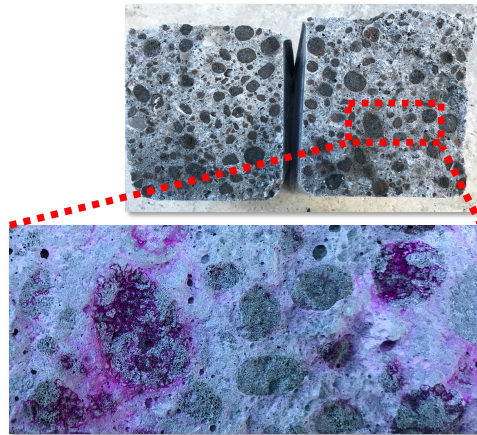


Figure 2.29 Visualization of internal curing effect using a new method

2.9 The Expansion Mechanism of CSA Concrete and Modeling

2.9.1 Discussion on expansion mechanism of CSA concrete

Even though the CSA-type expansive additive has been studied in and used in practices in many countries for a long time, the actual mechanism of its expansion is still under debate. Several major controversial mechanisms are listed in the following:

2. Early-age Deformation and Stress Development

- The most direct way is that the expansion could be explained by the increase of solid volume from formation of ettringite (Polivka, 1973), but it was also argued that it lacked the evidence to link expansion to amount of ettringite formation (Taylor, Famy and Scrivener, 2001). According to Mehta (Mehta, 1972), it is also pointed out that the expansion fails to be directly accounted by the increased volume of solids, on the basis of stoichiometric equations.
- The expansion is related to the adsorption of water by the colloidal sized ettringite crystals (Mehta, 1973). But it was also argued that crystalline ettringite will not show gel-like swelling behavior and such behavior has not been reported for synthetic specimens (Bizzozero, Gosselin and Scrivener, 2014).
- Expansion can be ascribed to the formation of crystallization pressure when ettringite crystals are generated (Bizzozero, Gosselin and Scrivener, 2014; Kolneath, 2021). This theory emphasizes the role of saturation degree of the solution. Supersaturation is considered to be the driving force for the development of crystallization pressure.

Based on the plausible mechanism of crystallization pressure, Pen (Kolneath, 2021) successfully implemented the expansion of CSA in DuCOM by considering the chemical kinetics and microstructural formation. Additional volume of ettringite and CH was incorporated into the original microstructural system of DuCOM. The caused crystallization pressure was evaluated from a proposed fictitious saturation index (SI). By this implementation, the restrained deformation of CSA specimen with steel bar could be reasonably quantified. However, there is still one unsolved issue:

- The modeled expansion of lower w/c case (e.g., w/c:0.3) was much larger than that of experiment.
- It should be also noted that previous experiments using TSTM (Lin, 2006) had offered us straightforward interpretations: 1. It was found that, a higher w/c will lead to a higher expansion. 2. The wet-curing condition (covering wet cloth after hardening) also generate higher expansion.
- Also, as per the discussion in the last section: CSA concrete cannot compensate the shrinkage effectively under high temperature condition, but its combination with lightweight aggregate can solve this problem.

If we consider these several features consistently with the experimental findings of last section in this study, one key point running through all of them is the availability of free water for hydration of CSA. It is plausible that the availability of free water for CSA will be in shortage easily, then the expansion of CSA will no longer be effective. That is the reason why CSA concrete fails to compensate shrinkage under high temperature, while a combined usage with lightweight aggregate can lead to more effective expansion for a longer time. The lightweight aggregates store some part of the water as large reservoirs, which supplies water for expansion when pore water becomes depleted. Also, one can deploy this concept to consistently explain the problems mentioned above. It is possible that due to the shortage of free water in low w/c (e.g., 0.30), the

2. Early-age Deformation and Stress Development

expansion is much suppressed. Additionally, due to the higher amount of free water in the high w/c concrete, the expansion will be higher. With a higher relative humidity offered by wet-curing, the expansion will be higher accordingly.

In the following discussion, the proposed model in this study mainly focuses on the concept regarding the availability of free water for CSA, and it is further implemented in the current coupled model.

2.9.2 Modeling of deformation and stress development of CSA concrete

Followed by the experimental results from last section, the expansion mechanism of both CSA concrete and CSA concrete with lightweight aggregate will be unfolded more comprehensively and the analytical model will also be established.

When predicting the hydration temperature of varied mix proportions, a multicomponent model proposed by Kishi (Maekawa, Chaube and Kishi, 1999) is used. In this multi-component model, Arrhenius's law of chemical reaction is introduced to express the mutual dependency of cement hydration, expressed by the following equations:

$$H_i = \gamma \beta_i \lambda \mu s_i H_{i,T_0}(Q_i) \exp \left\{ -\frac{E_i}{R} \left(\frac{1}{T} - \frac{1}{T_0} \right) \right\} \quad (2.20)$$

Where H_i is the heat generation rate of component i per unit weight of cement, H_{i,T_0} represents the reference heat generation rate of component i at constant temperature T_0 , γ is a coefficient expressing the delaying effect of chemical admixture and fly ash, β_i means the coefficient for reduction of hydration heat due to reduced availability of free water (precipitation space). λ expresses the change of the heat of generation rate of blast furnace slag and fly ash due to the lack of calcium hydroxide in the liquid phase. μ means the coefficient of difference of mineral composition of Portland cement. s_i represents the change of hydration heat due to fineness of powders. E_i is the activation energy of component and R the gas constant. And the accumulated hydration heat Q_i can be determined through integral:

$$Q_i \equiv \int H_i dt \quad (2.21)$$

One of the key parameters representing the free water availability is the β_i , expressed by

$$\beta_i = 1 - \exp \left\{ -r \left[\left(\frac{\omega_{free}}{100 \cdot \eta_i} \right) s_i^{1/2} \right]^s \right\} \quad (2.22)$$

Where the r and s are constants. It is determined that $r=5.0$ and $s=2.4$ for all components. ω_{free} is the free water ratio and η_i the thickness of internal reaction layer of component i .

In this study, in order to simulate the rapid drop of free water for CSA concrete, a separated β_{CSA} is proposed for the CSA component. And the expression of expansion rate is in a similar mathematical form as the hydration heat model, as shown in Eq. (2.23). In this way, it is able to directly link the expansion with free water availability, which can reasonably explain the unsolved

2. Early-age Deformation and Stress Development

discrepancies between experiment and model, as depicted previously. Additionally, this mathematical expression is a simplified way to evaluate the interdependence between factors (temperature, dosage and free water availability), similar with the treatment of hydration heat model (Maekawa, Chaube and Kishi, 1999).

$$\dot{\epsilon}_{CSA} = 6P_{CSA}\beta_{CSA}(T - T_0)^{0.9} \quad (2.23)$$

The accumulated expansion at certain time step could be determined as

$$\epsilon_{CSA} = \int \dot{\epsilon}_{CSA} dt \quad (2.24)$$

Where P_{CSA} is the dosage of CSA concrete, β_{CSA} is the free water reduction parameter, and T the temperature (K), T_0 the reference temperature (K).

The free water amount inside the CSA concrete will be lower due to a stronger self-desiccation effect (1.0 gram of CSA needs 0.90 gram of water for full hydration). It is considered that only a part of the common free water could be used for the expansion of CSA, as shown in the following equation,

$$\omega_{free,CSA} = f_{acc}(t) \cdot \omega_{free} \quad (2.25)$$

In which, the $f_{acc}(t)$ is a time-dependent function to consider the portion of free water accessible for CSA component, and for single use of CSA, $f_{acc}(t) = 0.71 \cdot \exp(-t)$, in which t is the time in days. The r and s are kept the same as 5.0 and 2.4 respectively. For a combination of CSA and light aggregate, the $f_{acc}(t) = \exp(-t^{0.05})$, and the r and s are 5.0 and 1.1, respectively. The physical meaning behind these selected parameters is that, due to some blockage of pores during the formation of hydration products, discontinuity of pore structure takes place. The rapid loss of free water availability of CSA can be attributed to the less amount of free water and also, the discontinuity of pore structure which hinders the water accessibility.

The rest of the computation, including the thickness of the component η_i and the fineness of component s_i could be kept identical with the original hydration heat model. By this treatment, the free water reduction β_{CSA} could be shown as the following Figure 2.30. The chemical component in OPC including C_3A , C_3S , C_4AF and C_2S is the same as the original hydration heat model. The separated β_{CSA} reveals a much rapid drop during the first several days, however, with a combined use with lightweight aggregate, the drop of water becomes less sharp.

2. Early-age Deformation and Stress Development

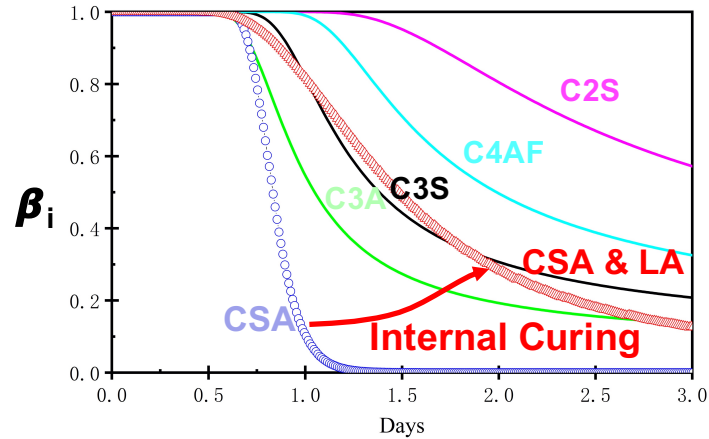


Figure 2.30 Parameter of free water availability

By the formulated equations, the free deformation could be computed. As shown in Figure 2.31, the left panel shows the free deformation under high temperature condition and right panel shows that under low temperature condition. The experimental data from Lin (Lin, 2006) is also summarized. The analytical results can capture well the expansion of CSA concrete and also, the shrinkage development for both the high and low temperature cases. It is noteworthy that, under low temperature case, the expansion effect of E40C45L is larger than the shrinkage, therefore, the specimen will have a small portion of continued expansion. The effect of interdependence between dosage, temperature and free water availability can also be simulated in this manner. Also noted that by such a mathematical treatment, the time of free water availability corresponds well to the time for effective expansion. As shown in Figure 2.30, the free water availability becomes very low at around one day, which also indicates that the expansion is almost completed in this time point, in agreement with the experimental data in Figure 2.31. Whereas, the addition of lightweight aggregate could prolong this expansion period for several days. The mathematical treatment provided here is only one alternative to address the prediction of deformation and stress development. The value of parameters can be further optimized with more experimental data provided. However, the proposed free water availability is a universal concept that can consistently address all the unsolved experimental findings. This physical understanding can be used in any other multi-scale FEM model for more complex engineering problems.

Noted that the water from the original lightweight aggregate (~26% of the water content) may slightly increase the actual w/c ratio, but this effect is minor. Previous study by Lin using oven-dried lightweight aggregate has shown very similar stress evolution as the original lightweight aggregate and it was concluded that the effective expansion does not depend on the saturation degree of lightweight aggregate (Lin, 2006). Therefore, the effect of the possibly slight increase of actual w/c using original lightweight aggregate is not taken into consideration of the current model.

2. Early-age Deformation and Stress Development

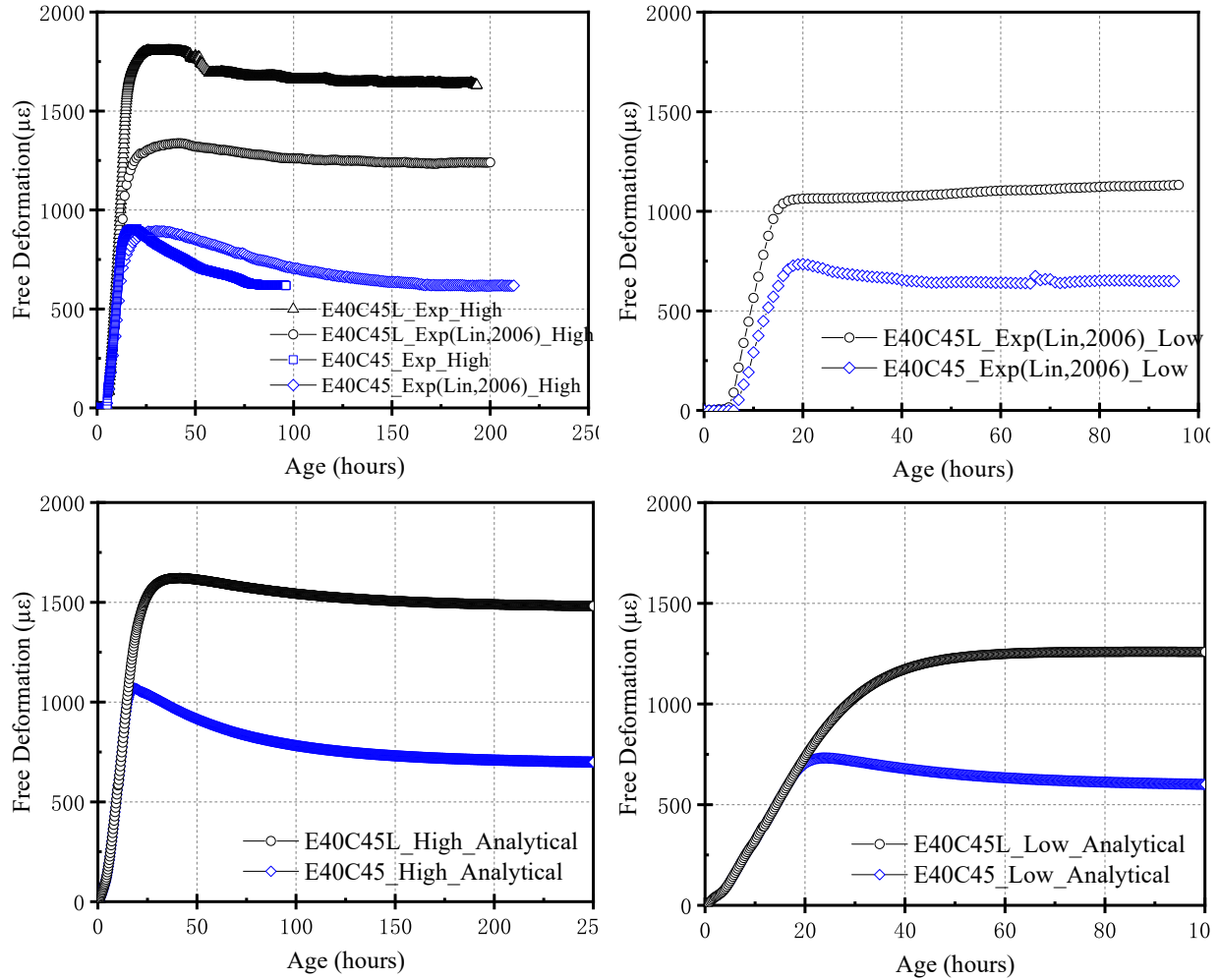


Figure 2.31 The prediction of free deformation of CSA concrete with/without LA. Left: High Temperature, Right: Low Temperature

The prediction of modulus could be achieved if the modulus of aggregate is given. In the modeling, the modulus for normal aggregate is used as 60 GPa and that of lightweight aggregate is used as 20 GPa. These values are within the range given by Mehta (Mehta and Monteiro, 2006).

The optimized parameter for the relaxed stress of expansive concrete is also listed in the following. $f_r=0.85$, which signifies around 85% of the stress is relaxed due to the applied stress. $R_{max}=2.0$, which means that there is around 2.0 MPa of the time-dependent relaxed stress. These values are much larger than that of OPC concrete, which agrees with the statement from Choi (Choi *et al.*, 2015) that, expansive concrete will have much greater early-age creep effect. Noted that not all of the free deformation formed by expansive concrete can be converted to restrained stress owing to the early-age creep effect. The possible mechanism may be related to the formation of loosely-structured ettringite. Under stressed state, loose ettringite products cannot sustain the load effectively, leading to the higher stress relaxation effect.

2. Early-age Deformation and Stress Development

The rate constant is found out to be $K_r=0.4$ for high and low temperature condition. By optimization of the early-age creep effect, the stress development of CSA concrete with/without LA can be predicted. As shown in Figure 2.32, the simulated restrained stress corresponds quite well with the experimental data of both high and low temperature conditions.

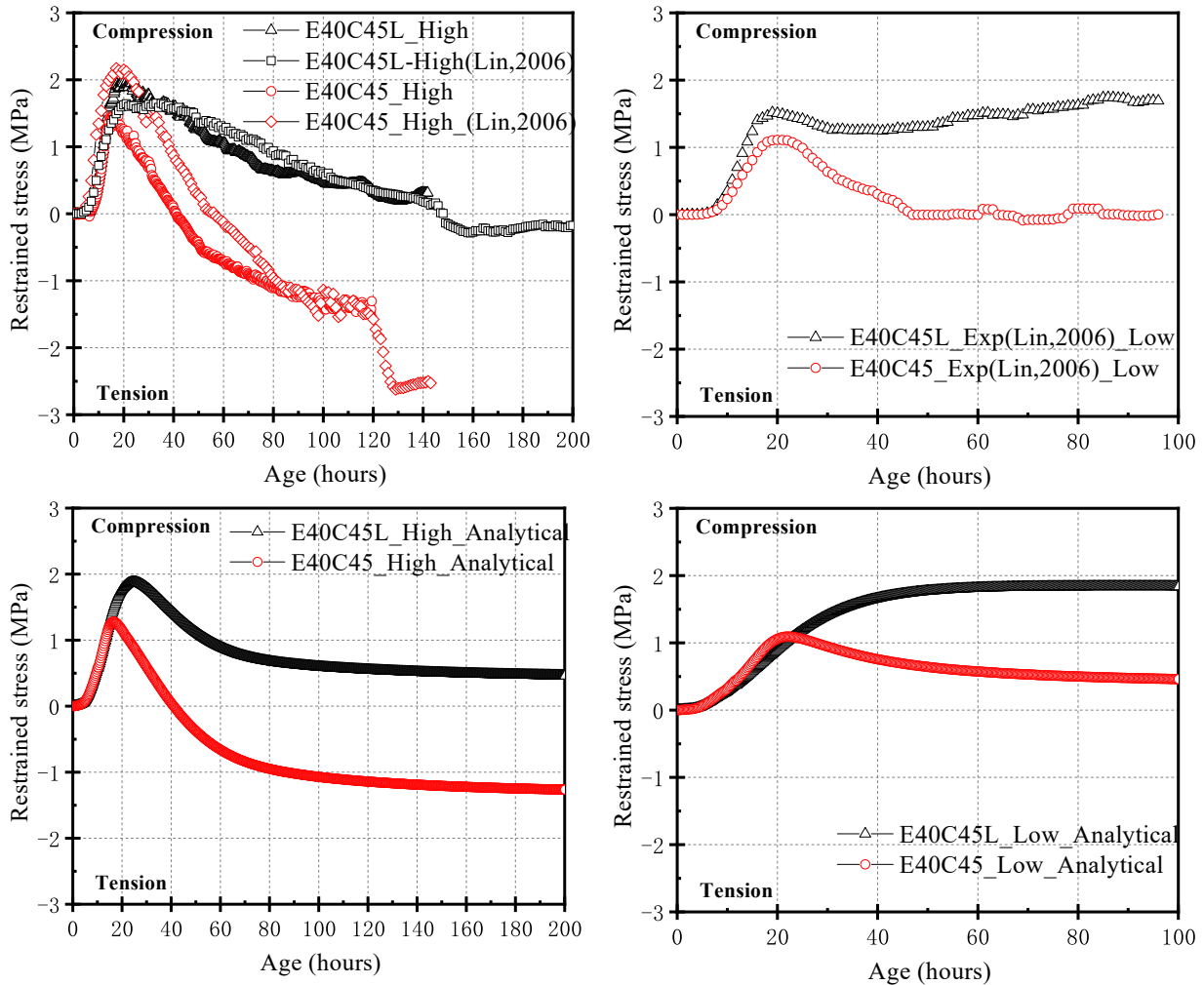


Figure 2.32 The prediction of full-restraint stress of CSA concrete with/without LA. Left: High Temperature, Right: Low Temperature

2.10 The Expansion Behavior of MgO Concrete

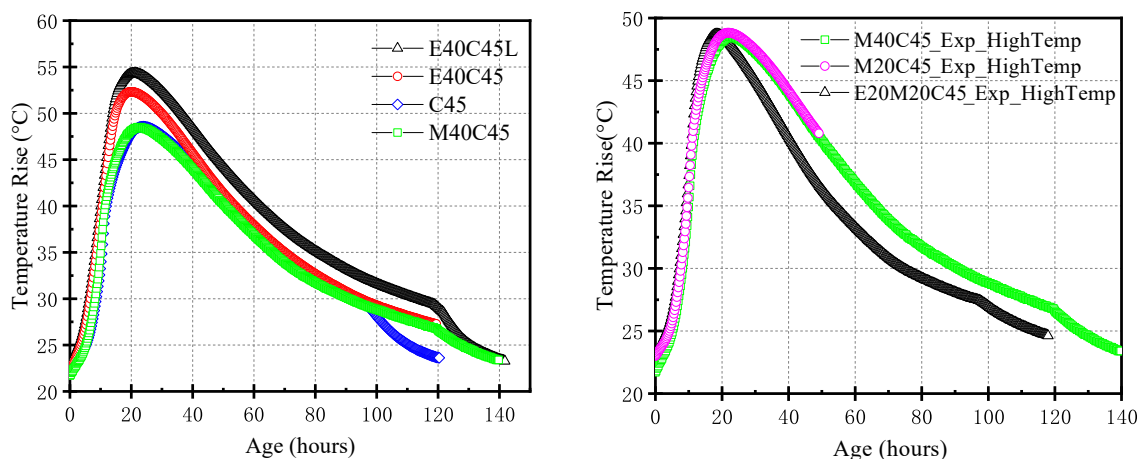
In this section, the cracking performance of a relatively new expansive additive MgO will be discussed. This material has been used in more than 30 concrete dam structures in China, including the well-known three gorges dam. Two rapid types of MgO are acquired from two suppliers in China to understand their cracking performances. Physical properties of these expansive additives are listed in Table 2.1. Type-I MgO is from a supplier which claims to be one

2. Early-age Deformation and Stress Development

of the suppliers of the MgO used by three gorges dam. Type-II is obtained from Prof. Mo(Mo *et al.*, 2014). Even though the number of recent reports on expansion properties of MgO is increasing, most of the previous publications were written in Chinese. Additionally, the study of restrained stress development of this expansive additive is quite limited, while most of the published studies mainly focus on the properties of free deformation (Zheng, Xuehua and Mingshu, 1991; Mo, Deng and Tang, 2010; Mo, Deng and Wang, 2012). Due to the high requirement on experimental set-up, the very early-age behaviors (starting from casting) are seldom reported. With the aid of TSTM, these behaviors can be more comprehensively and deeply evaluated. In this section, attempts to achieve acceptable cracking performance without the usage of lightweight aggregate is made, as the use of lightweight aggregate will lead to higher economic cost and lower compressive strength (Table 2.5).

2.10.1 Stress Development of Type-I MgO

The restrained stress under high temperature condition is tested, as shown in Figure 2.33. Here in, the dosage of MgO and the combination of MgO and CSA are all tried. From the green line of the left panel, it can be seen that the temperature development of M40C45 (10%, Type-I) is quite similar with that of CSA concrete. Up to around 20 hours, the compressive stress generated by MgO is lower than that of CSA, due to a slower and smaller expansion. When temperature starts to drop, the development of tensile stress is less than CSA, and finally it evolves to quite similar value of tensile stress as the CSA. And the tensile stress is around 1.5MPa. On the right panel, the effect of dosage is also tested. When the dosage is only 5% (M20C45), the generated compressive stress is smaller than M40C45, with only around 0.5MPa of the compressive stress. The development of tensile stress is also relatively rapid, and it cracks with around 0.8MPa of the tensile stress on second day. The combination of MgO and CSA does not show improvement to the cracking performance, shown as the black line on the right panel (E20M20C45).



2. Early-age Deformation and Stress Development

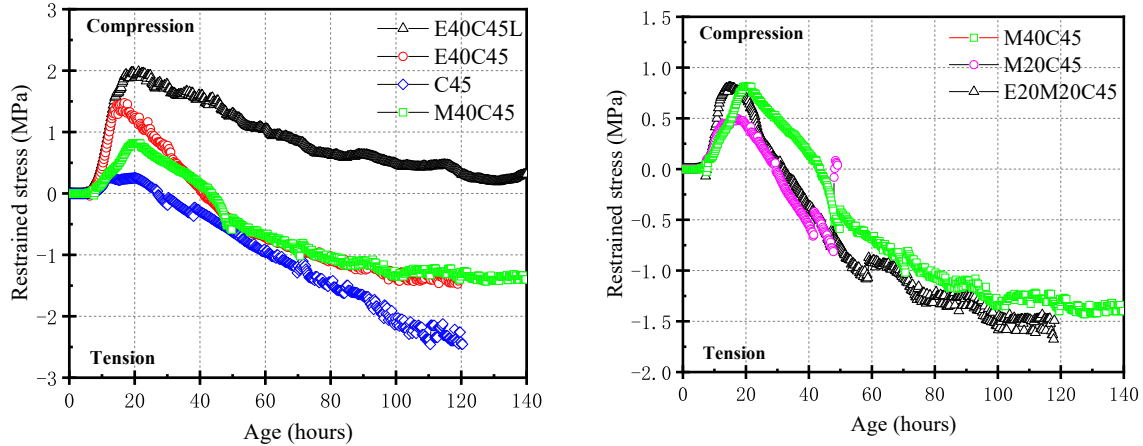


Figure 2.33 Full-restraint stress development of MgO concrete with varied mix proportions

2.10.2 Stress Development of Type-II MgO

Figure 2.34 shows the results with respect to the stress development of Type-II MgO concrete under high temperature condition. The top panel denotes the temperature history, which shows that Type-II MgO concrete has a similar temperature development as Type-I MgO and CSA concrete. Interestingly, in comparison with Type-I MgO, the Type-II MgO concrete reveals a more effective and prolonged expansion effect under this strict criterion of high temperature and full restraint condition. The maximum tensile stress of type-II MgO is around 1 MPa, which is smaller than that of type-I MgO and CSA concrete (~ 1.5 MPa). When the temperature of the specimen almost returns to the original casting temperature at the 120th hour (It means that the thermal shrinkage has almost completed), it keeps on expanding for more than 2 days (~ 160 th hour). The actual expansion time may not be fully ceased even after one month. Due to the limited time, the later period is not studied currently. It should be noted that there is a small peak of stress at around 140 hour, that is due to the unexpected disturbance of room temperature. After the disturbance, room temperature is recovered. The behavior of prolonged expansion is not found for Type-I MgO and the normal CSA concrete, which indicates Type-II MgO concrete has a lower cracking sensitivity than Type-I MgO concrete and CSA concrete, with just around 1.0 MPa of the maximum tensile stress and this tensile stress is compensated by the prolonged expansion at later time. It reveals a potential application in practice to mitigate early-age cracking even under strict temperature and restraint condition, without using lightweight aggregate and compromise of the strength.

It is noteworthy that there is a difference of chemical kinetics between the CSA concrete and MgO concrete. In the stoichiometric equations given in **section 1.1**, it can be interpreted that for the complete hydration of CSA, 1 gram of CSA needs around 0.85-0.90 gram of the water, while MgO requires only around 0.45 gram of the water. Due to much less requirement for water, the MgO concrete can still expand at later time, while the expansion of CSA concrete (without addition of lightweight aggregate) is depleted at around one day.

2. Early-age Deformation and Stress Development

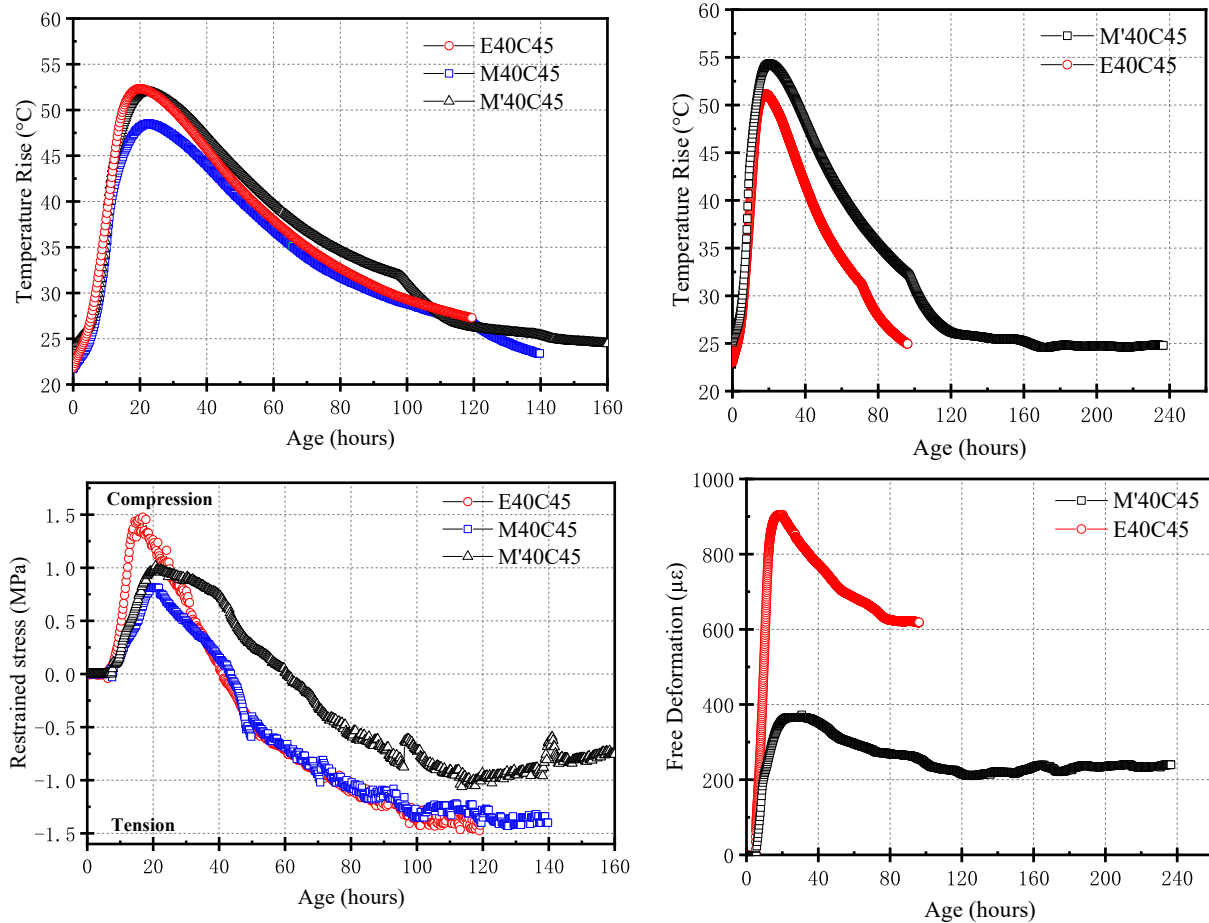


Figure 2.34 Stress development and free deformation of Type-II MgO concrete

The free deformation tests are further conducted for ~10 days to confirm about the compensation effect on shrinkage for type-II MgO. As shown in the right panel of Figure 2.34, the free deformation of CSA and type-II MgO under high temperature conditions are compared. Even though type-II MgO shows less than 50% of the expansion of CSA at the beginning, the shrinkage value (160μ ϵ) is much less than CSA (290μ ϵ) when temperature starts to decline. It indicates that MgO can offer prolonged expansion, making it outperform the normal CSA concrete. When the temperature is eventually stabilized at the original room temperature at around 160 hours (thermal shrinkage becomes insignificant), the expansion still continue for at least 10 days. But this prolonged expansion of lightly-burnt MgO won't last for years and cause the damage of the structure, as reported for the dead-burnt MgO. It is reported that it may last for several months (Mo *et al.*, 2014). Generally, the MgO with higher reaction activity will stop the hydration earlier. The 28-day compressive strength of both type of MgO concrete also show no much difference with the normal OPC concrete, as shown in Table 2.5.

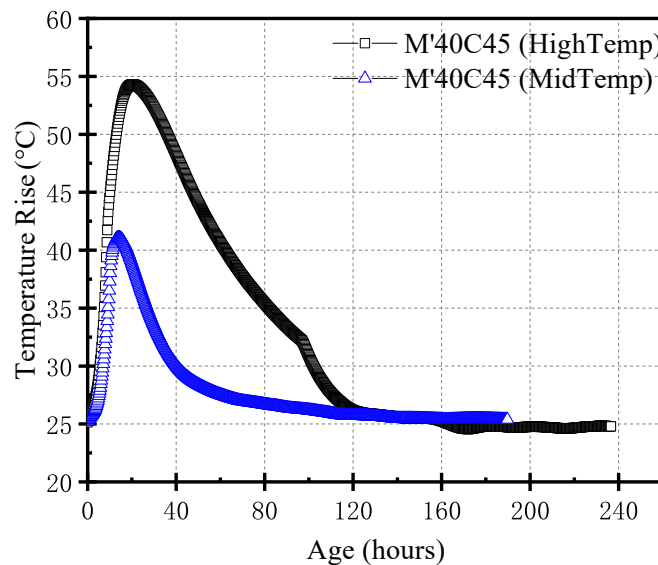
The modeling of the deformation and stress is not provided, which can be formulated using the similar computation flow of CSA. But actually, if one compares both of the stress development and free deformation of CSA and MgO in Figure 2.34, it reveals that even though at the very

2. Early-age Deformation and Stress Development

beginning, the expansion value of MgO is less than half of CSA, the generated compressive stress ($\sim 1.0\text{MPa}$) under a full-restraint condition is not too much lower than CSA ($\sim 5.0\text{MPa}$). It implies that, the early-age creep effect of MgO concrete will be lower than CSA. It might be related to the different mechanical properties of hydration products. The hydration product of MgO is brucite, possessing a much higher density than ettringite. In comparison to ettringite, it may act as a stronger load-bearing medium and reduce the effect of stress relaxation. Interestingly, as shown in the next chapter, the pore structure of MgO is quite similar with OPC, while CSA pastes show a coarser pore structure.

2.10.3 The effect of different temperature conditions

The free deformation under medium temperature condition is also tested and compared with the high temperature condition. The medium temperature condition means that, heater is turned off with only insulation formworks covering outside the specimen. As shown in Figure 2.35, The blue line denotes the tested temperature history, with around 15°C of the temperature increase. It can be observed that, the maximum expansion is around $200\ \mu\epsilon$, much lower than the high temperature case. Since the expansion is related to the temperature condition, a higher temperature condition will generate more expansion. When temperature starts to drop, the shrinkage value is around $60\ \mu\epsilon$. At around 60th hour, even though the temperature is still declining, the shrinkage is all compensated and expansion takes place. The prolonged expansion can be clearly observed after 60 hours. It can be further confirmed that MgO shows prolonged expansion, which can compensate the shrinkage in a longer time.



2. Early-age Deformation and Stress Development

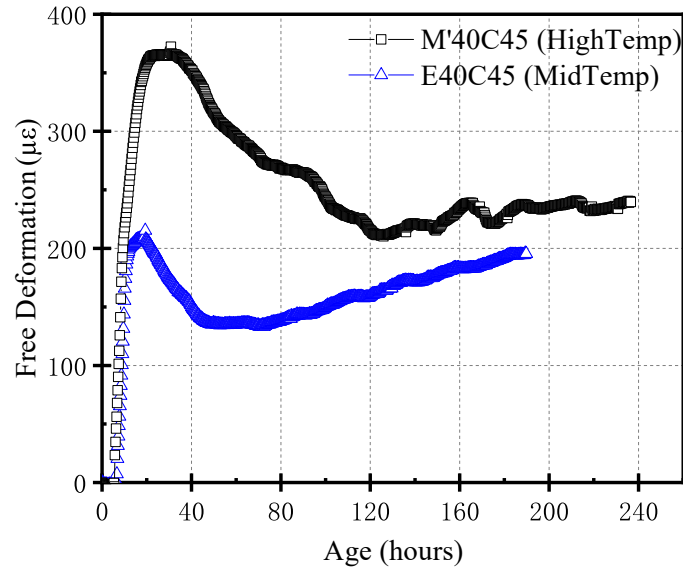


Figure 2.35 Comparison of free expansion of type-II MgO under varied temperature conditions

2.10.4 Calcination condition and reactivities of MgO concrete

As discussed in **section 1.1**, various calcinations result in different reaction activities for MgO. A lower calcination temperature and shorter time can produce MgO with higher reactivity. Due to the difference of expansion effects found from TSTM experiments, reactivities of MgO have also been determined using neutralization method. 1.70 gram of the MgO is used to completely neutralize 200 mL of 0.07mol/L citric acid at 22 °C (not 30 °C as stated in (Mo, Deng and Tang, 2010)). The time for neutralization is measured, which is used as an index of reactivities. A shorter neutralization time simply means higher reactivity. 0.04% (w/v) Bromothymol Blue Indicator (BTB solution) is used to judge if the citric acid is neutralized or not. If the color of the solution is changed from yellow to light green, it is regarded as being neutralized, and the time from beginning to this time point is used as the neutralization time, as shown in Figure 2.36. Color change during titration is a common and easy method for researchers and engineers, but it is argued that variations from measurements may also be induced by different operators. To reduce this effect, an advanced sensitive PH meter (From METTLER TOLEDO company) with high accuracy is also used for double-check. Since the response time of this PH meter is just several seconds, the accuracy is enough for this measurement. It is found out that the difference between the color change method using BTB solution and PH meter is less than 10 seconds. Therefore, both methods could be used in practice.

The tested neutralization time for type-I MgO is around 220-232s while that of type-II is around 160-169s. Please noted that the measured neutralization times are different from the information offer by supplier (Table 2.1). The neutralization method used by the supplier is conducted under 30 °C. Both types are reported as 90 -120s, while in this study a clear difference of neutralization time is found. The differences of reactivity are also validated by TSTM experimental results.

2. Early-age Deformation and Stress Development

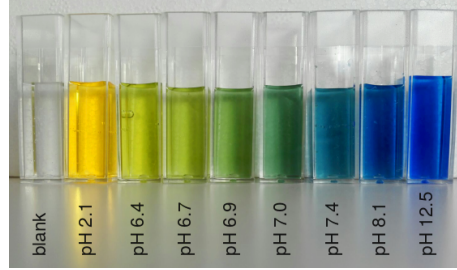


Figure 2.36 Color change from yellow to light green as an indicator of neutralization (After Wikipedia).

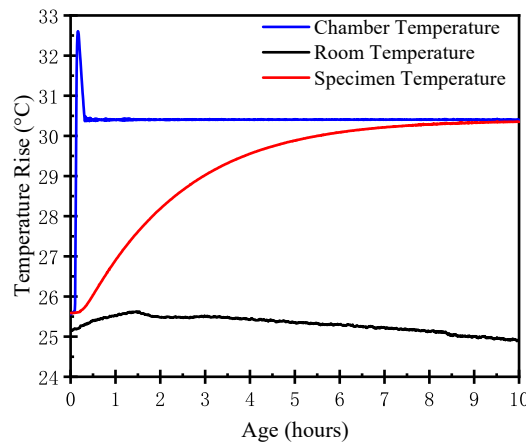
Specific surface area of dried powder is also determined by nitrogen adsorption-desorption test. The measured surface area of type-I MgO is $S_{BET} = 17.58 \text{ m}^2/\text{g}$ and that of the type-II MgO is around $22.25 \text{ m}^2/\text{g}$. The results regarding surface area also supports that type-II MgO has a higher reactivity.

2.10.5 Measurement of Thermal Expansion Coefficient (TEC)

This section discusses about the method to determine thermal expansion coefficient (TEC) using TSTM. The TEC after hardening can be tested by varying the temperature for certain degree Celsius and testing the corresponding thermal deformation. Then the TEC can be determined by the following equation:

$$\alpha_h = \frac{\Delta \varepsilon}{\Delta T} \quad (2.26)$$

Where α_h represents the thermal expansion coefficient ($\mu\text{e}/^\circ\text{C}$).



2. Early-age Deformation and Stress Development

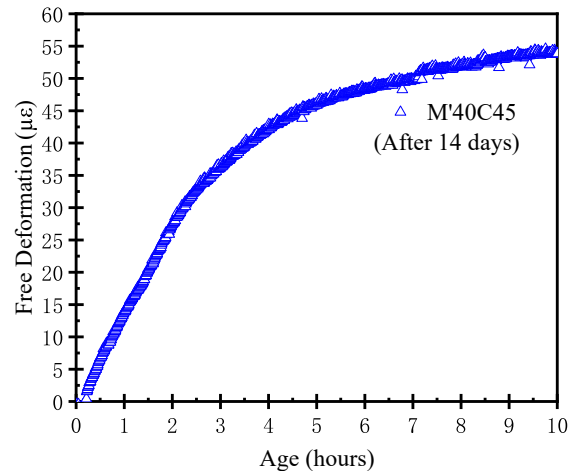


Figure 2.37 Measurement of TEC using TSTM

Figure 2.37 shows the testing result for type-II MgO concrete after 14 days of the casting. Top panel of the figure represent the temperature conditions. The black line represents the room temperature, it shows certain fluctuation. The blue line represents the temperature of the chamber, which can be controlled by the system. In this study, increment of 5 degree Celsius is applied into the chamber, and correspondingly the temperature of the specimen will gradually be increased, which is depicted by the red line. The concrete will start to expand, as reflected in the blue scattered points in the lower panel. After being heated about 10 hours, the temperature of the specimen is increased to be identical as the chamber temperature and become stable later. In this manner, the relationship between specimen temperature and the expansion can be determined. It is found out a very good linear relationship ($R^2=0.99$, not plotted for simplicity) between the tested specimen temperature and expansion, and the slope is around $11 \mu\epsilon/^\circ\text{C}$. Since the sealed concrete has been cured for 14 days and the tested duration is 10 hours only, so it can be considered mostly the detected deformation is thermal expansion, with negligible autogenous shrinkage, drying shrinkage and artificial expansion. In this section, it offers one way to measure TEC using TSTM. The same method can be applied to trace the time-dependent development of TEC, for example, with interval of one day. It is also reported by some researchers that the TEC will be increased to some extent at later time due to the self-desiccation effect (Nguyen *et al.*, 2019b).

2.11 Cracking Sensitivity under Wetting-Drying Cycles

The early-age deformation and stress development under sealed condition can adequately reflect the cracking sensitivity without drying shrinkage. In the realistic construction site, drying effect is also induced sometimes. To study the cracking performances of expansive concrete under drying, the restraint stress developments of both CSA and MgO concretes under wetting-drying cycles are measured and compared for the first time (to the author's best knowledge), which offers us valuable insights for their actual performances under realistic engineering conditions. After a high temperature condition and cured for around seven days (temperature of specimen has

2. Early-age Deformation and Stress Development

stabilized at the room temperature, so thermal effect is limited), wet cloths are put on the top of the TSTM specimen. Then, the specimen is sealed by double-layer plastic sheet again to simulate a wetting condition. Noted that, in order to reduce the effect of temperature exchange between wet cloth and the specimen, the wet cloth has already been submerged in water tanks with the same room temperature for at least one day. After one-day wetting, the sealed plastic sheets are opened, and wet cloths are removed. The specimen is then exposed to drying condition (30-40% RH) for three days. After the drying period, the specimen is wetted by the aforementioned method for one day again. In this manner, a 1D drying- 3D wetting- 1D drying cycle is conducted.

As shown in Figure 2.38, the CSA concrete is marked as red line, type-I and type-II MgO concretes are symbolized by blue and black lines respectively. The green circle with letter “W” represents the time point to apply wetting condition while “D” denotes drying. Very interestingly, it can be found out that CSA concrete reveals very rapid development of stress under wetting-drying cycle. The shrinkage stress developed for three days can reach up to 1.8 MPa, starting from ~1.0 MPa of the compressive stress to ~0.8 MPa of the tensile stress. This immediate and rapid development of shrinkage stress indicates a high cracking sensitivity under drying condition in reality. When this shrinkage stress is coupled with other heavy mechanical loading applied in the field, it may crack easily. But in terms of type-II MgO concrete, it is surprising that even drying has been started, retarded expansion is found to be continued for around one day. When specimen starts to shrink under drying, the development of shrinkage stress is much slower than CSA concrete. As shown in the right panel of Figure 2.38, type-II MgO concrete reveals similar phenomena. The stress development is slightly sharper than type-I but much smoother than CSA. A retarded expansion is found again at around 50th hour, which also lasts for around one day. The development of shrinkage stress of both types of MgO concretes is much slower than CSA concrete. It can be concluded that MgO concrete reveals much better resistance to drying stress than CSA concrete under wetting/drying cycles. The reason can be attributed to: (1) The occurring of retarded expansion, which associates with the less water dependency for further hydration than CSA, as discussed previously. (2) The finer pore structure, which hinders the water evaporation process under drying. The effect of pore structure will be discussed in the next chapter. By wrapping up these experimental findings, we can figure out that type-II MgO concrete not only shows a potential to compensate thermal shrinkage even under high temperature and full restraint condition, but also, it is able to mitigate the drying stress in a longer time. More comprehensive study on its mechanical property could be studied in the future, including fatigue behavior and long-term creep effect, since creep effect is greatly linked with drying shrinkage. Additionally, optimization of mix design can also be conducted for better usage and economical purposes.

2. Early-age Deformation and Stress Development

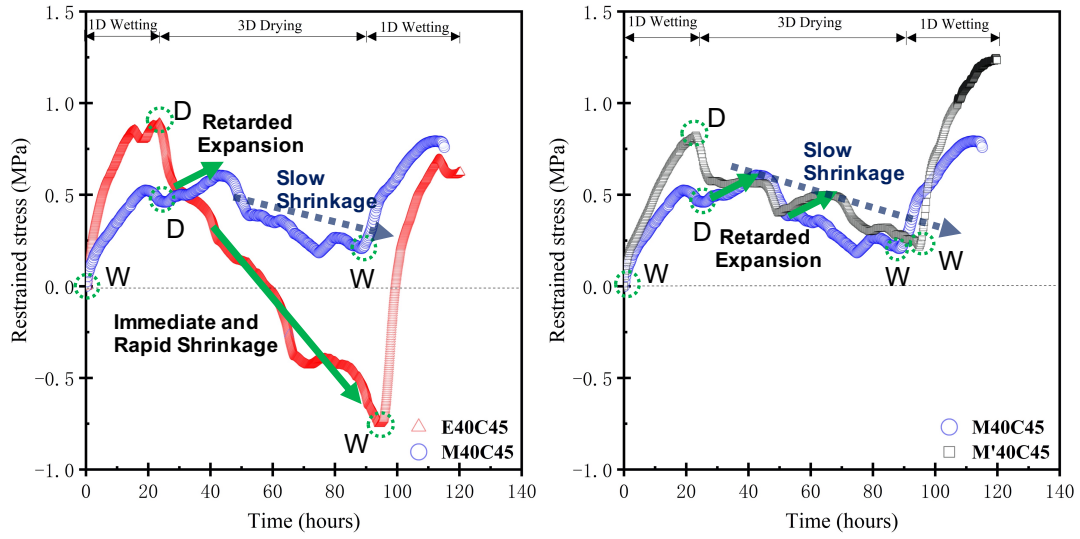


Figure 2.38 Stress development of MgO concrete and CSA concrete under wetting/drying cycle

3. The Thermo-Hygro-Mechanical Model

In this chapter, the development of pore structure will be discussed. This pore structure will be implemented into the coupled thermo-hygro-mechanical scheme, so that the moisture state inside the porous material can be quantified on the basis of thermodynamics. The basic attempt of this study is to simplify the prediction of free deformation and stress development reasonably. In order to achieve this attempt, a constitutive law is proposed by consideration of mutual interaction between aggregate and cement matrix. It can transform the computed free deformation into full-restraint stress by a proper consideration of elastic modulus and early-age creep. And this problem now traces back to how to determine the free deformation. In a sealed condition, the drying shrinkage can be avoided. The free deformation can be computed by a summation of thermal deformation, autogenous shrinkage and artificial expansion induced by addition of expansive additive (same as Eq. (1.7) in Chapter 1).

As an easiest solution to this problem, empirical equations which simply links the variables of mix proportions to the free deformation could be possibly formulated. However, setbacks of such a highly empirical method are apparent. Firstly, under varied insulation conditions, the temperature history will be quite different. Without more sophisticated consideration of hydration heat caused by varied chemical components, the temperature development could not be simulated and understood properly. Secondly, as found by the experiment, the free water availability plays a key role in the effectiveness of expansion. The expansion value is also related to the temperature. The prediction of artificial expansion is not feasible without the consideration of these factors. Simple empirical formulas to directly link mix proportions with free deformation lacks applicability and it cannot take into account the interdependence between factors. For example, when mix proportions are changed (e.g., varied w/c and addition of lightweight aggregate), the free water availability will also change drastically. Temperature conditions in different engineering projects may also vary significantly, which also alters the expansion value.

Thus, to properly quantify these effects on the free deformation, a coupled model which is able to comprehensively consider moisture state and temperature condition is much more preferable. Noted that in this coupled scheme, the moisture state is always related to and should be discussed in the context of a given pore structure. According to the thermodynamics (Laplace-kelvin equation), the pores smaller than certain radius will be saturated at given relative humidity. Therefore, the pore structure (e.g., the porosity of capillary pores, inter-hydrate pores, gel pores and interlayer pores and their pore size distributions) will determine the amount of water

3. The Thermo-Hygro-Mechanical Model

evaporated/left inside a pore with specific size. Each part of this coupled process should be evaluated rationally, i.e., the hydration process, pore structure and moisture state.

In the contemporary age, the understanding on pore structure has been advanced owing to new and interesting experimental findings (SANS, SAXS, and NMR, etc.) and theories. Therefore, different from the previous pore structure model in DuCOM (Maekawa, Chaube and Kishi, 1999), a new pore structure model is proposed in order to better elucidate the role of each group of pores and evaluate its moisture state. Through a more realistic treatment on pore structure, it is expected that (1) The physical mechanism behind the ineffective expansion of CSA can be better understood by the analytical model. (2) Though qualitatively, insights on the influence of pore structure on several unsolved drying behaviors could be acquired.

In the following discussion, the hydration model and the moisture isotherms will be briefly introduced (with most of the details already given in DuCOM (Maekawa, Chaube and Kishi, 1999)), since the current coupled model formulated in this study mostly keeps the hydration model and moisture isotherms the same as DuCOM. After that, the computation flow and scheme of the current coupled model will be presented. Finally, the proposed new pore structure model will be discussed.

3.1 The hydration heat model

Major minerals in the cement consists of the alite (C_3S), belite (C_2S), aluminate phase (C_3A) and the ferrite phase (C_4AF). The portion of each component varies for different types of cement. The heat of hydration can be computed in the way that the total heat of hydration is a summation of heat generated by varied components. However, the accurate prediction of hydration process also relies heavily on the interdependence between components. In the hydration heat model proposed by Kishi (Maekawa, Chaube and Kishi, 1999). The following equation is used for the modeling of their mutual dependence, which conforms to the Arrhenius' law.

$$H_i = \gamma \beta_i \lambda \mu s_i H_{i,T_0} (Q_i) \exp \left\{ -\frac{E_i}{R} \left(\frac{1}{T} - \frac{1}{T_0} \right) \right\} \quad (3.1)$$

Where H_i is the heat generation rate of component i per unit weight of cement, H_{i,T_0} represents the reference heat generation rate of component i at constant temperature T_0 , γ is a coefficient expressing the delaying effect of chemical admixture and fly ash, β_i means the coefficient for reduction of hydration heat due to reduced availability of free water (precipitation space). λ expresses the change of the heat of generation rate of blast furnace slag and fly ash due to the lack of calcium hydroxide in the liquid phase. μ means the coefficient of difference of mineral composition of Portland cement. s_i represents the change of hydration heat due to fineness of powders. E_i is the activation energy of component and R the gas constant. And the accumulated hydration heat Q_i can be determined through integral:

3. The Thermo-Hygro-Mechanical Model

$$Q_i \equiv \int H_i dt \quad (3.2)$$

By using this hydration heat model, the adiabatic temperature development of any mix proportions could be well predicted. The validation of the hydration heat model is shown in Appendix. Noted that the relationship between time and hydration degree under varied temperature conditions can also be extracted from the model.

3.2 Moisture Isotherms

The mathematical formula moisture isotherms used in the established coupled model are kept the same as that proposed by Ishida for DuCOM (Maekawa, Ishida and Kishi, 2009), which is capable of quantifying the moisture state inside a given pore structure. The formulations provided offers very practical values, which could be implemented for any pore size distribution. In the following, some basics will be introduced. According to thermodynamics, The pressure difference due to capillarity in a liquid-vapor interface can be expressed as

$$P_l = \frac{-2\gamma}{r} \quad (3.3)$$

Where P_l represents the negative pressure that liquid water is subjected to (Pa), and γ the surface tension of liquid water (N/m), r the radius of a pore (m).

Due to the equilibrium at the interface, the kelvin's equation can be given:

$$P_l = \frac{\rho_l RT}{M_w} \ln \frac{P_v}{P^*} = \frac{\rho_l RT}{M_w} \ln h \quad (3.4)$$

Where ρ_l represents the density of liquid water (kg/m^3), and M_w the molar volume of liquid water (m^3/mol). R is the gas constant (J/mol K), T the temperature (K) and P_v/P^* represents the ratio of vapor pressure to saturated vapor pressure which is also relative humidity (RH).

Subsequently, the well-known Laplace-kelvin equation determines the saturation condition of a cylindrical pore with radius of r_s under ideal condition, as shown in Eq. (3.3).

$$r_s = \frac{2\gamma M_w}{\rho_l RT} \frac{1}{\ln h} \quad (3.5)$$

It can be interpreted that under a certain relative humidity h , pores with a radius smaller than r_s will be saturated, while those larger than that will be emptied. However, the effect of absorbed water should also be considered, which can be determined by the Hillerborg Equation (Hillerborg, 1985).

$$t_a = \frac{0.525 \times 10^{-8} h}{(1 - h/h_m)(1 - h/h_m + 15h)} \quad (3.6)$$

Where h_m denotes the humidity to fully saturate a pore.

$$h_m = \exp\left(\frac{-\gamma M}{\rho RT r_1}\right) \quad (3.7)$$

3. The Thermo-Hygro-Mechanical Model

Where $t=r-t_a$ is the actual interface radius. The degree of saturation of a cylindrical pore could be expressed as:

$$S_r = 1 - \left(\frac{r - t_a}{r} \right)^2 \quad (3.8)$$

The degree of saturation of all groups of pores could be readily integrated over the whole range. Correspondingly, after considering the absorbed water, the equilibrated interface radii r_c can be considered as 2.15 times the r_s determined from Laplace-kelvin equation.

Under wetting state, the total saturation of pore smaller than

$$S_{total} = \int_0^{r_c} \Omega dr = \int_0^{r_c} dV \quad (3.9)$$

Where $\Omega = dV/dr$ represents the porosity distribution function. Under drying, the entrapped pore water due to ink-bottle effect can be estimated by

$$S_{ink} = \int_{r_c}^{\infty} f_r dV = \int_{r_c}^{\infty} \frac{S_c}{V} dV \quad (3.10)$$

Where $f_r = V_{rc}/V_r$ is a probability function for consideration of entrapped water in pores. V_{rc} represents the volume of the pore volume of pores with radius smaller or equal than r_c and V_r is the volume of pores with radius smaller or equal than the concerned radius r . Noted that the above mathematical treatment on the consideration of moisture isotherm in DuCOM (Maekawa, Ishida and Kishi, 2009) does not depend on a certain pore size distribution, which means any pore size distribution can be computed accordingly. It facilitates the incorporation of a new pore structure, as discussed in the following sections. The actual saturation of the porous media S can be therefore computed as:

$$S = S_{total} + S_{ads} \quad (3.11)$$

Where S_{ads} denotes the absorbed component of saturation. Using this scheme, a computed moisture profile for a random pore size distribution under relative humidity of 50% is shown in Figure 3.1. The saturation degree in pores with any size could be estimated, and by integrating the saturation condition over the whole range of pore, the total saturation or actual saturation could be computed.

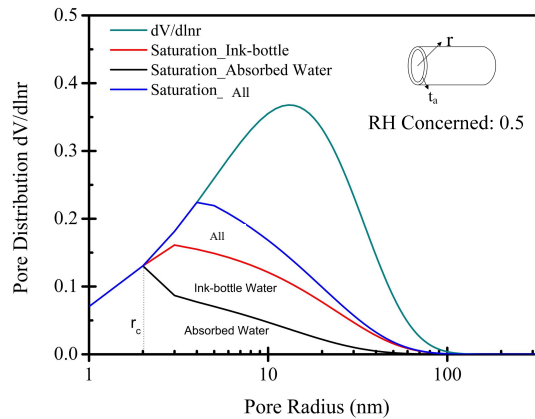


Figure 3.1 An example of computed moisture state in a random pore size distribution profile

3. The Thermo-Hygro-Mechanical Model

As for the contribution of interlayer moisture, the hysteresis behavior is different. Feldman and Sereda considers that interlayer water is a structural part locating between the layers of C-S-H (Feldman and Sereda, 1968, 1970), which accounts for a high surface area detected by water adsorption experiments. The removal and re-entry of water between these layers is taken as the primary reason for the hysteresis. Inter-layer water gradually loses water at the range of 30% to 10% relative humidity (RH) while further removal takes place at around 10-2% RH, which is accompanied with a rapid loss of modulus and length change. The following empirical equations for correlating RH with saturation condition for interlayer spaces are used.

For the first wetting phase,

$$S_{lr} = h \quad (3.12)$$

For the first drying phase,

$$S_{lr} = h^{0.05} \quad (3.13)$$

The total moisture isotherm for the whole system of cement matrix could be computed by combination of the non-interlayer pores and interlayer pores. For example, the gel pores, interhydrate pores and capillary pores conform to Eq. (3.1) to Eq. (3.11), while for interlayer pores, Eq. (3.12) and Eq. (3.13) will be used.

3.3 The Computation Scheme of the Coupled Model

The flow of the whole multi-scale model could be referred to Figure 3.2. The discussion regarding the stress development in Chapter 2 is computed from the free deformation and elastic modulus. The free deformation and elastic modulus are upscaled from the coupled thermo-hygro-mechanical model. With this scheme, the attempt of scientific understanding at the finer scale (nanometer-scale) is made, while at the larger scale (meter-scale), a more practical computation method is favored for the purpose of engineering application.

3. The Thermo-Hygro-Mechanical Model

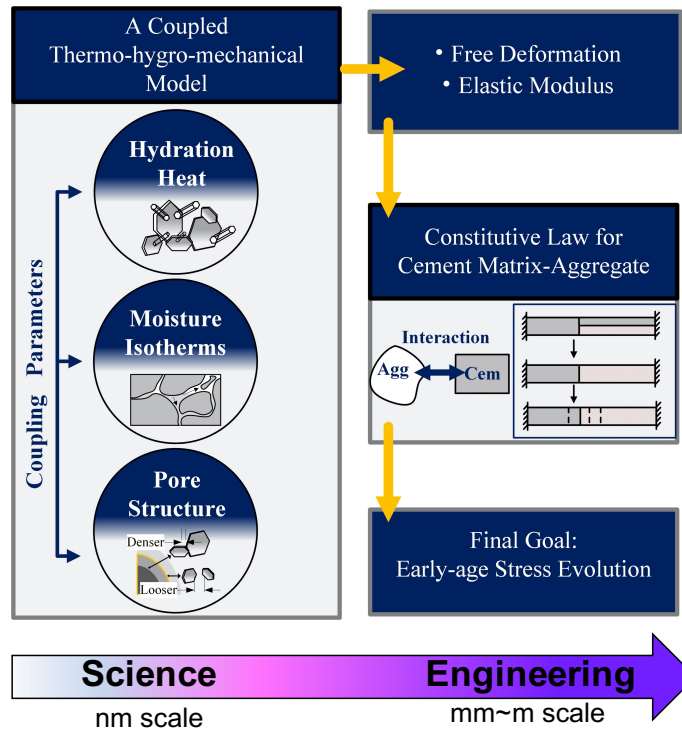


Figure 3.2 Overall flow of the multi-scale model

The most important feature of the coupled thermo-hygro-mechanical model is the mass conservation of the whole system. At early-age, a large amount of free moisture is consumed by chemical reaction to form chemical-bound water. The hydration heat for varied chemical components could be computed by the hydration heat model, which determines the hydration degree and temperature evolution. At certain hydration degree, the mass and volume of varied hydration reactants and products can be computed by the pore structure model. The moisture state within these pores can be derived from the pore structure model and moisture isotherms. Subsequently, by knowing the moisture state within the pore structure at this time step, the free water amount could be computed (which is taken as the water existing in capillary pores in a condensed state). It is noteworthy that the free water amount defined in this study (also in DuCOM) is not equivalent to the definition of evaporable water, since physically absorbed water are not available for hydration. Eventually, the computed free water affects the development of hydration in the next time step, so on and so forth. The nonlinear coupling process of the computation flow is given in Figure 3.3. This is the basic computation frame of this study, which is taken as the most fundamental factors and contributions for early-age properties.

3. The Thermo-Hygro-Mechanical Model

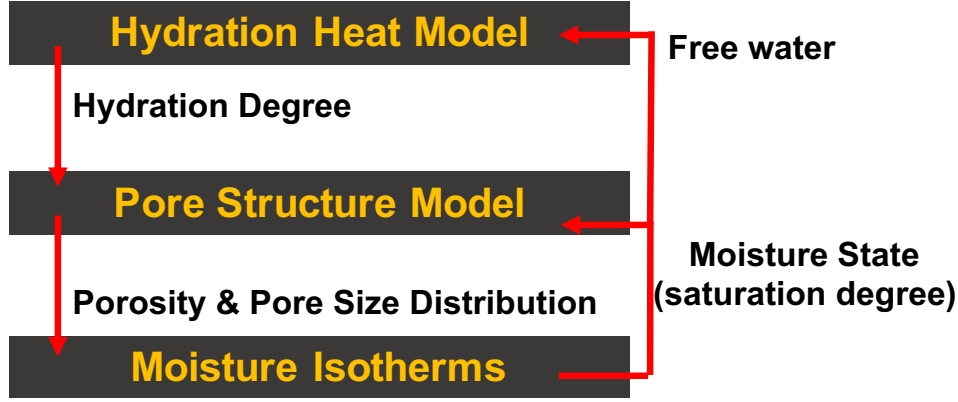


Figure 3.3 The nonlinear coupling of the thermo-hygro-mechanical model

Using this method, the moisture conservation should be satisfied, as shown in the following equation,

$$\rho \left(\sum \phi_i \frac{\partial S_i}{\partial P} \right) \frac{\partial P}{\partial t} - \text{div}(K \nabla P) + \rho \left(\sum S_i \frac{\partial \phi_i}{\partial t} \right) - W_p \frac{\partial \beta}{\partial t} = 0 \quad (3.14)$$

In which, ρ is the density of the water, ϕ the porosity, and P the pressure. W_p the weight of powder material per unit paste volume and β the chemical-bound water per unit weight of hydrated powder. The second term $\text{div}(K \nabla P)$ is the flux term. Under sealed condition, the flux term can be eliminated, Eq.(3.14) can be rearranged as the following:

$$\rho \sum \frac{\partial(\phi_i S_i)}{\partial t} + \frac{\partial(W_{chem})}{\partial t} = 0 \quad (3.15)$$

Where W_{chem} represents the weight of formed chemical bound water. The first term is the potential term and the second term is the sink term. It simply means that the consumption of water from hydration causes the loss of water in pores. Therefore, the chemical potential of the pore solution could be computed at given time step, which in turn affects the hydration at the next time step. When solving this equation, the saturation degree in each group of pore S_i depends on the pore size distribution and the porosity as well.

Since the equation is nonlinear in nature, the exact analytical solution of Eq. (3.15) is difficult to be acquired, especially if the formulation of pore structure distribution is complicated. While in this study, the discrete method is used to solve this equation, which facilitates the computation. Firstly, hydration degree and the consumption of chemical water at certain time step can be computed. Secondly, the porosity ϕ_i and the pore size distribution of each group of pore i at that hydration degree could be computed by the pore structure accordingly. Then, in order to evaluate the moisture state (saturation degree S_i) of each group of pore, Eq. (3.15) should be satisfied. Herein, a bisection search algorithm is implemented for this purpose. A random relative humidity RH_1 is selected as a first value, under such a RH_1 , and given the porosity and pore size distribution, the saturation degree $S_{i,1}$ of each pore can thus be readily computed from moisture isotherms (Section 3.2). Then, such a $S_{i,1}$ is substituted back into Eq. (3.15) to check if the equilibrium is fulfilled. If not, RH_1 is updated by the simple bisection search algorithm as RH_2 .. RH_x , until Eq.

3. The Thermo-Hygro-Mechanical Model

(3.15) is achieved with acceptable accuracy. When the equilibrium state is found, the free water amount can be subsequently determined and used for the next-step input for hydration heat model. This logic is iterated for all time steps to ensure moisture equilibrium is always satisfied. The time-dependent moisture state of pores (or RH in the whole system) due to the hydration itself can be estimated in this manner. But if drying effect is considered, the flux term should be included and computed. In that case, such an easy treatment is not feasible. Finite element method (FEM) will be preferable instead, which is not the analytical objective of the current study (Even though experimental results under drying are presented in this study).

3.3.1 Computation of Autogenous Shrinkage

The computed autogenous shrinkage consists of two parts (Luan and Ishida, 2013), the chemical shrinkage which can be expressed by the following equations:

$$\varepsilon_{ch} = v_{ch} \cdot f(\delta_m) \quad (3.16)$$

Where v_{ch} is the chemical shrinkage, $2\delta_m$ represents the average distance between cement particles. The chemical shrinkage is calculated by the volume change from liquid water to chemical-bound water, given by

$$v_{ch} = W_{ch} \left(\frac{1}{\rho_l} - \frac{1}{\rho_{ch}} \right) \quad (3.17)$$

Where W_{ch} represents the weight of chemical-bound water in a unit volume of concrete. ρ_l and ρ_{ch} represents the density of liquid and chemical bound water, respectively. And ρ_{ch} is used as 1.30 g/cm^3 . $f(\delta_m)$ is expressed by the empirical equation as,

$$f(\delta_m) = 0.045 \cdot \exp(-a \cdot \delta_m^b) \quad (3.18)$$

In which, a and b are constants with values of $1.2 \times 10^{-4.5}$ and 6.3 , respectively. This function has the physical meaning that around 4.5% of the chemical shrinkage is converted to the detected autogenous shrinkage. Another part of the autogenous shrinkage can be calculated by the self-desiccation, which is due to the drop of relative humidity (Lura, Jensen and Van Breugel, 2003):

$$\varepsilon_{LIN} = \frac{P_l \cdot S}{3} \left(\frac{1}{K} - \frac{1}{K_s} \right) \quad (3.19)$$

Where S is the saturation degree (which will be determined by the drop of RH), K is the bulk modulus of the whole porous body (MPa) and K_s is the bulk modulus of solid material, which is used as 44 GP (Lura, 2003).

3.3.2 Computation of Thermal Deformation

The thermal deformation is mainly computed by the time-dependent thermal expansion coefficient (TEC). The TEC of concrete right after casting is very large, since it acts like a liquid phase. Then it will decrease rapidly and stabilized to certain value. The TEC of concrete can be computed by an empirical relationship as (Lin, 2006):

$$\alpha(t) = \alpha_0 - \frac{\alpha_0 - \alpha_h}{1 + \left(\frac{t_{c1}}{t}\right)^{a1}} \quad (3.19)$$

3. The Thermo-Hygro-Mechanical Model

Where α_h is the measured TEC of concrete, which ranges around 8.0-10.0 $\mu\epsilon/^\circ C$. t_{c1} has a value of 14 and $a1$ is 4. α_0 can be defined as the initial TEC of the liquid state of concrete, which can be formulated as the following,

$$\alpha_0 = 60 \times c_{paste} + \alpha_g \times c_g \quad (3.20)$$

Where c_{paste} and c_g are the volume proportion of the cement paste and aggregates.

3.3.3 Modeling of Modulus Development

The prediction of modulus of the cement matrix can be upscaled from the packing density of hydration products (Petersen *et al.*, 2018). The empirical relation which links the packing density of hydration products with the modulus has been formulated by Petersen, et al. It is formed by experimental data from nanoindentation and coarse-grained particle simulations. Eq. (3.21) shows the relationship between packing density and elastic modulus of cement paste,

$$E_m = E_0(\phi - \phi_0)^b \quad (3.21)$$

The $\phi_0 = 0.15$, $E_0=190\text{GPa}$ and b has a value of 3.5. After predicting the modulus of cement matrix, the modulus of the concrete can be calculated by Eq. (2.7) in Chapter 2. Then, the effect of tensile modulus should also be considered by Eq. (2.16).

Using the coupled model, some of the microscopic properties can be upscaled to predict the free deformation and modulus. After substituting the free deformation and modulus development into the constitutive law in **Chapter 2**, the restrained stress can be acquired. In the following section, detailed discussion on how to consider the development of pore structure will be unfolded.

3.4 The Pore Structure Model

In the following discussion, an introduction and review of pore structure of OPC paste will be presented. A simulation-aided study using Mic Model will be firstly conducted. Subsequently, the densification concept used by the Mic Model will be modified and extended to understand the pore structure development. A new pore structure model based on the combined effect between densification and expansion will be established, which attempts to incorporate some of the advanced understanding (e.g., two types of C-S-H and densification process of C-S-H) into the numerical scheme. Then, a new hypothesis on the nanostructure C-S-H is proposed, in order to better categorize varied groups of pores and elucidate the role of them for moisture exchange behavior. The hypothesis is mainly formed on the basis of ^1H -NMR data from published studies.

3.4.1 Introduction and Review of Pore Structure

The pore structure of cement paste has a broad distribution of sizes which range from nano-meter to micro-meter. The multi-scale nature of cement paste has imposed difficulties on the quantitative evaluation of its pore structure, especially if we attempt to bridge all of the disparate pore structure properties measured by different experimental techniques (e.g., Small angle neutron scattering

3. The Thermo-Hygro-Mechanical Model

(SANS), small angle X-ray scattering (SAXS), nuclear magnetic resonance (NMR) and nitrogen adsorption tests) in a consistent manner. It is well known the main hydration product of cement, calcium silicate hydrate (C-S-H), contributes tremendously to this mystery, since C-S-H has a rather complex internal structure, featured by high specific surface area and complex interconnectivity of pores. Microstructure of C-S-H has been deemed to substantially affect the mechanical, transport and deformation properties of cement paste (Vandamme, Ulm and Fonollosa, 2010; Dridi, 2013) and thus, understanding and quantitative modelling of microstructural development of C-S-H is of substantial significance.

Two prestigious schools of microstructure model of C-S-H are Feldman-Sereda Model (Feldman and Sereda, 1968, 1970) and Jennings Model (Hamlin M. Jennings, 2000; Tennis and Jennings, 2000; Jennings, 2008a). The Feldman-Sereda model postulates C-S-H as a layered structure and highlights the effect of interlayer water movement on deformation properties. A relatively large amount of gel pore is considered to locate in the pocket-like structure between C-S-H sheets. It successfully and qualitatively characterizes a variety of shrinkage behaviours and gas sorption properties of cement paste. With regard to Jennings model, the early works resolve an inconspicuous puzzle that the more surface area nitrogen measures in C-S-H structure, the more gel pore volume it misses simultaneously (Hamlin M Jennings, 2000). In order to solve this conundrum, two types of C-S-H structure at meso-scale (1-100 nm), i.e., the low-density C-S-H and high-density C-S-H are postulated. The values of the density of these two types of C-S-H are optimized by predicting experimental data of nitrogen adsorption tests from a variety of studies. The microstructure of C-S-H is proposed to consist of discrete colloidal gel/particles without long-range order. These gel particles (or named as “globules” in (Hamlin M. Jennings, 2000)) are arranged and packed together to form the low-density and high-density C-S-H with different packing densities, respectively. It rationalizes physical properties measured by different techniques including nitrogen adsorption, SANS, SAXS and NMR, and also, explains the chemical aging, shrinkage and creep using gel science (Jennings, 2004; Thomas and Jennings, 2006). These early works of Jennings model are referred to the following discussion as CM-I. Furthermore, Jennings proposed an improved microstructure to quantitatively model the water movement inside the C-S-H structure, in which, globule is viewed as a layered-brick unit with a size of ~5 nm (Jennings *et al.*, 2007; Jennings, 2008a). The later works of Jennings will be denoted by CM-II in the followings. The C-S-H structure at meso-scale (1-100 nm) is hard to model precisely due to its structural complexity and lack of direct experimental techniques to fully unveil its properties at this scale, especially in a quantitative manner. Microscopy techniques can only offer fragmental information that are mostly qualitative and at a scale around several μm . Different techniques (e.g., SAXS, SANS, NMR and nitrogen adsorption tests) offer varied values of specific surface area (SSA). This discrepancy may represent there is a specific detectable scale (or resolution) for each technique to “see” inside the C-S-H, respectively (Hamlin M. Jennings, 2000). However, the hydration of cement is a dynamic process, during which the amount and properties of C-S-H will change as curing age. On one hand, the growth of C-S-H enables its

3. The Thermo-Hygro-Mechanical Model

expansion to occupy the large capillary pores, on the other hand, the pore structure of the C-S-H itself will witness a densification process (or pore refinement). This combined effect of expansion and densification of C-S-H is complicated but very intriguing, which strongly affects the hydration kinetics, pore structure formation and mechanical properties of cement pastes (Ioannidou, Pellenq and Del Gado, 2014; Ioannidou, Kanduč, *et al.*, 2016; Ioannidou, Krakowiak, *et al.*, 2016). The dynamic process of cement hydration has imposed limitations on the experimental techniques to capture the evolution of C-S-H structure. SANS can provide a dynamic measurement of SSA for reacting samples at early age of hydration without drying pre-treatment (Thomas, Jennings and Allen, 1998; Hamlin M. Jennings, 2000), while nitrogen adsorption technique is more appropriate if one attempts to trace the evolution in a long term, e.g., until several months or years. The drying pre-treatment is necessary for nitrogen adsorption technique, and the fragile C-S-H formed at early age will be susceptible to collapse on drying. The drying pre-treatment lead to the failure of using nitrogen adsorption technique to analyse the evolution of pore structure at early age (Thomas, Jennings and Allen, 1998; Jennings, 2004). however, it still provides considerable information for the C-S-H gel at later age (Korpa and Trettin, 2006), and is served as a widely-used and readily available technique for analysing the tendency of changes in pore structure at meso-scale (Garci Juenger and Jennings, 2001).

Based on the experimental results of nitrogen adsorption, CM-I proposes an empirical formula for calculating the fraction of low-density C-S-H and high-density C-S-H at different hydration degrees (Jennings and Tennis, 1994; Tennis and Jennings, 2000), which is able to solve the abovementioned conundrum. It also predicts the SSA and capillary porosity with reasonable accuracy. However, there are still some controversies and problems not addressed explicitly: (1) The empirical formula is hard to be linked with the densification process of C-S-H, which has been experimentally detected by $^1\text{H-NMR}$ (Muller *et al.*, 2013) (2) The increase of SSA with curing age can be explained by the expansion of low-density C-S-H in CM-I. However, as argued by Odler (Odler, 2000, 2003), the decrease of SSA with curing age is also found in some samples. The underneath mechanism cannot be well explained by an empirical formula in CM-I. The numerical model which can consistently explains the development of nitrogen-accessible surface area is still missing. (3) The total porosity accessible to nitrogen cannot be well predicted by the CM-I model (Tennis and Jennings, 2000). As the number of experimental data increases, the fitting error increases significantly. It is necessary to determine and redefine which range of nitrogen-accessible porosity truly reflects the amount of low-density C-S-H. These problems will be addressed in the following discussions. At the very first beginning, a simulation-aided study on the process of densification will be discussed. But due to the limitation of voxel-based method, the finer pores at nanometer-scale cannot be simulated. Therefore a new numerical model is formulated for the densification process in the later stage.

3. The Thermo-Hygro-Mechanical Model

3.4.2 Simulation-aided study using Mic

The original HYMOSTRUC model treated elements of material with fixed properties independent of time (van Breugel, 1995), and further, the updated multi-scale model divides the pore structure into three levels (<5 nm, 5-100nm and >100nm), in which the packing of C-S-H globules are classified into two groups: loosely-packed outer C-S-H and densely-packed inner C-S-H. The DuCOM model used an expanding cluster model to predict the time-dependent bulk density of hydration products. The DuCOM model used an expanding cluster model to predict the time-dependent bulk density of hydration products (Maekawa, Chaube and Kishi, 1999). Whereas, the intrinsic governing mechanism regarding how C-S-H densifies (e.g., how the low-density product and high-density product vary with age, w/c, temperature and drying) is not revealed in these models. The time-dependency of bulk density of C-S-H is rather complicated in reality, which requires a proper understanding and rational description of its densification process. Actually, a realistic densification mechanism should not only be limited to explain the pore structure development, but should also consistently rationalize the hydration kinetics, and the moisture state inside pores. Because all of these processes (hydration kinetics, pore structure development and moisture change) are taking place simultaneously in an interactive and coupled manner. A dynamic densification process of C-S-H has been implemented by S. Bishnoi to rationally model the hydration kinetics of alite particles using the developed platform Mic (or μic (Bishnoi and Scrivener, 2009a)). In this section, the same densification model is utilized to understand the microstructure development of cement (including Alite, Belite, aluminate phase, ferrite phase, gypsum and impurities). The time-dependent bulk density of C-S-H is implemented in the model. The conventional scheme using constant C-S-H density is also conducted for comparison. The effect of w/c on the densification process is analyzed by comparison with published experimental data. Furthermore, the significant implications of the simulation results and the limitation of current voxel-based characterization method are discussed.

3.4.2.1 Simulation Scheme and Outline using Mic

μic is a modelling framework which has been established to simulate complex particle interaction of hydrating cement pastes by S. Bishnoi (Bishnoi, 2008). The hydration kinetics and pore structure can be computed in a system with millions of particles. Its flexible and customizable properties also facilitate the simulation of different physical/chemical mechanisms and their evolution process, serving as an ideal tool for understanding more realistic hydration kinetics and pore structure development during hydration.

- Reactions

The widely-used stoichiometric reactions proposed by Bentz (Bentz, 1997) are adopted and lumped as the following equations for simplicity.



3. The Thermo-Hygro-Mechanical Model

$$1.0V_{OtherPhase} \rightarrow 1.97V_{Crystalline} \quad (3.23)$$

In which V denotes the volume of each phase (C3S, C2S, CSH, CH, crystalline, etc.). H denotes water and subscript “OtherPhase” represents aluminate and aluminoferrite phase. It can be interpreted from Eq. (3.21) to Eq. (3.23) that one volume of reacted cement will produce 2.13 volume of hydration products ($\kappa_h = 2.13$), which corresponds well to the generally-accepted range of value (Sanahuja, Dormieux and Chanvillard, 2007; Ma, 2013). The physical properties of these equations are listed in Table 3.1. Noted that the constant value of C-S-H density is only used in the conventional model scheme, while in the densification model, time-dependent bulk density is expressed by the following Eq.(3.24).

Table 3.1 Density of Reactants and Products (g/cm³) used in the Mic Model

Scheme	Cement	CH	Other Crystallines	CSH
Conventional	3.15	2.24	3.06	2.12
Densification				$\rho_{min} \sim \rho_{max}$

Noted: The adopted values of ρ_{min} and ρ_{max} will be discussed later.

$$\frac{d\rho}{dt} = k_{den} \cdot \frac{\rho_{max} - \rho}{\rho_{max} - \rho_{min}} \quad (3.24)$$

Where, ρ denotes the bulk density of C-S-H. Eq.(3.24) indicate the density will increase from a minimum value ρ_{min} to a maximum value ρ_{max} and its variation rate in time is controlled by a constant parameter k_{den} (g/cm³/h).

Additionally, two nucleation cases of outer C-S-H products are simulated. Case 1 (termed as homogenous case): outer C-S-H nuclei are set to randomly formed in the pore volumes. Case 2 (termed as heterogenous case): very fine outer C-S-H nuclei is only allowed to be formed as attached on the surface of the particles.

3.4.2.2 Modelling Input

- Input Kinetics

In this study, nucleation and growth mechanism (a modified form of Avrami Equation (Bishnoi, 2008)) followed by the diffusion controlled mechanism are set as reaction kinetics.

- Particle Size Distribution in Mic Model

The distribution of particles simulated in this study caters to the actual particle distribution of cement. One advantage of using μic is that millions of particle numbers can be computed which agrees much with the realistic situation and without much computation cost. In this study, millions of cement particles are simulated. The REV size is 100 μm , and voxel size used to post-process the pore size distribution is 0.25 μm . Noted that μic exploits the vector approach that does not depend on the resolution during calculation (i.e., multi-scale information is preserved). Voxels

3. The Thermo-Hygro-Mechanical Model

are only used when post-processing the pore structure information by a pixel-erosion method to facilitate the computation of millions of particles (Bishnoi, 2008; Bishnoi and Scrivener, 2009b).

- Other Modeling Features

Other features like periodic boundary conditions, optimization of the vector approach and customizable reaction conditions can be referred to the literature (Bishnoi, 2008).

3.4.2.3 Simulation Results and Discussion

- Homogenous and heterogenous nucleation

Figure 3.4 and Figure 3.5 denote the pore structure development during hydration for the homogenous and heterogenous case, respectively. Dark blue phase represents inner C-S-H, which is formed inside the original boundary of particles. Light blue particles represent the outer hydration products (Outer CSH, CH and other crystalline products are integrated together and plotted in light blue for better visualization). Black area is the capillary pores.

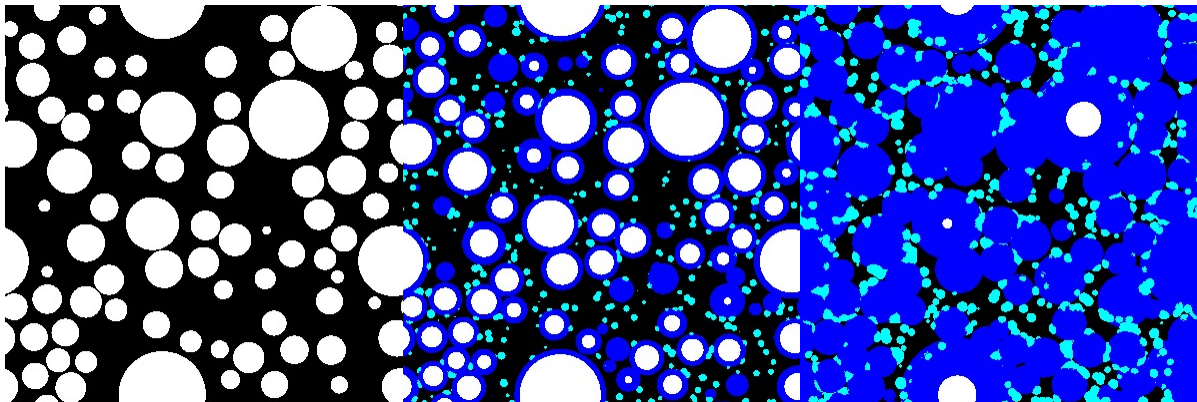


Figure 3.4 Homogenous nucleation of outer products (Hydration Degree:0, 0.72, 0.85)

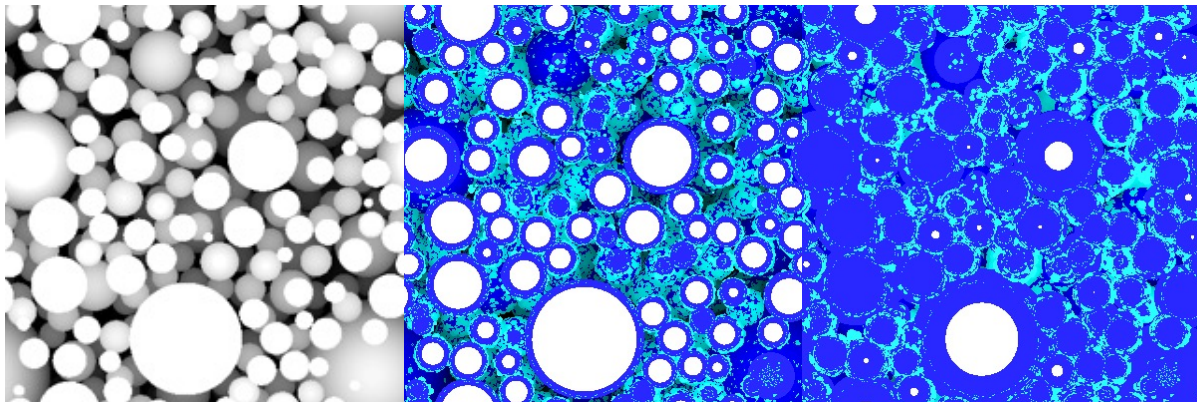


Figure 3.5 Heterogenous nucleation of outer products (Hydration Degree:0, 0.72 and 0.85)

The periodic boundary condition is clearly depicted by aligning figures close to each other, it can be easily seen that the particles on the right boundary of first column of graph actually are the

3. The Thermo-Hygro-Mechanical Model

ones on the left boundary of the second, so on and so forth. It can be found that in the homogenous case, outer C-S-H is randomly formed in the capillary pore space, whereas in the heterogenous case, it is closely confined on the surface of particles.

The BSE (Back-scattered electron) experiment results of hydrating cement paste from Ma (Ma and Li, 2013) are plotted in Figure 3.6 to compare with the modeling results of pore size distribution for the homogenous case. The hydration degree for cement paste with w/c of 0.40 and 0.50 cured for 60 days are 0.72 and 0.79 respectively, determined experimentally by TGA (Ma, 2013). The hydration degree in the simulation is defined as the volume of hydrated cement over that of the original cement. Since the BSE technique eliminates the ink-bottle effect encountered by MIP results, such a comparison is more reasonable instead of using MIP results. As shown in Figure 3.6, simulation scheme using homogenous nucleation will lead to relatively large deviation for total porosity in the range larger than 0.1 μm .

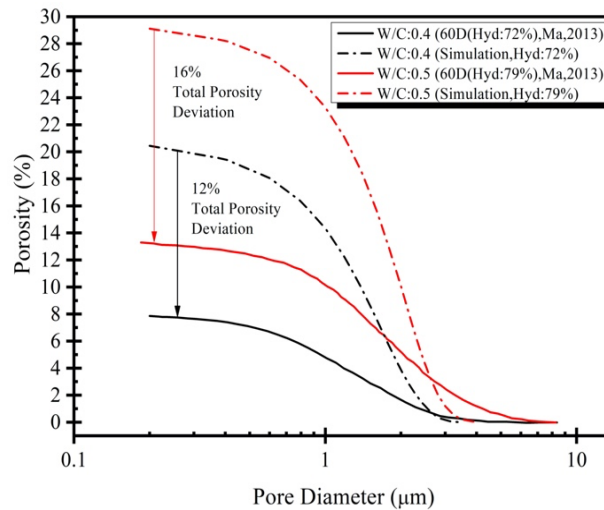


Figure 3.6 Porosity deviation of homogenous case

While the heterogenous case surprisingly leads to much smaller porosity at the same hydration degree, being closer to the experimental results, as shown in Figure 3.7. Noted that in both cases, only the nucleation sites are varied (one is randomly formed in the pore space, the other is formed on the surface of particles), other parameters and reaction conditions are all identical.

A clearer qualitative comparison with both cases under same hydration degree (0.72) can be found from Figure 3.8. Deep image technique is used in the heterogenous case to visualize the confined hydration products on the surface (right figure). It can be seen, the thickness of inner hydration products (the dark blue region) is almost the same for both cases, having around several micrometer. It implies the discrepancy is not due to the inner products.

3. The Thermo-Hygro-Mechanical Model

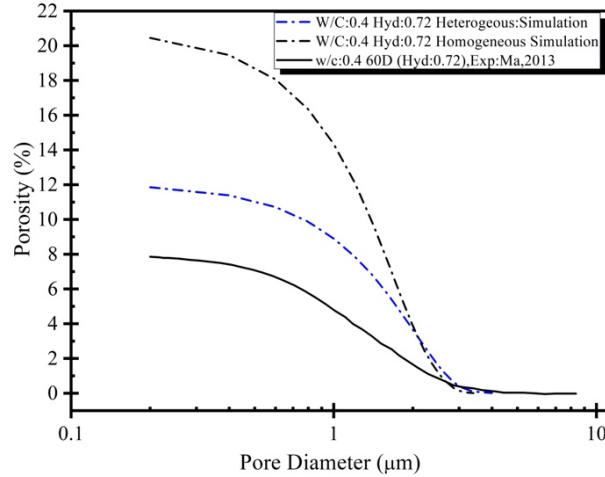


Figure 3.7 Comparison of the heterogenous case with the experiments

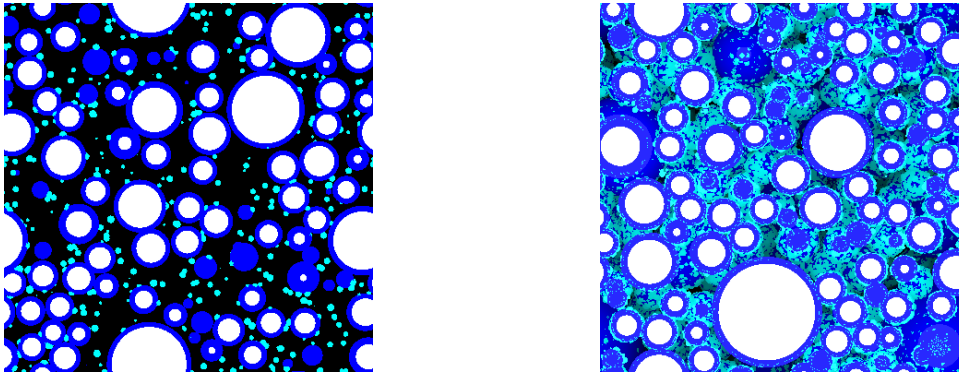


Figure 3.8 A two-dimensional slice of homogenous (left) and heterogenous case (right), with hydration degree=0.72

Quantitative information of the two cases are further plotted in Figure 3.9 to clarify the reason of those discrepancies. Left panel of reveals that each component amount (Cement, CSH, CH and Crystalline) is exactly the same in both cases, signifying the computation is correct. While some discrepancies are found for the pixel number in two cases. As shown in right panel of Figure 3.9, the voxels of hydration products computed in two cases start to differ from each other after hydration degree reaches around 0.25. Those overestimated volume of hydration products in the heterogenous case explain well the smaller total porosity found in Fig. 3.7. It is also interesting to know that hydration degree of around 0.25 also closely matches with the time when impingement between particles take place. Therefore, it can be envisaged that when hydration products (mainly the outer CSH) of particles start to impinge with each other, pixels can be easily captured and counted in the homogenous case. While some very fine and tortuous pores (mostly gel pores smaller than $0.1\ \mu\text{m}$) between hydration products cannot be captured in the heterogenous case due to the pixel-based characterization method for porosity in the model. Pixel size ($0.25\ \mu\text{m}$) is too

3. The Thermo-Hygro-Mechanical Model

large for those fine pores between hydration products. These pores are not “seen” by the pixel-based method.

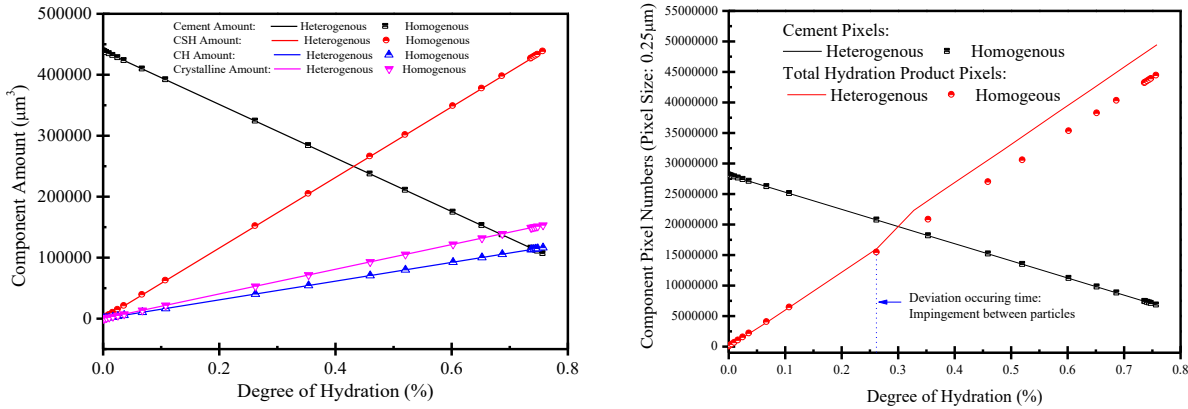


Figure 3.9 Left: Computed amount of chemical component; Right: Pixel numbers of both cases

It demonstrates that the realistic development of hydration products should be more analogous to the heterogeneous case. The results of conventional simulation scheme (both homogeneous and heterogeneous) reveal that a constant stoichiometric density of CSH fails to express the pore structure development, since many fine pores within or between hydration products cannot be treated properly. It highlights the importance of a proper description of bulk density of CSH, which varies with time, w/c, temperature and drying condition. In the next section, a densification model considering the time-dependent bulk density of C-S-H will be discussed.

- The Densification concept in Mic Model

The time-dependent densification process has been successfully used by S. Bishnoi to model the hydration kinetics of alite. The current section aims to figure out how to use this concept to interpret the microstructure development, so that both kinetics and microstructure development can be explained consistently. Herein, a schematic representation is given in Figure 3.10. A densification mechanism is described as follows. At the initial stage, unhydrated core of cement is plotted as the darkest grey color, with the orange-colored boundary. At the earlier stage, inner hydration products are formed, along with loose outer products having very low bulk density (ρ_{min}). It leads to a very rapid volume expansion of outer hydration products at earlier age, which also accounts for the deceleration branch in the hydration kinetics (Bishnoi and Scrivener, 2009a). This loosely-packed structure formed in the early age acts as a skeleton (or “scaffold” structure). Then, in the later age, two simultaneous effects will be taking place. Firstly, more outer C-S-H will be formed inside the skeleton (or “scaffold”), which defines a densification process with increasing density. Secondly, more loosely packed C-S-H structure will be formed at the outer rim, causing the volume expansion and occupying more capillary pores. This volume occupation of capillary pore space by hydration products has been widely studied and accepted. Interestingly,

3. The Thermo-Hygro-Mechanical Model

the densification process (i.e., increasing bulk density of C-S-H as hydration proceeds) has also been recently proved by the advancement of experiment using ^1H NMR (Muller *et al.*, 2013)

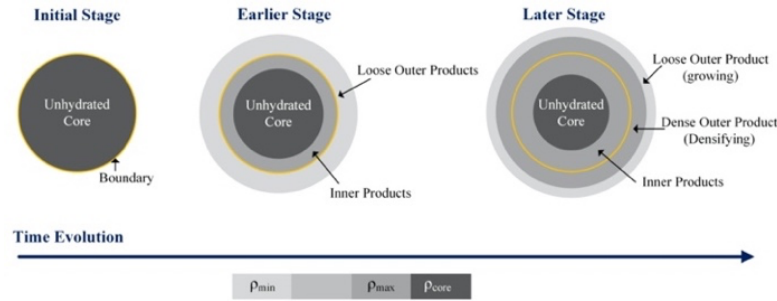


Figure 3.10 Schematic diagram of simulated densification

The bulk density of C-S-H will cease to densify when it reaches a defined maximum value ρ_{max} . By defining the time-dependent bulk density of C-S-H, the undetectable volume of fine pores in conventional scheme (see last section) can be taken into account. It should be pointed out that the definition and clear separation of these two simultaneous effects are hard to be applied in Mic, which needs to define two time-dependent behaviors at the same time, i.e., the densifying outer hydration products and the expanding outer hydration products.

Therefore, in the current model, only one time-dependent bulk density of the whole outer hydration product is considered. The governing equation for this process is given in Eq. (4). Tentatively, in this study we use values given by Bishnoi (Bishnoi and Scrivener, 2009a), $\rho_{max} = 2.0 \text{ g/cm}^3$. and K_{den} is a constant value of $0.007 \text{ g/cm}^3/\text{h}$. Then, ρ_{min} is computed in an iterative way until satisfactory matches with the experimental results are found. After optimizing the model, it is found that when ρ_{min} equals to $\sim 0.65 \text{ g/cm}^3$ (excluding any evaporable water), the modeling results are in good agreement with the experiment results for 60 Days of hydration, as shown in Figure 3.11. The output of model at steps with identical hydration degree as experiments are used for direct comparison. The modeling results demonstrate the feasibility and applicability of adopting such a densification concept to describe the microstructure development of cement.

Additionally, different water-to-cement ratios ($w/c=0.3, 0.4$ and 0.5) are also modeled to elucidate the effect. The same computation methodology as aforementioned is utilized. The computation results are shown in Figure 3.11. Results for all w/c cases are consistent with the experimental results. The optimized values for ρ_{min} are 0.82 g/cm^3 , 0.65 g/cm^3 and 0.57 g/cm^3 for w/c equal to $0.3, 0.4$ and 0.5 , respectively. That is to say, at lower w/c ratio, a higher initial bulk density ρ_{min} is found.

3. The Thermo-Hygro-Mechanical Model

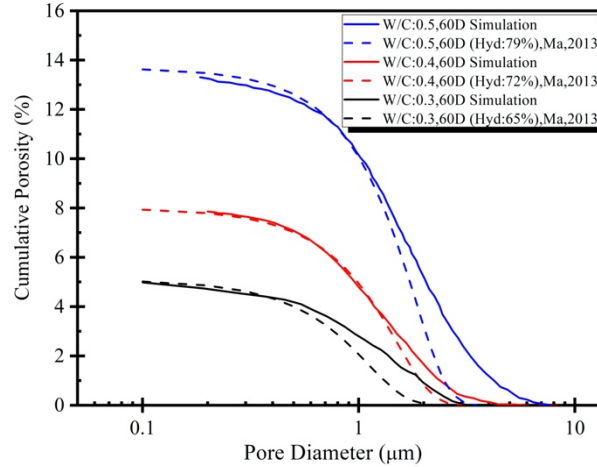


Figure 3.11 Computed pore size distribution with varied w/c using densification model (Age=60 days)

Importantly, the simulation results indicate the densification process is not only age-dependent, but also greatly relies on w/c. Varied w/c will lead to different densification effect. If we view it from another perspective by keeping the initial bulk density values ρ_{min} the same in three w/c cases and attempt to search the densification rate k_{den} for all three w/c cases, one can readily conclude that a lower w/c requires much higher densification rate. It is noteworthy that this mechanism corresponds well to the concept of two types of C-S-H proposed by Jennings (Hamlin M. Jennings, 2000; Jennings, 2008a). which states that under a low w/c situation, the ratio of HD CSH (high-density) C-S-H to LD (low-density) CSH is higher than that in high w/c situation. Recent studies (Šmilauer and Bittnar, 2006) on micromechanics analysis also supports that HD C-S-H tends to be formed in restricted space and LD C-S-H in more open space.

Noted that the density ρ_{min} described here represents the bulk density excluding any evaporable water present in pores. After converting to saturated bulk densities, they will be $\sim 1.53 \text{ g/cm}^3$, 1.42 g/cm^3 and 1.37 g/cm^3 for w/c equal to 0.3, 0.4 and 0.5 respectively. These values are smaller than the value of saturated low-density C-S-H in Jennings' model (Hamlin M. Jennings, 2000), i.e., $\sim 1.93 \text{ g/cm}^3$ (converted from d-dried density to saturated density). But it is reasonable that at very early age, more loosely-packed C-S-H than relatively mature C-S-H can be formed, e.g., as evidenced by studies using TEM image for OPC cement paste cured for 12 hours (Mathur, 2007).

- Limitation of pixel-based method

It is difficult for pixel-based method to characterize the multi-scale properties of pore structure, which spans over several orders of size (from nm to μm scale). Even though the size of a pixel is chosen as $0.1 \mu\text{m}$, most of the fine gel pores having nano-meter size cannot be considered using conventional computation method. One solution is that using high-resolution numerical model that simulates nanoparticles in nm-scale (or even starting from molecular level) to predict the thermal-hygro-mechanical behavior of the material in a full-scale (from nm up to μm). But,

3. The Thermo-Hygro-Mechanical Model

obviously, such a model is of very high computation cost and not available up to now. An alternative is to interpret the material properties using multi-scale model. Cementitious materials possess heterogeneities at different scales. In a multi-scale approach, the heterogeneous nature in a smaller scale is upscaled as a homogenized response in a larger scale. And thus, varied behaviors in different scales can be bridged and predicted. The key point of multi-scale approach is to obtain accurate and rational constitutive responses when upscaling, which can truly express the behavior of the materials. In this study, the densification concept is a way to homogenize the nano-scale porosity within C-S-H as a time-dependent bulk density, so that its development and pore size distribution in micrometer scale can be simulated properly.

- Implications and perspectives

Due to the complexity of the densification process, which is related to age (or time), w/c, temperature and drying conditions, etc., it is of great importance to conduct further study to elucidate its mechanism. A mathematical model (or constitutive law) to express this process should be formulated properly, so that a multi-scale approach can be implemented. In this way, it can consistently explain experimental results in varied scale (MIP, Nitrogen adsorption, SANS and NMR, etc).

The advancement of understanding on C-S-H requires the aid of all aforementioned experimental techniques and also, more importantly, it requires a proper interpretation of these experimental results. For example, when nitrogen adsorptions tests are conducted on cement paste specimen with same w/c=0.5, varied interpretations can lead to contrasted conclusions (Ma and Li, 2013; Zeng *et al.*, 2016). which hinders the proper use of these experimental data into the model. Experimental results from Ma (Ma and Li, 2013) is plotted in left panel of Figure 3.12. It was concluded in his study that porosity from 3 nm to 100 nm detected by nitrogen adsorption tests is decreasing as curing time increases, and such pores are categorized into small capillary pores. The porosity of these capillary pores is decreasing due to the volume occupation of more hydration products. Whereas in Zeng's study (right panel of Figure 3.12), it can be found that the porosity of pores smaller than 4 nm increases as hydration time proceeds, while pores in the range >4 nm demonstrates an unclear trend against hydration time. Such discrepancies between researches imply that a more comprehensive and deeper understanding on densification process is required, which provides insight on a more rational classification of varied types of pores and their evolution patterns. It also serves as fundamental and key problems for shrinkage-related problems, because the moisture state and transport properties greatly associate with pore morphologies.

3. The Thermo-Hygro-Mechanical Model

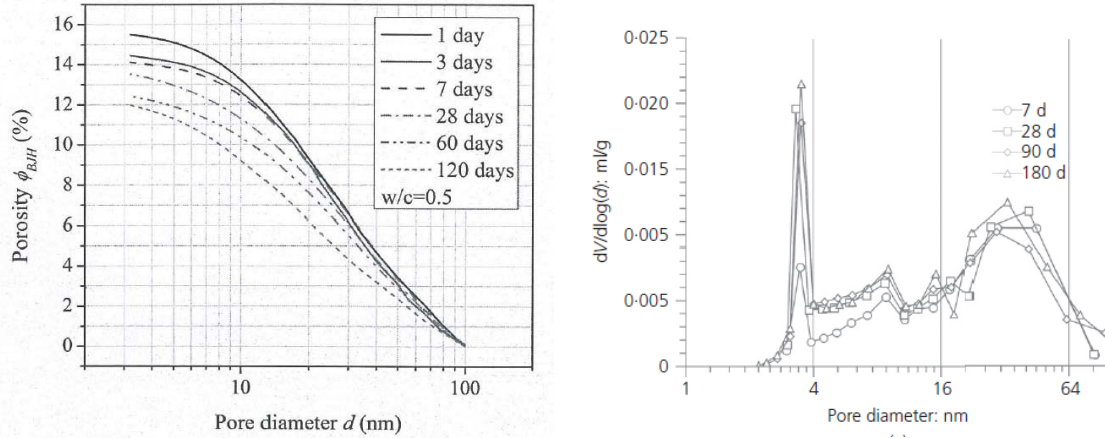


Figure 3.12 Left: Porosity of cement paste (w/c:0.5) tested by NAD, after (Ma and Li, 2013). Right: Derivative plot (w/c:0.5) tested by NAD, after (Zeng *et al.*, 2016).

In order to overcome the disadvantage of pixel-based method on characterization on the pore structure, a new mathematical formulation to consider the combined effect between densification and volume expansion is proposed, which is able to quantify the porosity at finer scale (meso-scale). The inconsistency of varied interpretations on the results of nitrogen adsorption test are also resolved by a proposed densification mechanism, which is supported by systematic experiments using nitrogen-adsorption test.

3.4.3 The proposed pore structure model based on combined effect

This section presents a numerical model to investigate the combined effect of expansion and densification of meso-scale C-S-H in cement paste. The time-dependent development of pore structure, densification mechanism in both low and high water-to-cement ratio, are discussed. The model is validated through nitrogen adsorption experiments of our study and a variety of research in different organizations. Even though the scattering of experimental data from different studies is inevitable, it is assumed that the evolution trend of C-S-H with time should be consistent. The logic and attempt adopted here is to rationalize disparate measurements, resolve controversies among varied studies, and consistently bridge the early- and later-age properties. In this section, development of amount, densities and porosities of two types of C-S-H is mainly unfolded, without making postulations upon a finer scale (i.e., the morphology and internal structure of C-S-H). It means that the numerical results do not contradict with the aforementioned Feldman-Sereda Model or Jennings Model (CM-I and CM-II) at a finer scale. Also, it is noteworthy that the hydration of cement is always a coupled thermo-hydro-mechanical-chemical process. The hydration kinetics and pore structure development will evolve simultaneously, and different chemical-physical processes are not separated or independent. In order to establish a more realistic computation scheme, the coupling effects and correlations between these processes should be well considered and incorporated. The implications of the proposed microstructure model and its correlations with hydration kinetics and development of mechanical strength will be discussed. Furthermore, the range of nitrogen-accessible pores that might truly reflect the growth of low-

3. The Thermo-Hygro-Mechanical Model

density C-S-H is redefined, based on our finding that the porosity with diameter of 1 to ~8 nm scales linearly with the increase of measured surface area.

3.4.3.1 CM-I: Jennings' numerical model for two types of C-S-H

Jennings Model (CM-I) proposes a set of equations for computation of amount of each compound and hydration product. The mass of each compound and hydration product at a given hydration degree can be readily determined by reaction equations of cement hydration and the physical properties of them. The stoichiometry reactions used in the CM-I are given in Equations (3.25) to (3.30). The density, molecular weight, and molar volume of compounds and hydrates that are utilized is shown in Table 3.2 Properties of compounds and hydrates.

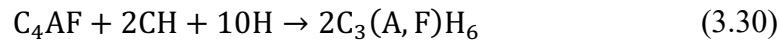
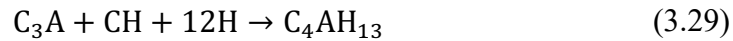
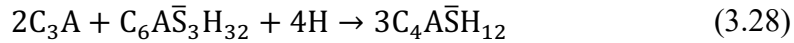
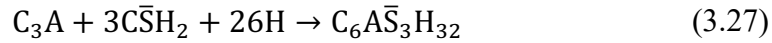
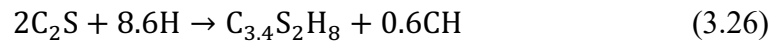
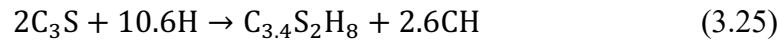


Table 3.2 Properties of compounds and hydrates

Compounds/Hydrates	Nominal formula	Density (kg/m ³)	Molecular weight (kg/mol)	Molar volume (cm ³ /mol)
Alite	C ₃ S	3150	0.228	72.4
Belite	C ₂ S	3280	0.172	52.4
Aluminate	C ₃ A	3030	0.270	89.2
Ferrite	C ₄ AF	3730	0.486	130.3
Water	H ₂ O	998	0.018	18.0
Gypsum	C \bar{S} H ₂	2320	0.172	74.1
Calcium hydroxide	CH	2240	0.074	33.1
Hydrogarnet	C ₃ (A, F)H ₆	2670	0.407	152.7
AFm, saturated	C ₄ A \bar{S} H ₁₂	1990	0.623	346
AFm, dried	C ₄ A \bar{S} H ₈	2400	0.551	229
AFt, saturated	C ₆ A \bar{S}_3 H ₃₂	1750	1.255	717
AFt, dried	C ₆ A \bar{S}_3 H ₇	2380	0.805	338
Calcium aluminate Hydrate	C ₄ AH ₁₃	2050	0.560	274
LD C-S-H*,dried	C _{3.4} S ₂ H ₃	1440	0.365	252
HD C-S-H*,dried	C _{3.4} S ₂ H ₃	1750	0.365	211

3. The Thermo-Hygro-Mechanical Model

The main focus of the computation is the derivation of C-S-H. After the total mass of C-S-H at a given hydration degree is obtained, the mass ratio of Low-density C-S-H (LD C-S-H) and High-density C-S-H (HD C-S-H) can be obtained by Eq. (1). This empirical equation is obtained using multiple linear regression on the experimental data (Hunt, 1966).

$$M_r = 3.107 \times (w/c) \times \alpha - 1.347 \times \alpha + 0.538 \quad (3.31)$$

Where w/c is the water-to-cement ratio, α the hydration degree and M_r the ratio of the mass of LD C-S-H to the total mass of C-S-H. Please note that in CM-I, the classification of low- and high-density C-S-H is distinguished by the accessibility of nitrogen. Nitrogen can only access part of the pores in LD C-S-H, while it can not measure pores in HD C-S-H. Correspondingly, the volume of HD and LD C-S-H can be determined through Eq. (3.32) and Eq. (3.33), respectively.

$$V_{HD} = \frac{M_t - (M_r M_t)}{\rho_{HD}} \quad (3.32)$$

Where ρ_{HD} denotes the density of HD C-S-H and M_t the total mass of C-S-H.

$$V_{LD} = \frac{M_r M_t}{\rho_{LD}} \quad (3.33)$$

Where ρ_{LD} is the density of LD C-S-H. The quantity of other phases can be computed at any hydration degree, given the cement composition and water-to-cement ratio. In order to achieve the equilibrium of volume, the volume of capillary pores should satisfy Eq. (3.34):

$$V_{cp}(\alpha) = V_{paste} - \sum_i V_r(\alpha) - \sum_i V_p(\alpha) \quad (3.34)$$

Where V_{cp} , V_{paste} , V_r , V_p represents the volume of capillary pore, cement paste, reactant and hydration products respectively. As the mass of the d-dried paste and C-S-H is known, the predicted nitrogen-accessible surface area for d-dried paste could be determined by Eq. (3.35):

$$S_{N_2} = \frac{M_r M_t S_{LD}}{M_D} \quad (3.35)$$

Where S_{N_2} is the specific surface area of dried paste, S_{LD} is the surface area per gram of d-dried LD C-S-H, which is a constant determined by model fitting. In CM-I, $S_{LD} = 247 m^2/g$ is used. M_D is the mass of d-dried paste. It can be calculated using the dried density of hydration products in Table A.1 or an estimation equation in CM-I (Jennings and Tennis, 1994), which yields no much differences on the results.

3.4.3.2 The proposed formulation and computation scheme

The formation of C-S-H during hydration is a complex and dynamic process. On one hand, C-S-H will grow and expand to occupy the large capillary pores, also resulting in the increase of mesopores that are located inside the C-S-H products. On the other hand, the pore structure of the formed C-S-H itself will witness a densification process, i.e., the refinement of mesopores will take place simultaneously. The microstructure development of cement paste is governed by the combined action between expansion and densification of C-S-H. To model this combined effect,

3. The Thermo-Hygro-Mechanical Model

it is hard to start from the volume of C-S-H, since it involves the unknown porosity within C-S-H gel. However, from another perspective, the mass of formed C-S-H at a given hydration degree is mainly determined by the stoichiometry reactions, which can serve as the first step. Subsequently, to consider the respective effect of expansion and densification, the mass of formed C-S-H at each time step could be considered to consist of two parts: one belongs to expansion and the other belongs to densification, as given in Eq. (3.36)

$$\Delta m_{csh}^i = \underbrace{\sum_{j=0}^{i-1} v_{csh}^j \Delta \rho_{csh}^j}_{\text{Densification Term}} + \underbrace{v_{csh}^i \cdot \rho_{ini}}_{\text{Expansion Term}} \quad (3.36)$$

Where Δm_{csh}^i denotes the mass increment of total C-S-H at time step i . v_{csh}^i , v_{csh}^j is the volume of formed C-S-H at time step i and j , respectively. $\Delta \rho_{csh}^j$ is the density increment of C-S-H at time step j . ρ_{ini} is the initial density of newly formed C-S-H. Herein, the C-S-H is discretized into different layer at different specific time steps. Based on the mass equilibrium, the total mass formed at a given time step i should equal to the sum of the mass for densification of all previously-formed layers earlier than time step i , and the mass for expansion of newly-formed C-S-H layer. A schematic representation of this process is shown in Figure 3.13. In this manner, the combined effect between volume expansion (the formation hydration products will keep occupying more capillary pore space) and the densification (the previously-formed products will be further densified) can be considered. The low-density product could be further densified to be denser product while reversed transformation is not permitted.

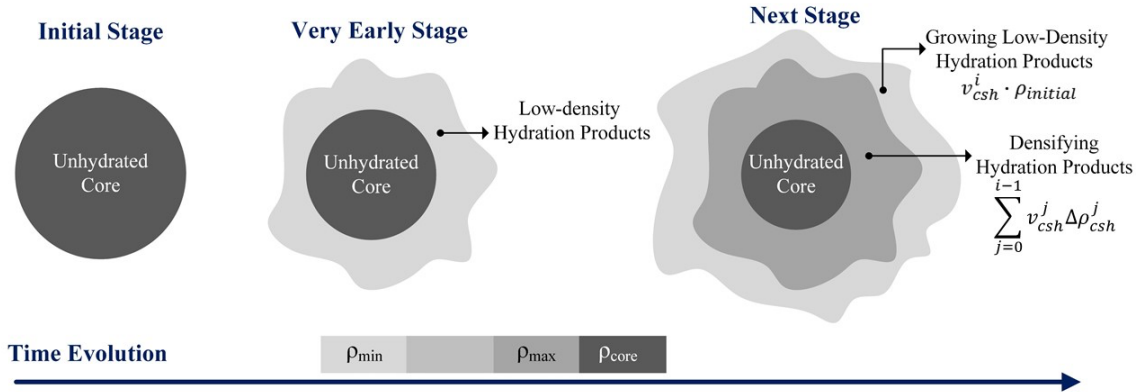


Figure 3.13 Schematic representation of combined effect between densification and expansion

If the time-dependent bulk density of C-S-H is found, the volume of C-S-H formed at discrete time steps can be computed accordingly. The next step is to find out the time-dependent bulk density of C-S-H, which can be regarded as a function of hydration degree, as depicted by Eq. (3.37):

$$\rho_{csh}^i = \rho_{csh}^i(\alpha) \quad (3.37)$$

The function for time-dependent bulk density can be treated as a function of minimum density, maximum density and a densification rate, which has been used to successfully model the

3. The Thermo-Hygro-Mechanical Model

hydration kinetics of alite by S. Bishnoi. A minor modification is made to replace the variable time by the hydration degree, for convenience of computation, as given in Eq. (3.38):

$$\frac{d\rho}{d\alpha} = k_{den} \cdot \frac{\rho_{max} - \rho}{\rho_{max} - \rho_{min}} \quad (3.38)$$

Where ρ represents the density of C-S-H at hydration degree α , ρ_{min} is a constant of the minimum possible bulk density of C-S-H, ρ_{max} is a constant of the maximum possible bulk density. k_{den} denotes the densification rate of density of C-S-H. After rearranging Eq. (3.38) and integrating with hydration degree from 0 to α , it yields Eq. (3.39):

$$\rho(\alpha) = \rho_{max} - (\rho_{max} - \rho_{min}) \cdot \exp\left(\frac{-k_{den}\alpha}{\rho_{max} - \rho_{min}}\right) \quad (3.39)$$

Herein, the densification rate k_{den} is further defined as a time-dependent function $k_{den}(\alpha)$, which gives Eq. (3.40):

$$\rho(\alpha) = \rho_{max} - (\rho_{max} - \rho_{min}) \cdot \exp\left[\frac{-k_{den}(\alpha) \cdot \alpha}{\rho_{max} - \rho_{min}}\right] \quad (3.40)$$

Which represents the density evolution of any newly formed layer of C-S-H, increasing from ρ_{min} to certain value bounded by ρ_{max} . The density increment at each time step is controlled by the function $k_{den}(\alpha)$, which needs to be found out in the next stage.

In CM-I, the mass ratio between LD and HD C-S-H is expressed by the empirical formula, as shown in (Eq. 3.31). In this study, the idea is to find out the proper densification rate k_{den} at each time step to make the computed mass ratio between LD and HD C-S-H match with the CM-I. In other words, the key problem to be addressed is that, how densification develops such that the computed amount of LD C-S-H, meso-porosity and capillary porosity all agree with the measured values.

To compute the k_{den} , values of parameters in Eq.(3.40) should be set first. In CM-I (Tennis and Jennings, 2000), the d-dried density of LD C-S-H is 1.44 g/cm³, the d-dried density of HD C-S-H is 1.75 g/cm³. In this study, since the bulk density of each layer of C-S-H is considered to change with time, we consider there are two groups (or clusters) of C-S-H: those C-S-H layers with a density lower than 1.60 g/cm³ belong to LD C-S-H and those above 1.60 g/cm³ belong to HD C-S-H. The assumed value 1.60 g/cm³ is the average of 1.44 g/cm³ and 1.75 g/cm³. The minimum density ρ_{min} and maximum density ρ_{max} is set as 1.30 g/cm³ and 2.10 g/cm³, respectively. It is noteworthy that after converting d-dried density of HD C-S-H (1.75 g/cm³) into the saturated density, it agrees well with the maximum saturated bulk density of C-S-H, around 2.10 g/cm³ found by ¹H-NMR (Muller *et al.*, 2013). These values can be updated and replaced by more accurate values in the future, if found. But it does not affect the overall computation scheme and evolution trend.

After substituting the input parameter, the k_{den} is computed and data points are shown in black in Figure 3.14. A fitting curve is formed by nonlinear regression analysis for more convenient use. The equation for this curve is given in Eq. (3.41).

3. The Thermo-Hygro-Mechanical Model

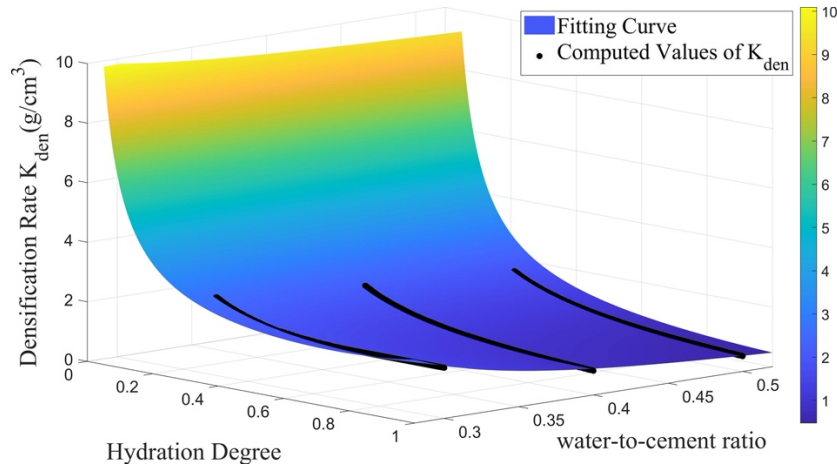


Figure 3.14 Fitting curve and computed densification rate with varied w/c and hydration degree

$$k_{den}(\alpha, w/c) = \frac{(w/c)^{-3.686}}{-129.9 \times \alpha + 202.7} + \alpha^{-0.7654} - 1.303 \times (w/c) \quad (3.41)$$

Where k_{den} is the densification rate (g/cm³ per unit of hydration degree). All coefficients in Eq. (3.41) are statistically at the 95% confidence level. The R^2 is equal to 0.9972.

Because CM-I is formulated by experimental data with hydration degree larger than 0.3, only these data are used to the fitting. For the densification rate at hydration degree lower than 0.3, values are predicted by the curve. The result reveals that there is an exponential decrease at the predicted region, implying a significant change in properties at the very early stage. After performing such a reversed analysis to formulate the function $k_{den}(\alpha, w/c)$, the densification rate in the whole domain can be readily found from Eq. (3.41). The flow chart of the model is shown in Fig. 3. The volume and mass of the whole system is kept in equilibrium at each time step. Currently, we only consider the time-dependent properties of C-S-H while assuming the physical properties of other hydration products is constant with time.

3. The Thermo-Hygro-Mechanical Model

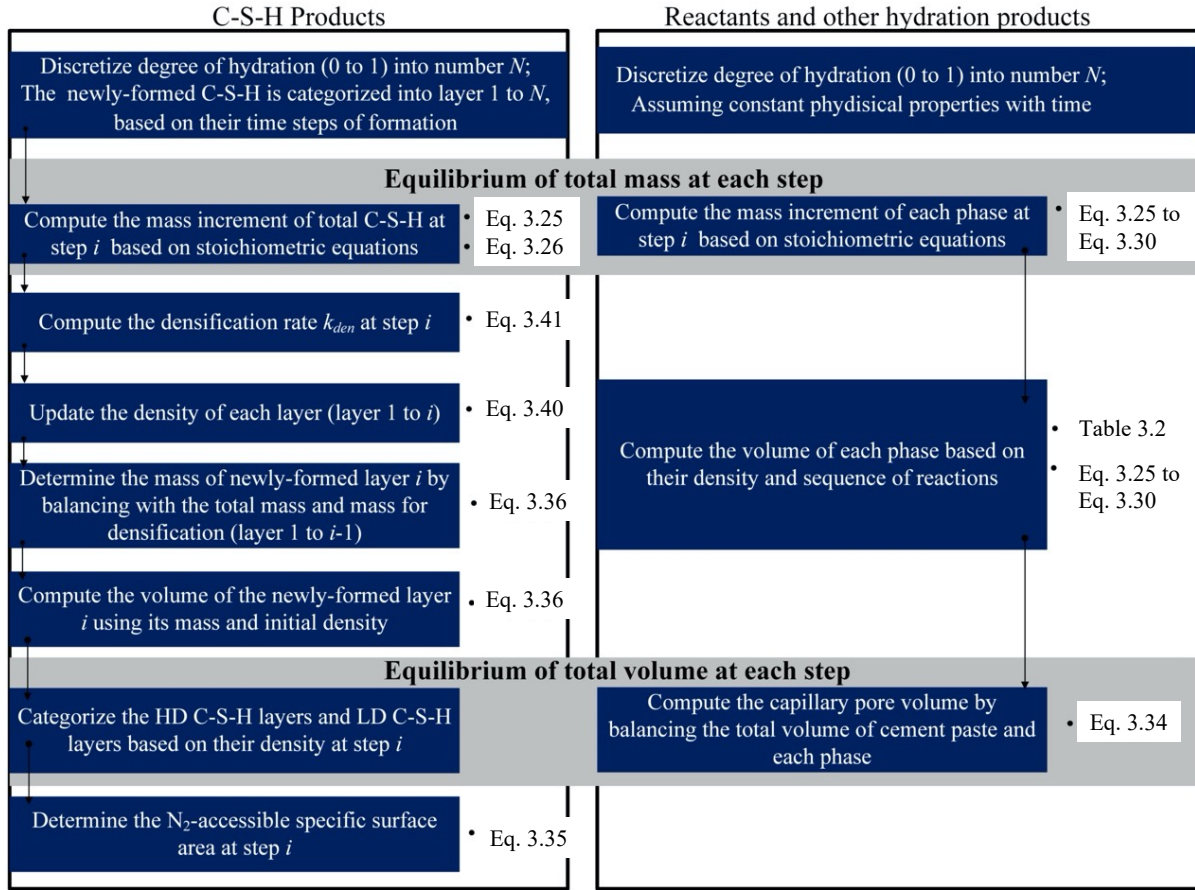


Figure 3.15 Flow chart of the computation of the pore structure development

3.4.3.3 Mass ratio of LD CSH and HD C-S-H

The computed densification rate in Figure 3.14 indicates the densification rate is relatively higher with smaller water-to-cement ratio. Rather high values in the very early age (hydration degree smaller than 0.3) is also found, compared to the later age. Such a densification rate indicates the strong tendency for C-S-H to densify at the very early age. However, the effect of volume expansion is also very significant, due to the low initial density. With a given mass increment, the low density of C-S-H layers enables rapid volume expansion into the capillary pore space. The dominant role of LD C-S-H expansion at this period can be found from Figure 3.16. The earlier age is shaded as darker grey colour in the figures. The mass ratio computed from the current model and CM-I are shown in the red and blue line, respectively. The dominant role of LD CSH at the very early age signifies that the formation of LD C-S-H is formed rapidly and occupies a large portion of capillary pores. The impingement of hydration products between particles may occur earlier and corresponds to the peak of hydration kinetics, which is in agreement with the statement from Bishnoi (Bishnoi and Scrivener, 2009a). Mathur (Mathur, 2007) found out the formation of very loosely-packed hydration products formed at the outer boundary of the hydration products at 12 hours of hydration using TEM, as shown in Figure 3.17. When hydration degree is larger

3. The Thermo-Hygro-Mechanical Model

than ~ 0.3 , the mass ratio between LD and HD CSH largely depends on the w/c ratio. The mass ratio of LD CSH/ total CSH corresponds well to Jennings model, since the parameter is optimized through Jennings Model. To further confirm this evolution pattern at later age, systematic experiments using nitrogen-adsorption tests are conducted.

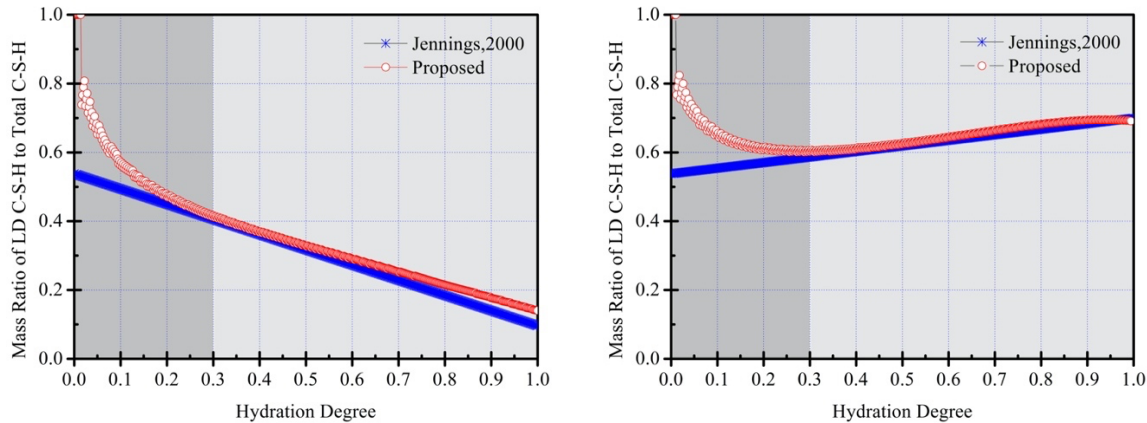


Figure 3.16 Computed Mass ratio of LD and HD CSH in the proposed model (Left: w/c:0.30; Right: w/c: 0.50)

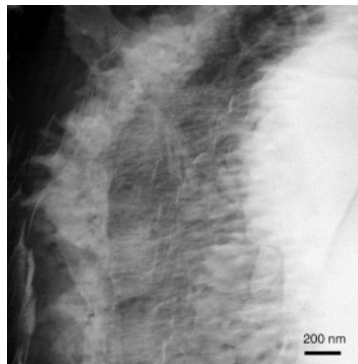


Figure 3.17 Loosely-packed CSH found by TEM image (After (Mathur, 2007))

3.4.3.4 Nitrogen adsorption tests

In this study, cement paste with two w/c ratios (w/c:0.5 and w/c 0.3), varied curing age and temperature condition is studied. The specimen is casted inside plastic containers, sealed with double layers of gum tape to achieve a sealed condition. The cement used for this experiment is the OPC cement from Sumitomo Osaka Cement Co., Ltd. After being cured at various temperatures for certain age (from 1 day up to 120 day), only the center part of the specimen will be extracted for testing to minimize the effect of bleeding.

Since drying has exerted important effects on the results, varied drying conditions are also considered. The first drying method is the d-drying, which has been widely used by many researches and considered as a common way to preserve the damage of pore structure of

3. The Thermo-Hygro-Mechanical Model

cementitious materials during drying (Korpa and Trettin, 2006). The specimen was crushed into small pieces (mm size) and kept in a freeze-drying desiccator with a pressure of 10 Pa for one day before testing. After drying, the specimen were crushed into powders and tested immediately. The second drying method is using solvent-exchange method. Specimen (mm size) was immersed into isopropanol solution to stop the hydration at certain curing age. After that, the small pieces were ground into powder. Then, powder samples were degassed under vacuum pressure of 0.2 mbar at 40 °C for one day before testing. The second drying method is more mild than the first one. The considered experimental factors are listed in Table 3.3. The hydration degree of the samples are determined by loss on ignition test. The powder samples smaller than 600 μm are used.

Table 3.3 Experimental factors

w/c	Curing Temperature (°C)	Drying Methods
0.30	22	Solvent Exchange and D-drying
	40	
	65	
0.50	22	
	40	
	65	

3.4.3.5 Densification Mechanism under normal temperature (22 °C)

Jennings (Hamlin M. Jennings, 2000; Tennis and Jennings, 2000) postulates that there will be two types of C-S-H, the low-density C-S-H (LD C-S-H) and the high-density C-S-H (HD C-S-H). It was considered that nitrogen can only penetrate and measure the specific surface area of the LD C-S-H, while it cannot access the HD C-S-H. It was considered that LD C-S-H was formed at the shorter hydration time while HD C-S-H is produced preferentially at the later time. Odler pointed out that, with such a postulate, the measured nitrogen-accessible specific area will witness an increase (even though with a slower rate at later age) or at least stay unchanged (Odler, 2000). Furthermore, he argued that the decline of nitrogen accessible surface area was found for both C_3S and cement past samples with the increase of hydration time, which seemingly to be against Jennings' hypothesis.

Interestingly, after summarizing the experimental data from a variety of data, it was found out that the pronounced decline of surface area with curing age existed only in low w/c or high temperature case (Odler, Hagymassy, Yudenfreund, Kaissar M Hanna, *et al.*, 1972; Odler, Hagymassy, Yudenfreund, Kaissar M. Hanna, *et al.*, 1972; Skalny and Odler, 1972). Such a phenomena has been validated through our experimental studies. Table 3.4 shows the experimental data in this study for normal room temperature (22 °C). In the high w/c case, the surface area constantly increases as hydration time elapses. Both drying methods (solvent-exchange method and d-drying method) reveal the same evolution pattern. At the early-age the

3. The Thermo-Hygro-Mechanical Model

increase of surface area is relatively faster while later age it tends to slow down. This evolution pattern for high w/c cement paste agrees under normal temperature agrees with other researches (Thomas, Jennings and Allen, 1998; Zeng *et al.*, 2016). Regarding the low w/c ratio case, the decrease of surface area at certain age is also found by both drying method, which agrees with a series of experimental findings from Odler and Zeng.

Table 3.4 Nitrogen-accessible surface area for varied w/c and drying condition cured at 22 °C

Conditions	W/C: 0.5		W/C=0.3	
Drying Method	Hydration Degree (Curing Age)	Surface Area (m ² /g dried paste)	Hydration Degree (Curing Age)	Surface Area (m ² /g dried paste)
D-drying	0.38 (1D)	16.73	0.35 (1D)	17.83
	0.76 (28D)	23.82	0.51 (3D)	18.61
	0.81 (90D)	30.81	0.52 (7D)	18.52
	0.85 (120D)	35.59	0.67 (120D)	9.16
Solvent-exchange (Isopropanol)	0.38 (1D)	28.07	0.35 (1D)	15.41
	0.57 (3D)	42.40	0.51 (3D)	36.96
	0.71 (7D)	86.40	0.52 (7D)	53.90
	0.85 (120D)	94.95	0.59 (28D)	44.47

Even though the prediction of exact values will be hard due to the fluctuation of experimental data between varied studies, a more realistic model should be capable of rationalizing the evolution patterns found from varied studies. The proposed pore structure model in this study can offer us new insights on the densification mechanism which consistently explains evolution patterns for both low and high w/c ratio case. Figure 3.18 shows the computed amount of C-S-H under varied w/c ratios. The amount of two types of C-S-H changes with time which determines the occupied capillary pore space. And also, since only LD C-S-H is accessible to nitrogen, the amount of LD C-S-H also determines the detected surface area.

Under a low w/c ratio case, the distance between cement particles is shorter, and the densification rate (K_{den}) is relatively high. HD C-S-H is more likely to be formed in this more restricted space, the amount of HD C-S-H is in a dominant role. It could also be found that, at the later age, a certain amount of LD C-S-H is densified into HD C-S-H due to the high K_{den} , which well explains the decrease of nitrogen-accessible surface area found by experiments. Under a high w/c ratio case, the distance between particles is longer, and the K_{den} is lower. The dominant role of LD C-

3. The Thermo-Hygro-Mechanical Model

S-H takes place for the whole period, even though a certain part of LD C-S-H constantly densifies into HD CSH, the preferable formation of new LD CSH results in the increase of surface area as hydration time. The proposed densification mechanism resolves the controversies (Hamlin M. Jennings, 2000; Odler, 2000) on the development pattern of nitrogen-accessible surface area .

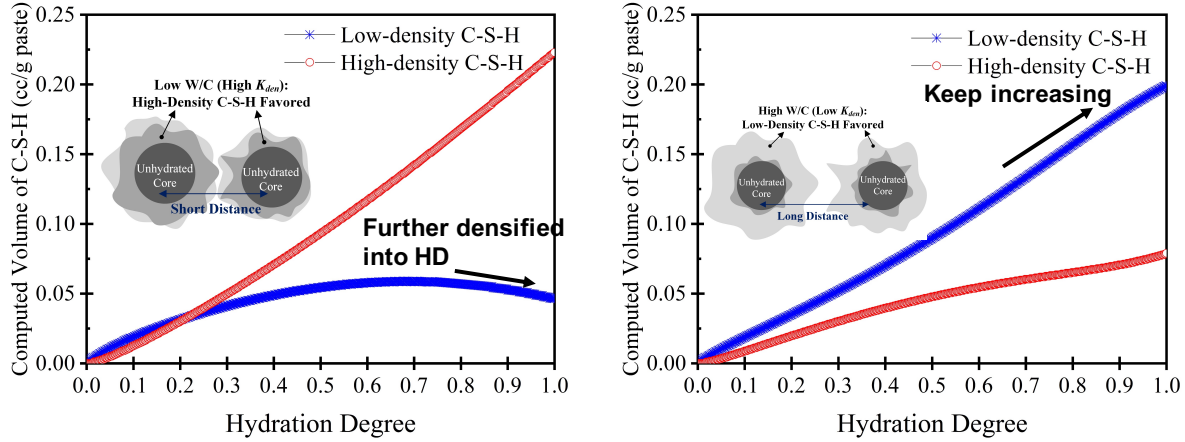


Figure 3.18 Computed volume of two groups of C-S-H under for varied w/c under normal temperature

The predicted capillary porosity and the surface area are validated through a variety of studies. For the determination of surface area, only the experimental data of C₃S and OPC samples using d-drying method is summarized, since the d-dried density is used in the numerical model. The model can also be extended for prediction of nitrogen-accessible surface area using other drying methods, if the well-defined density is provided. Various drying methods only change the predicted values of surface area and does not change the densification mechanism and evolution pattern. As found from Figure 3.19, the model can predict the capillary porosity well ($R^2=0.95$) and also, for the predicted surface area (the optimized S_{LD} is 220 m²/g), the accuracy is acceptable. Noted that due to the balance of the total volume, if capillary porosity is reasonably predicted, it can be inferred that the amount of total C-S-H is adequately predicted. Because the predicted surface area is closely related to the amount of LD C-S-H, it can be further expected that the mass ratio of LD C-S-H to total C-S-H is also considered reasonably.

3. The Thermo-Hygro-Mechanical Model

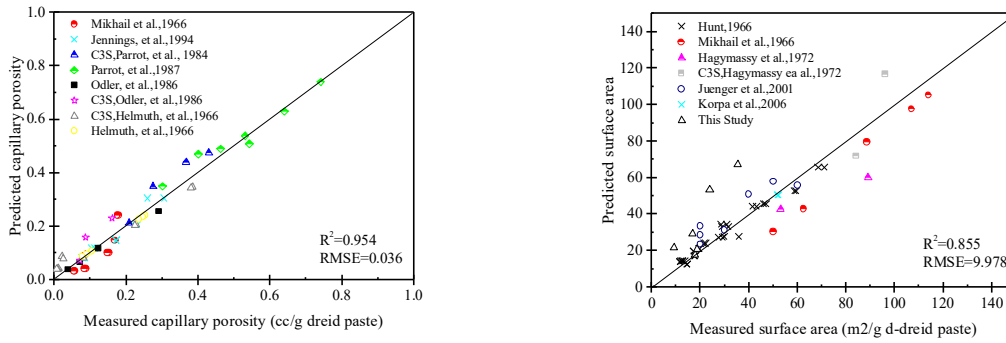


Figure 3.19 Validation of capillary porosity (left) and surface area (right) through a variety of studies.

The combined effect of densification and volume expansion is closely related to the densification rate K_{den} , which governs the formation and ratio of two types of C-S-H. The densification rate turns out to be affected by the chemical environments and the underlying thermodynamics of the solution, including w/c, age, the addition of SCMs or temperature conditions. Recent studies on molecular dynamics also suggests the formation of C-S-H relies heavily on the interplay of hydrate production rate (Ioannidou, Pellenq and Del Gado, 2014; Ioannidou, Kanduč, *et al.*, 2016). It suggested that the packing, local density, morphology and mechanical properties can all be associated with the effective interactions of nanoparticles during hydration. At the early times, the interaction potential is dominant by HS (high-shoulder) potential. Gel particles will grow as fibrils that branch and percolate the whole pore system, which is also characterized as the accelerating regime of the hydration kinetics. This process could be envisaged as the preferable formation of LD CSH in our study, as shown in Figure 3.20. While at the later age, the interaction between HS and LS potential will take place, the interplay between HS and LS potential alters the mass ratio between low-density fibrillar structure and high-density compact structure. With this holistic scheme, the correlation between structural formation, hydration kinetics and mechanical properties could be understood more comprehensively.

3. The Thermo-Hygro-Mechanical Model

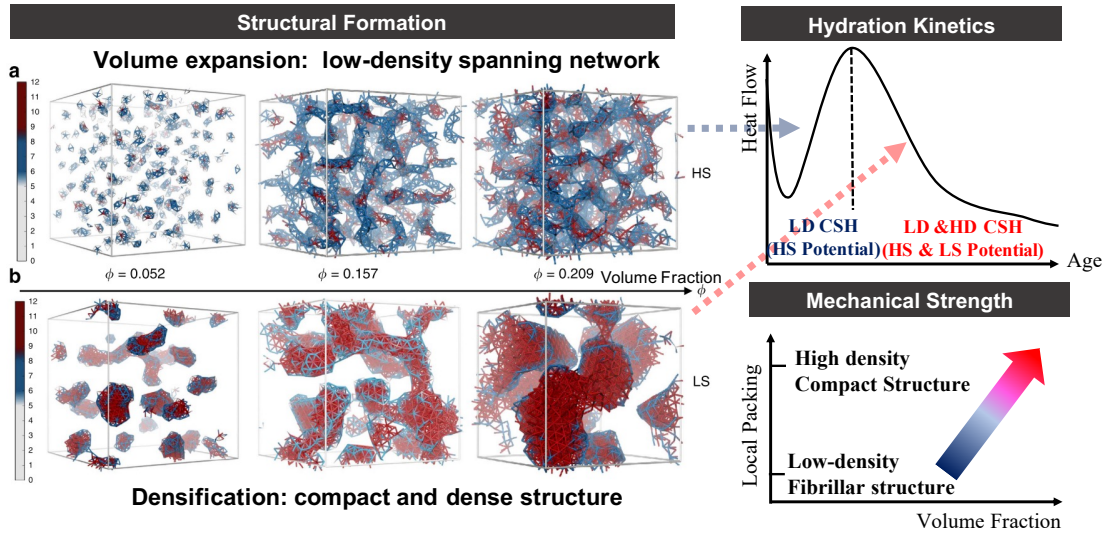


Figure 3.20 A schematic diagram of correlation between densification and volume expansion (Modified from (Ioannidou, Kanduč, *et al.*, 2016))

3.4.3.6 The interpretation of total porosity detected by nitrogen adsorption test

In the past, the total porosity detected by nitrogen adsorption has caused many confusions due to its unclear trends with respect to w/c, hydration degree or other parameters. The total porosity accessible to nitrogen cannot be well predicted by the CM-I model (Tennis and Jennings, 2000). As the number of experimental data increases, the fitting error increases significantly. Noted that the detectable range of nitrogen adsorption test is around several nm to ~60nm (at most 100nm). It can be considered that gel pores (with only several nm) and some portions of capillary pores (from around 10nm to 100nm) are intermixed into the measured total porosity. But as a general understanding, capillary porosity decreases as time, gel porosity will increase with time (since more hydration products are formed). This may hinder the correct interpretation on the total porosity accessible to nitrogen, unless a very well-defined and clear separation between gel and capillary pores could be made. Herein, we summarize a series of reported research (to the author's best knowledge), and attempt to figure out the relationship between the measured surface area and total pore volume. As shown in Figure 3.21, the nitrogen adsorption test with variables of different drying methods, curing temperature, addition of CaCl_2 , OPC or C_2S , w/c and curing age are summed up. One group of data includes only one variable in one study, and it is plotted with one specific symbols. By this way of classification, it can be found that there is not very clear linear relationship between the detected surface area and total porosity. The value of R^2 ranges from 0.98 to very small value around only 0.27. In several cases, when surface area increases, the measured total porosity even decreases. Interestingly, if we only consider the porosity of finer pores (smaller than 8 nm) rather than the total porosity, the linear relationship is clearly found, with all $R^2 > 0.95$, as found in Figure 3.22. Only two groups of data (pink data) show less clear linear relationship ($R^2=0.73$ and 0.81 , respectively), since only pores in a larger range (up to 20nm) are reported. Surface area is generally used as an index and directly linked with the amount of

3. The Thermo-Hygro-Mechanical Model

CSH products (Jennings and Tennis, 1994; Hamlin M. Jennings, 2000; Tennis and Jennings, 2000). It indicates that these finer pores (mostly smaller than 8nm) are the true gel pores that will scale with the amount of CSH products (or surface area), while the larger pores detected by nitrogen adsorption tests may not offer us valuable information.

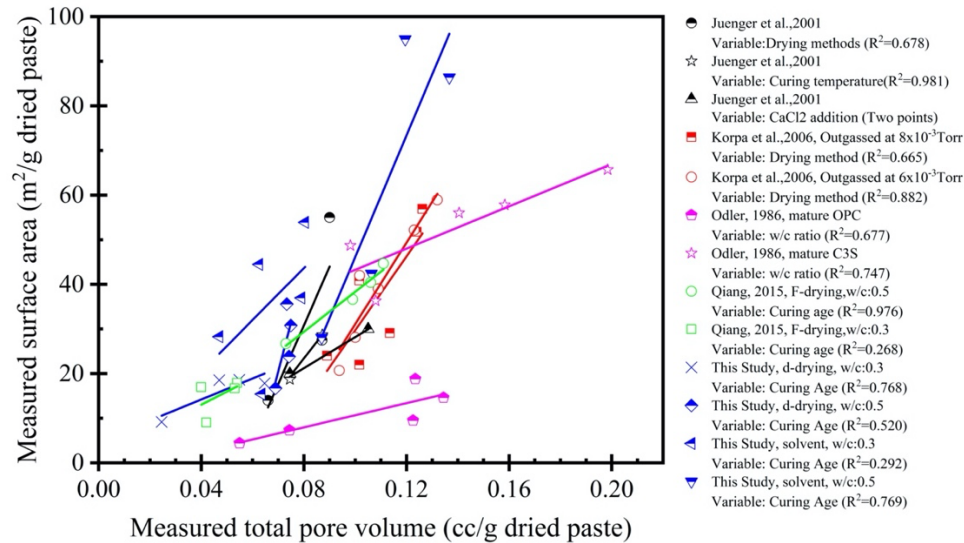


Figure 3.21 Relationship between measured surface area and total pore volume by NAD test

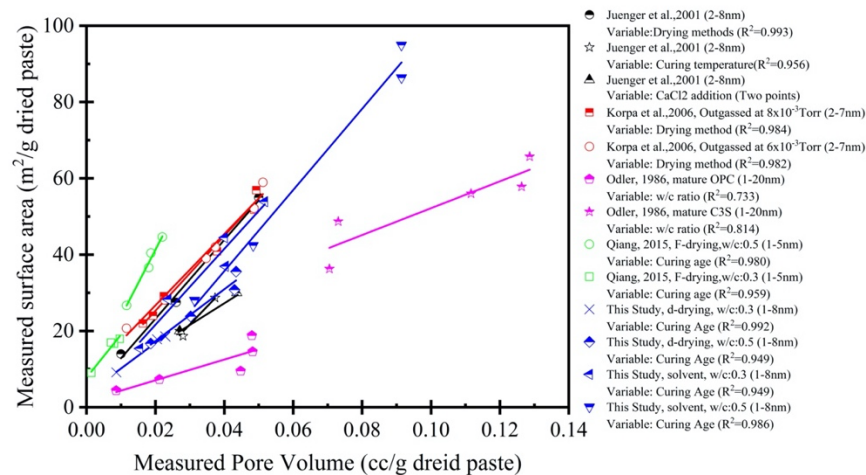


Figure 3.22 Relationship between measured surface area and finer pores by NAD test.

Pore size distributions of our experiments are plotted in Figure 3.23. It can be found out that under a low w/c ratio of 0.3, the smaller pores with a diameter less than 8nm corresponds well to the growth of LD C-S-H. According to the densification mechanism discussed above, the detectable amount of gel pores in LD C-S-H (also, the surface area) will increase with hydration time and then decrease. While in a high w/c ratio case, the amount of gel pores in LD C-S-H constantly increases with time. It can be considered for the larger pores detected by NAD test, those are small capillary pores which are located at the boundary region between the LD C-S-H and the larger

3. The Thermo-Hygro-Mechanical Model

capillary pores, subjected to the complex combined effect of densification and volume expansion. Therefore, these small capillary pores found by NAD test show no clear physical meanings and evolution trend with hydration time, w/c, etc.

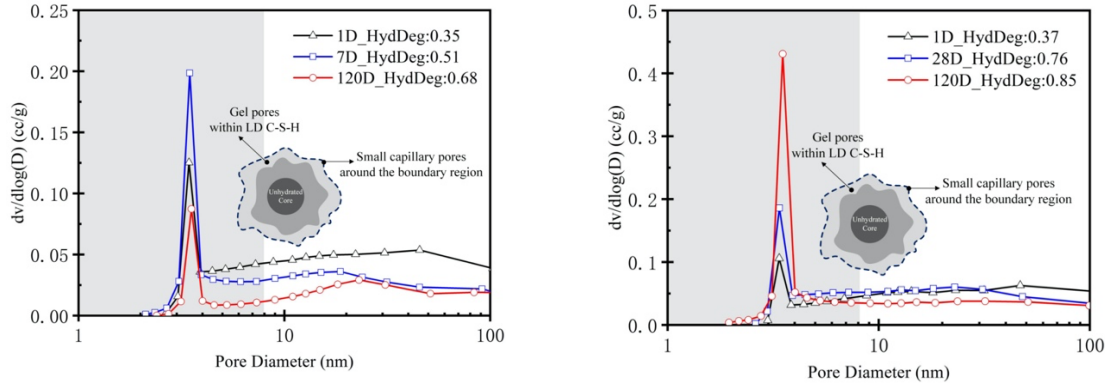


Figure 3.23 Pore size distribution of nitrogen-accessible pores. Left: w/c=0.3, Right: w/c=0.5.

3.4.3.7 The effect of high temperature on pore structure

In this section, the effect of high temperature on the nitrogen-accessible surface area is discussed. The development of surface area with age is plotted in Figure 3.24. Actually, it is more meticulous to plot the surface area versus degree of hydration rather than age. Because even for the same hydration age, the hydration degrees for specimens cured at different temperature will be varied. For example, the specimen cured at 65 °C for one day will have much higher hydration degree than the specimen cured at 22 °C for one day. But since data points will be quite congested within certain range of hydration degree, for better visualization, it will be plotted versus time. The overall development pattern will be mainly discussed. As shown in Figure 3.24, compared to the 22 °C case, the effect of 40 °C on the surface area is not so pronounced. But for 65 °C, the surface area is much lower, due to the coarser pore structure. Since the meso-pores at several nano-meter may be further densified, meanwhile the denser hydration products generate more capillary pores. It has also been previously reported that with higher curing temperature, the nitrogen-accessible surface area will be lower (Skalny and Odler, 1972). Again, the surface area determined using solvent-exchange method showed higher values than d-drying. For the high w/c group, at later time of 40 °C and 65 °C, the increase of surface area may level off or even decrease at later time. This effect is not shown in the 22 °C case. It might be attributed to the effect of aging (Thomas and Jennings, 2006). The linear relationship between measured surface area and pore volume (1-8nm) is found again, as shown in Figure 3.25.

3. The Thermo-Hygro-Mechanical Model

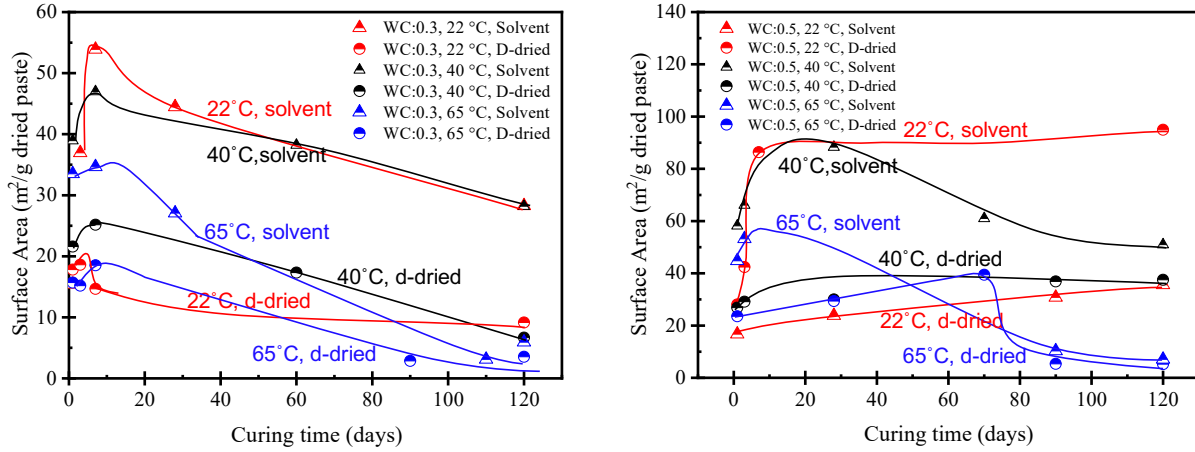


Figure 3.24 Effect of temperature on the surface area development of cement paste

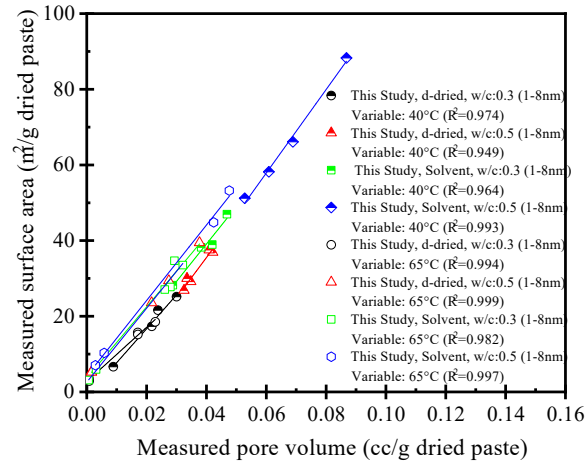


Figure 3.25 The Relationship between measured surface area and total pore volume (HighTemp)

3.4.4 Pore structure characterization of MgO and CSA concrete

The pore structure of MgO and CSA concrete can be compared and characterized, given the same curing condition and pre-treatment method. In this section, the MIP and NAD tests are also conducted on OPC, MgO and CSA cement paste specimens. In order to offer us insights for their behaviours under wetting-drying cycles discussed in Chapter 2, the w/c ratio used is the same as in the TSTM experiment, i.e., 0.45. The OPC used is the same JIS type. The replacement ratio of MgO and CSA to OPC is identical to the TSTM experiment as well, i.e., 10% is used.

- MIP tests on OPC, MgO and CSA cement pastes

After the samples has been sealed cured at 40 °C for 7 days, the mm-size paste samples are extracted by crushing. Then these samples are immersed into the isopropanol solutions to stop hydration. Subsequently, these samples are put into the d-drying desiccator for one day. After that, these samples are used for the MIP tests. The second intrusion process is also conducted to derive

3. The Thermo-Hygro-Mechanical Model

the ink-bottle porosity. The following equation shows the computation of the proportion of ink-bottle porosity in the total porosity accessed by MIP.

$$R_{ink} = (\phi_{Int-2nd} - \phi_{Int-1st})/\phi_{tot} \quad (3.42)$$

Where $\phi_{Int-1st}$ and $\phi_{Int-2nd}$ denote the 1st step intruded volume at the 1st intrusion and 2nd intrusion process, respectively. Then this valued is normalized by the total porosity to derive the ratio of ink-bottle porosity to total porosity.

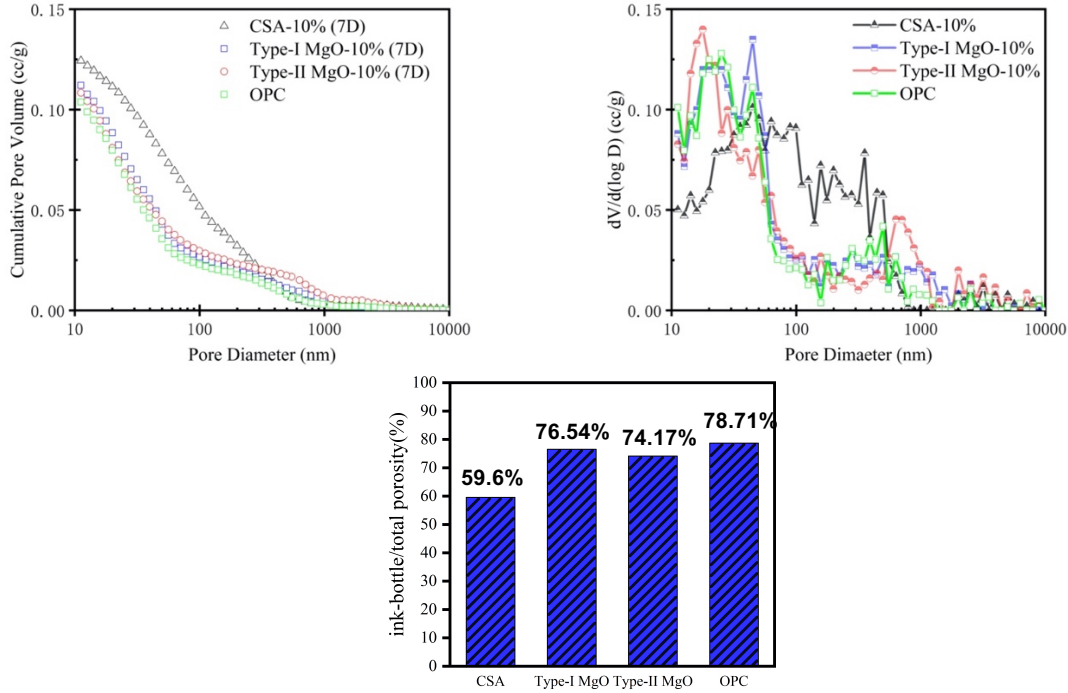


Figure 3.26 The pore structure of OPC, MgO and CSA paste samples measured by MIP

Figure 3.26 shows the pore structure characterized by MIP. It can be shown clearly by the top panel that, the CSA samples have a higher total porosity (in the range of >10nm). Additionally, the pore size distribution graph denotes that CSA samples reveal a much coarser pore structure than MgO samples, with most of the capillary pores located at 30-500nm. While the MgO paste samples have a peak of capillary pores at around 10-30nm. Interestingly, two types of MgO shows very similar porosity and pore size distribution as OPC. It should be noted due to the drying pre-treatment and the ink-bottle effect of MIP technique, the measured pore size distribution of MIP may not truly represent the realistic pore structure. However, comparable information between specimens can still be provided. It offers us valuable interpretation on the difference between various materials. As shown in the bottom panel of Figure 3.26, the ratio of ink-bottle porosity is much higher for MgO and OPC paste samples, in comparison with CSA samples. As a summary for the MIP results, MgO paste samples has less large capillary porosity, much finer pore structure and more ink-bottle porosity.

3. The Thermo-Hygro-Mechanical Model

- NAD tests on OPC, MgO and CSA cement pastes

During the NAD tests, the pre-treatment technique is the same as those aforementioned solvent-exchange method. It can be found out that the OPC, two types of MgO paste samples all reveal larger amount of fine pores with size of ~3 to 4 nm, in comparison with CSA concrete, as shown in Figure 3.27. It also indicates a finer pore structure system of OPC and MgO, in line with the MIP results.

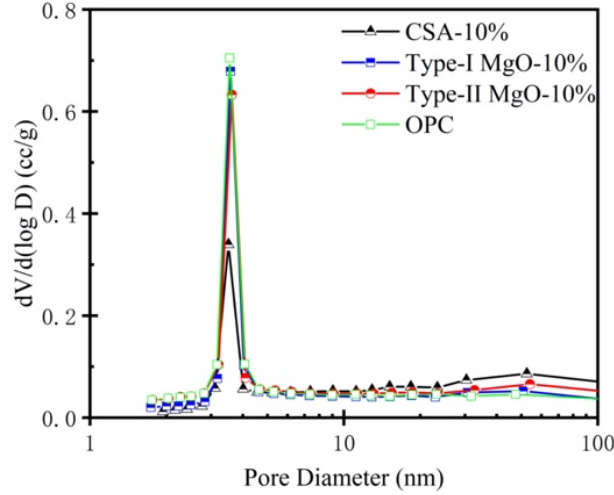


Figure 3.27 Fine pores of OPC, MgO and CSA paste samples detected by NAD tests

It is very possible that, due to the much finer pore structure and more amount of bottle neck pores of MgO sample, it hinders the moisture evaporation process, revealing much better resistance to the drying shrinkage. It is considered as one of the major mechanisms for the smoother stress development found in the wetting-drying cycles in Chapter 2. Because the major driving force for drying in the range of capillary pore size is the capillary tension (Lura, Jensen and Van Breugel, 2003; Luan and Ishida, 2013). A coarser pore structure will lead to the much easier loss of moisture, which induces higher shrinkage forces. As an estimation from the capillary tension theory (shown in the following Eq. (3.43)), the shrinkage value is proportional to the saturation degree S inside the pore system. A drop of 50% of the saturation degree in pores will lead to a double increment of the shrinkage values (if this shrinkage is confined, it is converted to shrinkage stress).

$$\varepsilon_{LIN} = \frac{P_l \cdot S}{3} \left(\frac{1}{K} - \frac{1}{K_s} \right) \quad (3.43)$$

3.4.5 A hypothesis on the nanostructure of C-S-H

The modelling of OPC system resolves the controversies on the densification mechanism and pore structure development. It provides more appropriate interpretation on the experimental results of NAD test. But such information is related to the bulk properties of the C-S-H only (mass, bulk density, porosity, etc.). The proposed numerical model up to here does not contradict with the

3. The Thermo-Hygro-Mechanical Model

Feldman-sereda model or the Jennings Model, since the discussion does not involve deeply with the nanostructure of C-S-H. In the next step, it is required to understand better on the nanostructure and consider how to reasonably define varied groups of pores and their roles on the moisture movement behaviours. Then, the computed porosity can be assigned to the pore size distribution. Also, based on the experimental results on MgO and CSA paste samples from last section, the pore size distribution will also be modelled accordingly.

As for the classification of pores and their moisture state, experimental data on $^1\text{H-NMR}$ techniques offer us valuable interpretations. One major advantage of this experimental technique is that, no drying pre-treatment is required. The continuous measurement on the specimen can be conducted while preserving the original pore structures of interest. Due to the recent advancement of the coupled QE-CPMG pulse sequences (Muller *et al.*, 2013), all the water in the system are “seen” by $^1\text{H-NMR}$, which provides us meaningful information on the moisture state of each group of pores. The theoretical background of this technique is not elaborated here.

A series of published $^1\text{H-NMR}$ data are chosen as the basis of our proposed hypothesis. Firstly, a categorization of pore groups and their size in line with several $^1\text{H-NMR}$ studies are provided as the following (mostly based on the relaxation time T2 and the fast-exchange model (Muller *et al.*, 2013; Gajewicz *et al.*, 2016)):

1. Interlayer Pores (~ 0.85 nm to 1 nm)
2. Gel Pores (2 nm to 5 nm)
3. Inter-hydrate Pores (10 nm)
4. Capillary Pores (> 10 nm)

Please noted that, the pore size of interlayer may induce systematic error, due to the absence of identifiably “bulk” water reservoir in the pore and the uncertainty of the surface relaxivity (Gajewicz *et al.*, 2016). The magnitude of error can be up to a factor of two. The error of the interlayer pore size also depends on in which angle and volume of the water is seen by $^1\text{H-NMR}$ (Muller, 2014). Generally, in a typical tobermorite 14 \AA (a mineral analogue of C-S-H), the interlayer spacing is just around one layer of water molecule, $\sim 3 \text{ \AA}$ to 4 \AA .

Apart from the pore categorizations, another valuable information is the water exchange behaviour detected by $^1\text{H-NMR}$. It is found by Maruyama (Maruyama *et al.*, 2019) that the moisture exchange behaviour takes place between the interlayer pore and gel pores during first drying process. It is suggested by P.J. McDonald that, the gel pore and interlayer water are isolated from the capillary water by C-S-H sheets. It is also evidently found that water exchange behavior is taking place between gel pores and inter-hydrate pores during wetting-drying cycles (Gajewicz *et al.*, 2016). Interestingly, it is reported for the first time that around 150 MPa of the hydrostatic pressure also causes the gel pore water to be expelled to the larger pores (inter-hydrate pores and capillary pores), as well as the interlayer pores (Wyrzykowski *et al.*, 2019). By summarizing all

3. The Thermo-Hygro-Mechanical Model

of these newly found phenomena, it is known that these very fine gel pores play a key role on the water exchange behavior.

Even though the pore structure has been studied for a long time, up to the current stage, the role and location of gel pores are still under controversies and hot debate (Muller, 2014). Herein, we are proposing a hypothesis on the nanostructure by new interpretations on the ^1H -NMR data. Figure 3.28 shows the three-dimensional schematic diagram of our proposal.

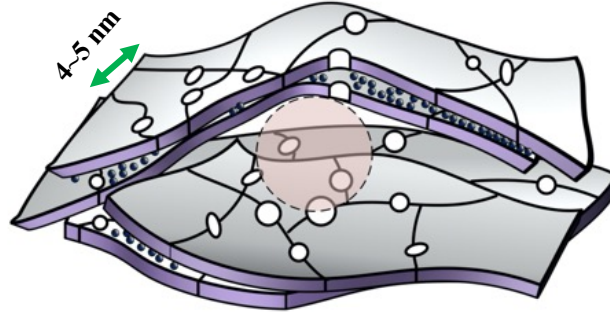


Figure 3.28 A new proposal of three-dimensional nanostructure of C-S-H

[white: gel pores on the skeleton of CSH; Purple: layers of C-S-H consists of inter-layer water inside; Orange: inter-hydrate pores encaged by CSH sheets]

It is considered that these gel pores (size around 2-3 nm) are mainly located at skeleton of the C-S-H sheet, which are penetrating through these C-S-H sheets. These gel pores are acting as a gateway (or bypass) for water exchange behaviours. In this manner, water exchange not only takes place between gel pores and inter-layer pores, but also between gel pores and larger pores (inter-hydrate pores and capillary pores). Therefore, those experimental findings from ^1H -NMR could be consistently explained, which shows that water exchange behaviour between these pores are indeed detected. The formation of these gel pores can be considered by the defects on the layered structure of C-S-H. Some supportive evidence could be found from some studies on molecular structure. It is known that for a 14 Å tobermorite, it has a Ca/Si ratio of around 0.83. This value is quite low compared to the Ca/Si ratio of C-S-H, which ranges from 1.2 to 2.1. It is quite possible that, in order to achieve higher Ca/Si ratio, the removal of bridging tetrahedra (SiO_2) and the addition of calcium ions or CaO and $\text{Ca}(\text{OH})_2$ can result in a defective layered structure of C-S-H with varying compositions (Mohamed *et al.*, 2015). It is considered that the gel pores detected by ^1H -NMR may be mainly locating at two positions. First type is those gel pores penetrating the C-S-H layer, which can be formed as defects at the boundary of C-S-H units during the growth of these units. When these C-S-H units start to grow and impinge with each other during hydration, defects are induced. These gel pores are the major part. The second type might be induced by the misalignment of these units (Muller, 2014). There might be some uneven irregularities when different units are stacking together. These irregularities might be detected with similar size of

3. The Thermo-Hygro-Mechanical Model

gel pores. There are some numerical studies recently showing that the planar, layering and defective growth of small C-S-H sheets (similar to the platelet proposed here) can reproduce the morphology of C-S-H detected by SEM or TEM at the larger scale, and some porosity properties (Etzold, McDonald and Routh, 2014; Nguyen-Tuan *et al.*, 2020).

In terms of experimental data to estimate the size of each C-S-H unit, it was found by (Muller *et al.*, 2013) that the gel porosity/interlayer porosity is around 2:1. Also, it was found that the number of locally stacked layers in region of C-S-H is around 2~ 3 at 28 days of hydration. When we are considering a region with two stacked layers of C-S-H with one layer of inter-layer water in between ($\sim 3\text{\AA}$), supposed these gel pores are penetrating through the C-S-H sheet, and it can be estimated that the size of each small C-S-H unit is around 4-5 nm. Which, interestingly, is in good agreement with the globule size in Jennings model. The C-S-H unit in the proposed nanostructure of this study is termed as “platelet”. The platelet-like structure of C-S-H shown in Figure 3.28 may bridge some of the colloidal properties in Jennings model and some other properties in Feldman-sereda model. In Figure 3.29, a multi-scale schematic diagram of the proposed model is also provided.

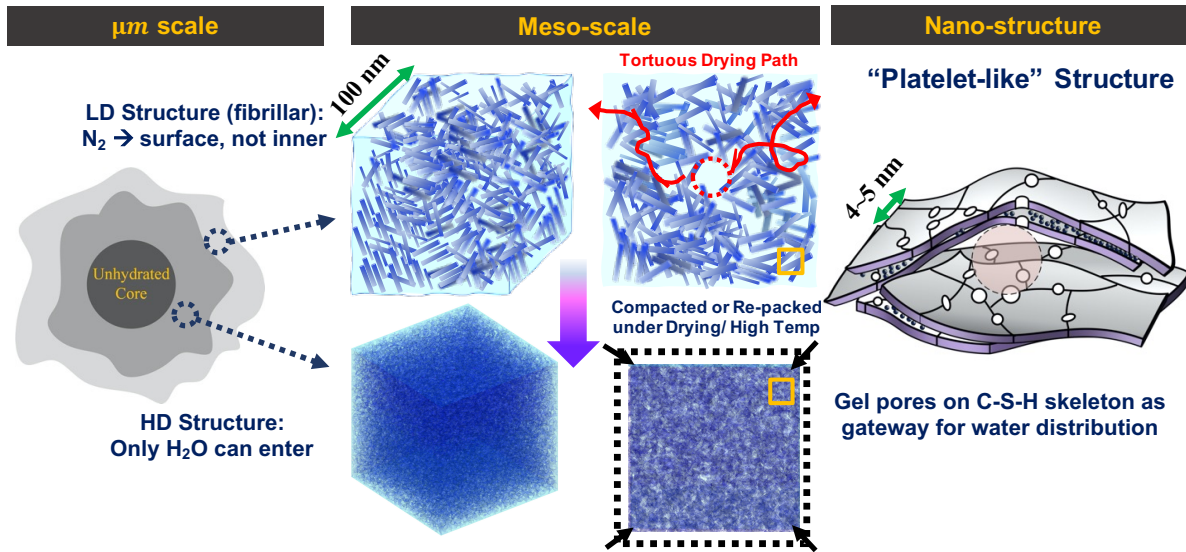


Figure 3.29 A multi-scale schematic diagram of C-S-H structure

Interestingly, there is also one supporting evidence from MIP for inter-hydrate pores with diameter around 10 nm. The multi-cycle MIP conducted by R. yoshida (Kishi and Yoshida, 2008) shows that, two distinct types of MIP intrusion profiles are found when mercury is intruding the cement paste. They are separated by a threshold diameter around 10 nm, as shown in Figure 3.30. It can be interpreted that, before the mercury is reaching the threshold pressure, it is detecting some continuous and ink-bottle capillary pores, while after the threshold has been reached, it intrudes inside the inter-hydrate pores (10nm) and cause some deformation (not damage/fracture).

3. The Thermo-Hygro-Mechanical Model

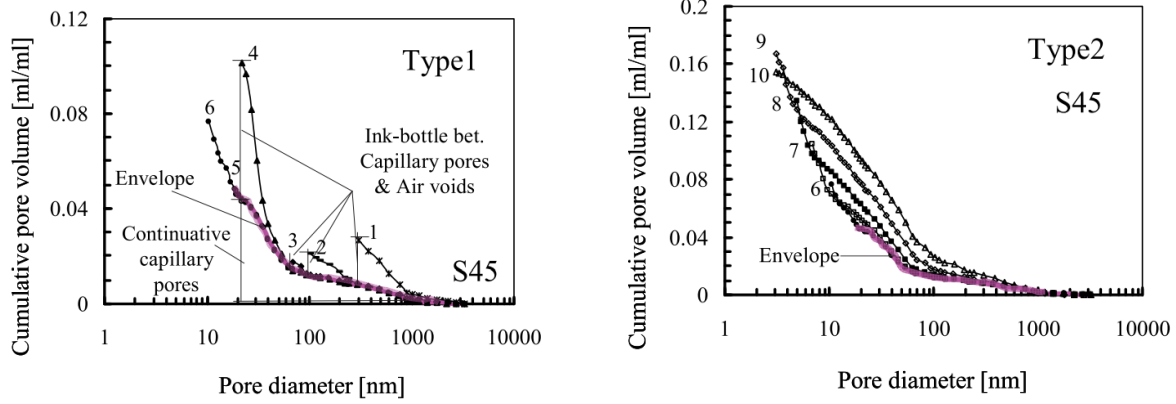


Figure 3.30 Multi-cycle MIP on sealed-curing paste with w/c:0.45 (after (Kishi and Yoshida, 2008))

3.4.6 Pore size distribution and moisture state of OPC, MgO and CSA

In our study, the pore classifications are same as those detected by $^1\text{H-NMR}$. That is to say, there are inter-layer pores, gel pores, inter-hydrate pores and capillary pores. The porosity of each group of pores can be estimated by the bulk density of C-S-H at varied scales. The used density values include density of single layer of C-S-H sheet, density of aggregates of C-S-H layers, bulk density of both LD and HD C-S-H (Tennis and Jennings, 2000; Allen, Thomas and Jennings, 2007; Jennings, 2008a; Muller, 2014). Detailed computation can be referred to the appendix. The capillary porosity and “gel porosity” is in good agreement with Powers’ data (Powers and BROWNYARD, 1946). It is considered for HD C-S-H (tightly-packed agglomerates): 10% interlayer porosity, 20% gel porosity, 12.8% inter-hydrate pores. In terms of LD C-S-H (loosely-packed agglomerates): 10% interlayer porosity, 20% gel porosity, 24.7% inter-hydrate pores.

After knowing about the porosity in each group of pores, the pore size distribution can be expressed by the modified Rayleigh-Ritz distribution function as

$$\phi(r) = \sum \phi_i \cdot \exp(-B_i d^{C_i}) \quad (3.44)$$

Where i represents different groups of pores. Where B is related to the location of the peak, and C can determine the shape of the distribution (to be coarser or finer). This is an extra term added into the original Rayleigh-Ritz function. For the determination of the functions $B=B(\alpha, w/c)$ and $C=C(w/c)$, exponential functions and linear functions could be used tentatively. For example, when dealing the time-dependent property, exponential function can be used for simulating the rapid refinement of pore structure at the early-age. But, these functions are not randomly set. As a criterion to set up these functions: based on the coupled scheme introduced previously, the saturation degree inside pores can be estimated and the RH development can be derived. This predicted RH development should be in reasonable agreement with reported experimental data on RH development of sealed-curing paste materials (Lura, Jensen and Van Breugel, 2003). If more

3. The Thermo-Hygro-Mechanical Model

quantitative data on the “realistic” pore size distributions is reported in the future, it can be updated by more accurate mathematical expressions in the future.

For the pore structure of CSA cement paste, according to the experimental data in **section 3.4.3.8**, several assumptions are made: 1. Pore structures between OPC and MgO are the same. 2. The total porosity between OPC, CSA and MgO is assumed to be the same (because in experiments we do not find much differences between them) 2. There will be more 50% less inter-hydrate pores and 40% less gel pores in LD C-S-H for CSA (estimated from the MIP and NAD results). Since the total porosity is kept the same, correspondingly, CSA will have higher large capillary porosity. This treatment of pore structure can be input in the coupled model, so that the saturation degree inside pores can be determined. Based on Kelvin-Laplace equation, the RH and the pore diameter d_c (pores larger than which are emptied) can be estimated.

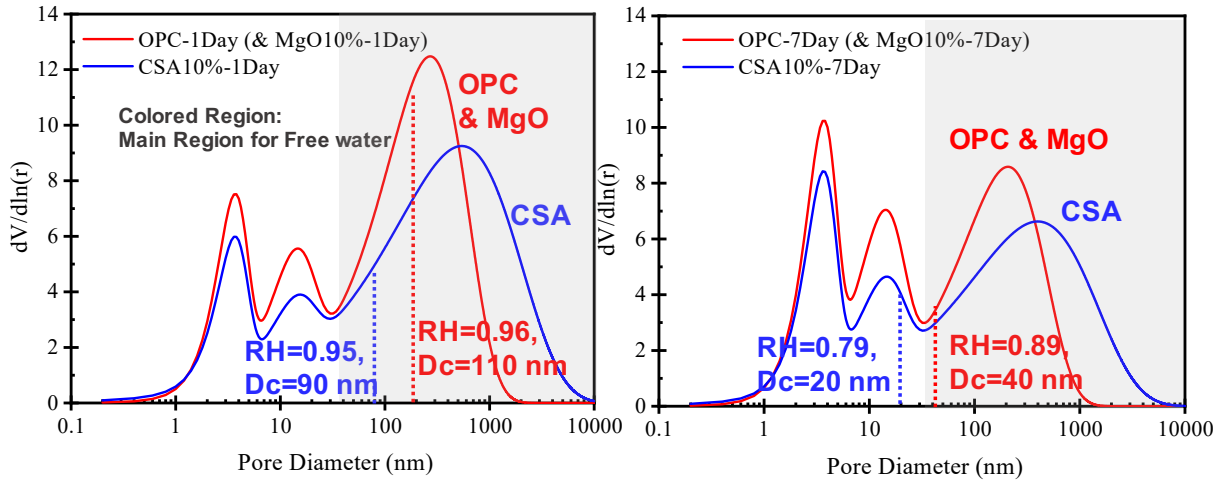


Figure 3.31 Development of Pore Structure and Moisture State for OPC, MgO and CSA concrete

The computation results of pore structure development for OPC, CSA and MgO is plotted in Figure 3.31. The analysis is conducted for paste samples with w/c:0.45 under high temperature sealed-curing condition. The simulated dosage of CSA and MgO is 10%. The left panel is for 1st day and the right is for 7th day. The interlayer pores are not plotted for simplicity which only possess the size around one water molecule. The red curve represents the OPC and MgO paste with three peaks: the gel pores, inter-hydrate pores and capillary pores. The gel pore has a diameter of around 2-5nm, the inter-hydrate pore has around 10 nm diameter and the capillary pores will be shifted to a finer range at later age. For the blue curve, CSA has a coarser pore structure than the OPC, with the peak of capillary pore locating at ~700 nm at 1st day to ~500 nm at 7th day. The volume of capillary pore is higher and that of finer pore (inter-hydrate and gel) is smaller than OPC. The graded region is the capillary pore space, which is the main region for condensed free water.

3. The Thermo-Hygro-Mechanical Model

According to the Kelvin-Laplace Equation (Eq.3.5 with modification parameter 2.15), the pores smaller than d_c will be saturated and larger than that will be empty. It is found that, after one day of hydration of OPC, the RH drops to 0.96 due to self-desiccation, and the d_c is around 110 nm. There is still a large portion of free water can be used for hydration. Regarding the CSA, d_c is dropped to 90 nm (since CSA consumes more free water compared to OPC). Also, due to the coarser capillary pore structure, a large part of the free water has been consumed. This phenomenon is more obvious at 7th day, with d_c for CSA dropping to ~20 nm.

By using this coupled scheme, one can understand the underlying physical mechanism of the ineffective expansion of CSA under high temperature condition. Due to the stronger self-desiccation effect and coarser pore structure, it can be found by the analytical model that, at around only one day, a large part of free water has been depleted. Other reason may be attributed to the discontinuity of pores (or blockage of pores) during the formation of hydration products. It is also mentioned in **section 3.4.3.8** that, from MIP and NAD results, CSA cement paste does show less ink-bottle porosity and less bottle neck pores. These reasons together lead to the rapid drop of free water availability (β_{CSA} in **section 2.9.2**).

3.4.7 The insight on drying behaviour

The complex time-dependent drying hysteresis of cementitious materials remains as a mystery. Its pattern reveals the complexity of the multi-scale pore structure. For example, the experimental results from Grudemo show interesting drying hysteresis behaviours (Grudemo, 1979), which may offer us some important implications. The experiment was carefully conducted and provided meaningful interpretations on the role of pore structure during drying, as shown in Figure 3.32. The experiment was conducted on C₃S specimen with only 1 mm of the thickness. Water-to-cement ratio of the specimen was 0.50, and it was cured for 5.8 years. Non-equilibrium drying condition was conducted under atmosphere of given relative humidity. The hysteresis shows a RH-dependent behaviour. The hysteresis effect is the highest between RH= 0.2 and 0.8. Such a behavior is also found by ¹H-NMR (Maruyama *et al.*, 2019) that time to reach the equilibrium state under RH=40% is much longer than that under RH=11% and RH=80%. One can envisage that due to the interlock of inter-hydrate pores (~10 nm) by gel pores (2-5nm), as shown in Figure 3.28, a large portion of inter-hydrate pores may take a very long time to be evaporated, featured by the tortuous and complex drying path. However, if under hasher drying condition, e.g., RH=10%-20%, the pores with diameter around 2-3nm will be dried (computed from Laplace-kelvin equation with modified parameter 2.15). Once these gel pores are emptied, it serves as bypass for water evaporation process, which facilitates the water evaporation and lead to shorter time to reach equilibrium. It can be considered that the gel pores and its relationship with inter-hydrate pores play a key role on this complex time-dependent hysteresis. It is also noteworthy that, 170 days in this study may only be a pseudo-equilibrium state. It possibly leaves unexplored hysteresis behaviours from pseudo-equilibrium to theoretical-equilibrium state, which can be studied further in the future.

3. The Thermo-Hygro-Mechanical Model

Furthermore, as new ^1H -NMR findings (Wyrzykowski *et al.*, 2019) indicate that hydrostatic pressure from 1 to 100 or 120 MPa does not show any evident effect of water redistribution from gel pores to different groups of pores (inter-layer, inter-hydrate and capillary pores). While 150 MPa of the pressure shows very pronounced effect of this water redistribution. Based on the Kelvin-Laplace equation, this pressure corresponds to the pore size around 2-3 nm. Maruyama (Maruyama *et al.*, 2018) also finds that the cavitation of cement paste during desorption takes place at a pressure of -140 MPa. Therefore, it can be envisaged that until the pressure reaches this threshold value (the required pressure to press the water in these small gel pores), the water between different groups of pores cannot be easily exchanged. While once this gateway is “open” (emptied), the water exchange behaviour becomes applicable. It supports the hypothesis that these gel pores may act as the gateway for varied groups of pores.

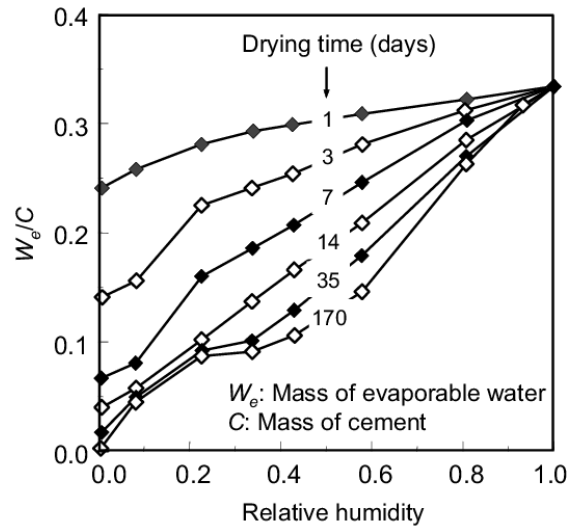


Figure 3.32 Hysteresis behavior of the 1 mm-thick C_3S sample during drying (After (Grudemo, 1979))

3.4.8 Limitations of the pore structure model and current gap of understanding

Even though in the current model, it has same pore classifications as that detected by ^1H -NMR, however, we consider C-S-H is composed of agglomerates with certain amount of inter-hydrate pores (comparable amount with gel pores), but ^1H -NMR data shows much less amount of inter-hydrate pores and more inter-layer and gel pores (Muller *et al.*, 2013; Muller, 2014). Our numerical computation of porosity is formed on the basis of dried densities from traditional techniques. Our model shows good agreement with Jennings model and Powers model, but the gap of understanding still exists between current model and some ^1H -NMR data. Some researchers (Muller, 2014) attribute this gap to the necessary drying pre-treatment of specimen when using traditional techniques (MIP and NAD, etc.), this pre-treatment leads to less gel porosity. But for ^1H -NMR, drying pre-treatment is not necessary and thus, the detecting gel porosity could be higher.

3. The Thermo-Hygro-Mechanical Model

It is also noteworthy that, ^1H -NMR finds that gel pores (diameter 2-5nm) can even start losing water at $\text{RH} > 0.95$, this process continues to $\text{RH} \sim 0.2$, as shown in Fig 4.24 of the reference (Muller, 2014). Such a phenomena could not be explained by the Kelvin-Laplace Equation, since such fine gel pores should remain saturated under such a high RH. Also, the amount of gel pores and interlayer pores is quite high. Supposed that this is a realistic phenomenon, it implies gel pores play a dominant role in the drying shrinkage under a wide range of RH, which does not agree with traditional considerations. For example, it was thought that capillary pores will play a crucial role in the drying shrinkage at relatively high RH by effect of capillary tension (Lura, Jensen and Van Breugel, 2003; Maekawa, Ishida and Kishi, 2009; Luan and Ishida, 2013). But the volume of inter-hydrate pores and capillary pores detected by ^1H -NMR is quite small. During desorption, most part of water loss is contributed from gel pores and interlayer pores.

These gaps remain controversial but significant for both scientific understanding and engineering problems of drying behaviour (though drying is not the main scope in this study), which may require us to revisit the traditional theories about the driving forces of drying, like the surface tension, disjoining pressure and capillary tension.

4. Conclusions and Future Perspectives

4.1 Conclusions

This study experimentally evaluates and compares the cracking performances of OPC concrete and two types of contemporary expansive concrete (CSA and MgO concrete), using the temperature stress testing machine (TSTM). Systematic experiments on early-age deformation and stress development of OPC, CSA and MgO concrete have been conducted. For OPC concrete, it has been found out that the rapid development of autogenous shrinkage of high strength concrete results in the cracking at very early age. Even though the 28-day strength is quite high, but it cannot catch up with the rapid development of tensile strength under the high temperature and full restraint condition. Additionally, it is shown that without adequate restraint effect from aggregate, the autogenous shrinkage of OPC concrete is increased, leading to a higher cracking sensitivity. Regarding CSA concrete, it is confirmed that CSA concrete fails to compensate rapid shrinkage stress effectively under high temperature and full restraint condition, while its hybrid use with lightweight aggregate indicates excellent cracking performance (Firstly discovered by Lin (Lin, 2006), part of experiments are repeated in this study). Importantly, the relatively new expansive additive MgO can offer prolonged expansion due to the less water dependency for complete hydration, compared to normal CSA concrete. Type-II MgO reveals nice performance to compensate shrinkage under high temperature condition, which has a potential to be applied into real construction site to control early-age cracking. Also, this study shows for the first time that MgO concrete has better resistance to drying stress than CSA concrete under wetting/drying cycles. Plausible mechanisms can be attributed to the retarded expansion due to less water dependency and the finer pore structure which slows down the water evaporation from pores. Experimental results from nitrogen adsorption-desorption (NAD) tests and mercury intrusion porosimetry (MIP) show that MgO concrete has finer pore structure and more bottle neck pores, thus hindering moisture movement during drying.

With respect to the analytical work, a multi-scale thermo-hygro-mechanical model is established, which is able to trace the development of free deformation and full-restraint stress under arbitrary temperature conditions. It offers practical value for mix design on-site. A new concept to interpret and model the expansion for CSA concrete is proposed. It is considered that the rapid drop of free water availability leads to ineffective expansion of CSA concrete, while a combined use with lightweight aggregate can solve this problem because of internal curing effect. The free water availability for CSA concrete with/without lightweight aggregate could be quantified reasonably by the coupled thermo-hygro-mechanical model. To estimate the moisture state inside pores, a

4. Conclusions and Future Perspectives

new pore structure based on the combined effect between densification and volume expansion has been put forward. The proposed pore structure model attempts to link some of the conventional understandings with innovative interpretations from ^1H -NMR technique. It is served as a preliminary but fundamental step to clarify the role of each category of pores and offer clearer insights on the behavior of moisture movement inside these pores.

4.2 Future Perspectives

- The further advancement and improvement of TSTM

The current version of UTokyo TSTM (ver. 1.1) is able to accurately quantify the deformation, stress and modulus development of concrete materials. As the humidity field is also important for us to understand the development of self-desiccation, in the future, the measurement of relative humidity will be incorporated into TSTM. Also, in order to simulate higher temperature condition, a better insulation system can be incorporated. To minimize the effect of fluctuation of room temperature, TSTM can be kept in a room with more rigorous temperature control to keep stable and constant room temperature. The deformation and stress development of concrete materials under freeze-thaw cycles can also be achieved by a well-designed insulation condition. Moreover, the digital image correlation (DIC) technique can also be incorporated to visualize the realistic deformation mechanism at the smaller scale. The experiments on the effect of steel bar could also be conducted, which offers us practical values on the economical usage of steel bars to control early-age cracking. With these new features, the TSTM can offers us very comprehensive and quantitative information on the concrete properties. It is expected that an innovative MSTM (Multi-functional Stress Testing Machine) can be constructed. Our research team is also working on the development of a small-scale TSTM, which is designed for mortar and cement paste materials (In courtesy of Dr. Z.H. Lin). The small-scale TSTM enables experimental operation with less labor work, though it imposes higher requirement on control of accuracy. As an overall blueprint, a more systematic and practical testing guideline for TSTM can be established. It provides us a practical evaluation method for durability performance regarding cracking sensitivities under complex and coupled thermo-hygro-mechanical conditions. It can be considered as a new testing criterion for concrete quality, which plays a comparable role as the commonly-used criteria like, compressive strength, workability, permeability, etc.

- A further study on MgO-type expansive additive

As found from this study, the MgO shows retarded expansion due to less water dependency. It also reveals better resistance to drying shrinkage, compared to the normal CSA concrete. In the future, more comprehensive studies on its compensation effect on the long-term drying shrinkage under various curing conditions can be expected. As drying shrinkage is closely related to the creep effect, the effect of long term creep on mechanical performances of OPC, CSA and MgO concrete can be studied and compared. Moreover, in this study, even though the proposed mix proportion has revealed acceptable cracking performances, a better optimization of mix design

4. Conclusions and Future Perspectives

can be conducted. Then, more practical mix design with balance of performance and economical cost can be achieved. The application of MgO concrete in more engineering projects is also a promising direction.

- Characterization of pore structure of OPC, CSA and MgO

¹H-NMR technique offers us valuable information on the moisture movement behavior between different groups of pores under wetting/drying cycles or mechanical loading. In the future, it would be meaningful to validate and modify our proposed hypothesis of the C-S-H structure at the meso-scale and nanoscale using ¹H-NMR. Especially, more well-considered experimental scheme under drying could be studied. As found from this study, the expansion properties of expansive concrete rely heavily on the free water availability. It will be interesting to experimentally figure out the difference of water exchange behaviors of OPC, CSA and MgO concrete under wetting/drying cycles, which may associate with the difference of pore structure (pore size distribution, tortuosity, connectivity).

5. Appendix

5.1 Modelling on Working Principle of Cracking Frame

The cracking frame could be simply considered as a spring with certain stiffness which restrains the deformation of the concrete specimen, as shown in Figure 5.1. Therefore, when the specimen tries to expand/shrink, only partial deformation is detected. With the known stiffness of the cracking frame (or the “spring constraint”) and the detected strain of that spring, the restrained stress can be estimated. But the full restraint stress cannot be measured in a cracking frame.

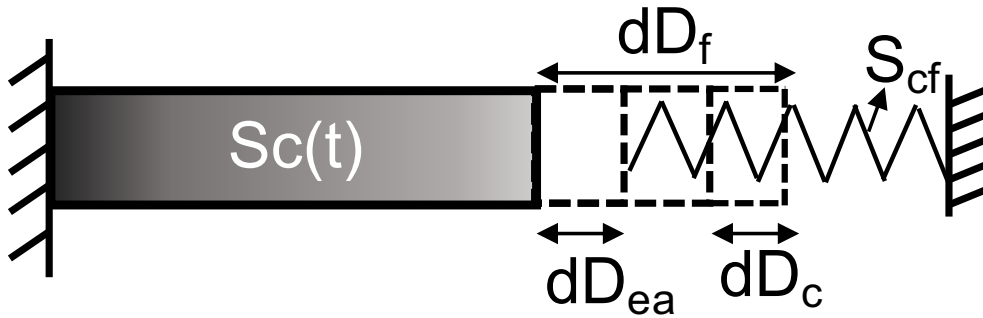


Figure 5.1 Modelling of Cracking Frame

If we assume the stiffness of concrete to be $S_c(t) = E_c(t)A_c/l_c$, where $E_c(t)$ denotes the time-dependent elastic modulus, A_c the area of the cross section of the concrete specimen and l_c the length of the specimen. And similarly, the stiffness of the cracking frame (or the spring) is defined as S_{cf} , the force in longitudinal direction should be balanced at each time step dt as Eq. (A.1):

$$(dD_f - dD_c - dD_{ea}) \cdot S_c(t) = dD_{ea} \cdot S_{cf} \quad (A.1)$$

Where dD_f and dD_c represents the total free deformation (if without any constraint), the creep (which means that this part of deformation is not considered to contribute any forces) respectively. dD_{ea} is the actual common deformation of the spring and specimen.

Interpretation on this Eq. (2.1) is given as follows: Supposed that the specimen freely deforms, originally the deformation would be dD_f at time interval dt . However, due to the restraint from the spring, the actual deformation is only dD_{ea} . Therefore, the actual compressed strain of the specimen is $dD_f - dD_{ea}$. If the specimen is a purely elastic materials, this part can be fully converted to stress, however, due to the creep effect of concrete, only the elastic part of this

Appendix

compressed strain can be considered, i.e., $dD_f - dD_{ea} - dD_c$. For clarity, we can use a function $e(t)$ to express the elastic part of the total free deformation, as given in Eq. (A. 2):

$$dD_f - dD_c = e(t) \cdot dD_f \quad (\text{A.2})$$

Where $0 \leq e(t) \leq 1$, Substitute Eq. (A.2) into Eq. (A.1) and rearrange, it yields:

$$dD_{ea} = \frac{e(t) \cdot dD_f}{\frac{S_{cf}}{S_c(t)} + 1} \quad (\text{A.3})$$

Integrating from time 0 to t, Eq. (A. 4) can be derived readily:

$$D_{ea}(t) = \int_0^t \frac{e(t)}{\frac{S_{cf}}{S_c(t)} + 1} D_f' dt \quad (\text{A.4})$$

Noted that in Eq. (A.4), the initial condition is that, at time $t=0$, $D_{ea}(t)=0$, $D_f(t)=0$.

First mean value theorem states that if $f: [a,b] \rightarrow \mathbb{R}$ is continuous and g is an integrable function there exists certain ξ in (a, b) such that:

$$\int_a^b f(x) g(x) dx = f(\xi) \int_a^b g(x) dx \quad (\text{A.5})$$

. By adopting this theorem, Eq. (A.4) could be rephrased as:

$$D_{ea}(t) = \frac{e(\xi)}{\frac{S_{cf}}{S_c(\xi)} + 1} \int_0^t D_f' dt = \frac{e(\xi)}{\frac{S_{cf}}{S_c(\xi)} + 1} D_f(t) \quad (\text{A.6})$$

In which $0 < \xi < t$. At early-age, the stiffness of the cracking frame spring is much larger than that of the concrete, i.e., $S_{cf}/S_c \gg 1$. It gives:

$$D_{ea} = \frac{e(\xi)}{\frac{S_{cf}}{S_c(\xi)}} D_f(t) \quad (\text{A.7})$$

This equation indicates that the actual deformation of the specimen is a part of the free deformation due to the creep effect $e(t)$. Also the actual deformation is related to the stiffness of the spring of the cracking frame S_{cf} . If we cast the same concrete mixture into two cracking frames with different stiffness (i.e., free deformation $D_{f1}(t) = D_{f2}(t)$), Eq. (A.7) will lead to

$$\frac{D_{ea-1}}{D_{ea-2}} = \frac{\frac{e(\xi_1)}{\frac{S_{cf1}}{S_c(\xi_1)}} D_{f1}}{\frac{e(\xi_2)}{\frac{S_{cf2}}{S_c(\xi_2)}} D_{f2}} \approx \frac{S_{cf2}}{S_{cf1}} \quad (\text{A.8})$$

It indicates that, if the second cracking frame has a stiffness n times higher than the first one, the actual deformation is just roughly $1/n$ of that of the first cracking frame when concrete's stiffness is still much lower than the frame. At later age when $S_{cf}/S_c \gg 1$ is no longer valid, Eq. (A.9) is more appropriate

$$\frac{D_{ea-1}}{D_{ea-2}} = \frac{\frac{e(\xi_1)}{S_{cf1}} D_{f1}}{\frac{e(\xi_2)}{S_{cf2}} D_{f2}} \approx \frac{S_{cf2} + S_c}{S_{cf1} + S_c} \quad (\text{A.9})$$

5.2 Modelling on Working Principle of TSTM

In this section, the Kovler's method which utilizes cumulative elastic strain detected by TSTM on evaluating creep strain will be discussed (Kovler, 1994; Kovler, Igarashi and Bentur, 1999). This method has been used by many other researchers to estimate early age creep effect in stressed state (Maruyama, Park and Noguchi, 2003; Tao and Weizu, 2006; Choi *et al.*, 2015; Zhao *et al.*, 2020). In the full-restraint condition of TSTM, when the detected deformation of the specimen reaches to the threshold value ($5 \mu m$ is used by (Kovler, 1994; Kovler, Igarashi and Bentur, 1999)), the step motor will drive the specimen back to original position. Each of this cycle is termed as a compensation cycle, as shown in Figure 5.2. In Kovler's method, it was considered that by accumulating all of these recoverable elastic strains in each cycle, the total elastic strain is determined. Simultaneously, another set of experiment for free shrinkage is conducted. Therefore two curves can be plotted: the free shrinkage curve, and the cumulative curves of all restored strains in each cycle. The difference of these two curves is considered as the creep deformation by Kovler.

However, it should be noted that the cumulative curve of all restored elastic strain cannot be simply regarded as the total elastic deformation, since one "invisible" part of the total elastic strain is converted to the internal stress of the concrete specimen (due to the confinement of the machine), which is not measured by the machine. The restored deformation is the detectable part that overcomes the confinement of the machine. Lin (Lin, 2006) had also pointed out that this problem and proposed a more realistic evaluation method for early-age creep effect using relaxed stress. In this section, the working principle of TSTM is mathematically reformulated in a more rigorous way to address three issues: (1) Compared to cracking frame, how TSTM achieves full-restrained condition and provides valuable information regarding the full-restrained stress development. (2) The derivation to clarify the limitation of Kovler's method. (3) How confinement of stiffness of the machine can affect the cumulative curve. These problems are key issues, which are served as a fundamental step for reproducible, comparable and consistent experimental results between TSTMs from varied organizations.

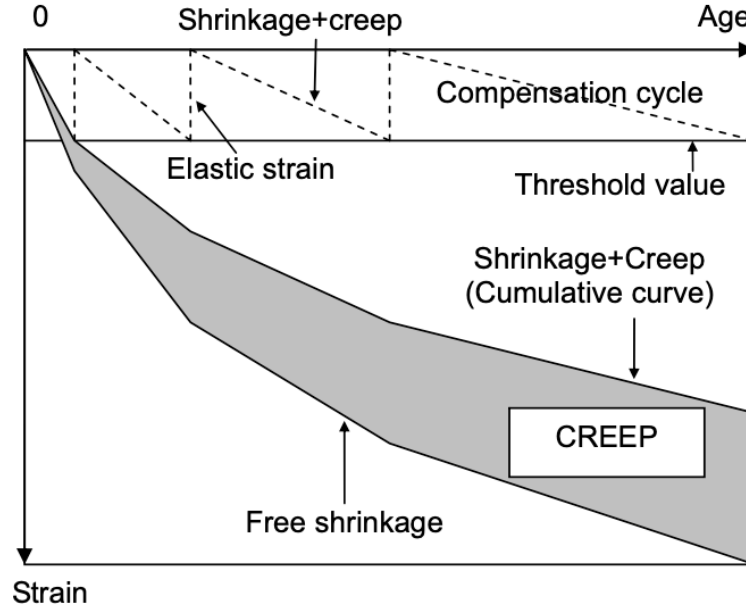


Figure 5.2 Creep and Free shrinkage in Kovler's Method

Firstly, the working principle of TSTM will be derived. Different from the cracking frame, TSTM has an adjustment mechanism which will drive the specimen back to the original position whenever threshold value is reached, as represented by a block in Figure 5.3. This adjustment system of TSTM will have its own stiffness, and when it is activated, an external force will be applied to move the specimen. Figure 5.3 and Figure 5.4 illustrate this process. Similar notations are used as the previous section about cracking frame, except that the stiffness of the machine is denoted as S_T and the displacement at each time step dt of the adjustment block is represented by dD_a .

At each compensation cycle, before the activation of the adjustment block, the following Eq. (B.1) is satisfied (i.e., the detected deformation is still within threshold value and step motor is not activated). It is just simply acting as a cracking frame, only that stiffness is changed to S_T :

$$(dD_f - dD_c - dD_{ea}) \cdot S_c(t) = dD_{ea} \cdot S_T \quad (B.1)$$

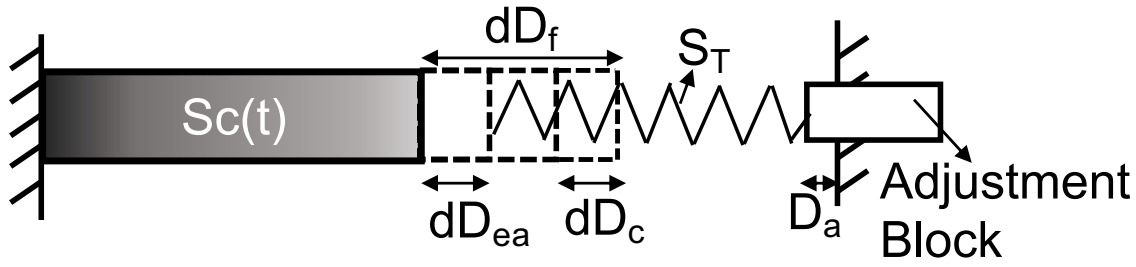


Figure 5.3 Before activation of adjustment

After the threshold value has been reached, the adjustment block will move and drive the specimen back to original position and the actual detected deformation $dD_{ea}=0$. It gives,

$$(dD_f - dD_c) \cdot S_c(t) = dD_a \cdot S_T \quad (B.2)$$

It also means that after each of this cycle, the increased stress in the concrete can be expressed by:

$$d\sigma \cdot A = (dD_f - dD_c) \cdot S_c(t) \quad (B.3)$$

Where A represents the area of cross section of the specimen and $d\sigma$ means the change of stress at this interval of time.

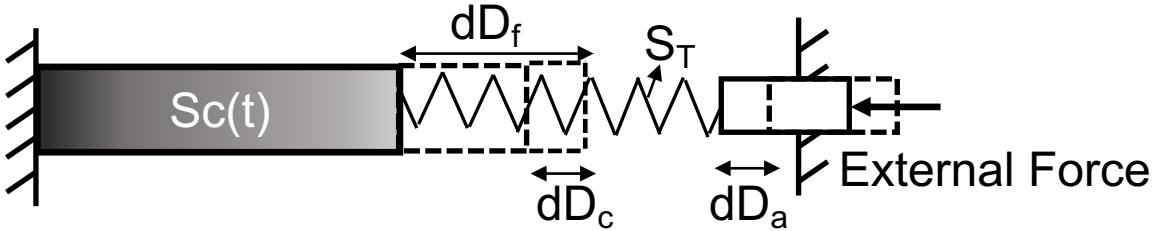


Figure 5.4 After activation of adjustment

Using Eq. (B.1) to Eq. (B.3), the relationship between cumulative curve, total elastic strain and accumulative restrained stress can be derived.

Integrating Eq. (B.1) from 0 to t can offers us the accumulated elastic deformation (again, the First mean value theorem is used):

$$D_{ea} = \int_0^t \frac{e(t)}{\frac{S_T}{S_c(t)} + 1} D_f' dt = \frac{e(\xi)}{\frac{S_T}{S_c(\xi)} + 1} D_f(t) \quad (B.4)$$

Therefore, the total cumulative restored elastic strain is not exactly equal to the total elastic deformation. If we let the total elastic deformation be expressed as $D_e(t) = e(t)D_f(t)$, we get:

$$D_{ea} = \frac{1}{\frac{S_T}{S_c(\xi)} + 1} D_e(t) \quad (B.5)$$

Appendix

Eq. (B.5) has an identical form as Eq. (A.6), indicating that the detected cumulative deformation is just one part of the total elastic deformation, and this detected cumulative deformation is dependent on the stiffness of the machine S_T . In other words, if same mix proportion is tested by two TSTMs with different stiffnesses, the tested cumulative curves will be different. Then, the subtracted creep effect from the free shrinkage will also be different (Figure 5.2). As expressed in Eq. (B.5), only if the stiffness of the machine $S_T = 0$, the cumulative curve becomes identical with the total elastic deformation, which is not realistic. Since each machine will more or less exert restriction on the crosshead (or grip) in the longitudinal direction.

By integrating Eq. (B.3), we can derive that:

$$\sigma(t) = \frac{\int_0^t S_c(t) \frac{(dD_f - dD_c)}{dt} dt}{A} = \frac{\int_0^t S_c(t) D_e' dt}{A} \quad (B.6)$$

Rearrange by first mean value theorem:

$$\sigma(t) = \frac{S_c(\xi) \cdot D_e(t)}{A} \quad (B.7)$$

Eq. (B.7) means that after same period of time passes by, the internal stress accumulated inside concrete will only be determined by the total elastic deformation and the stiffness of the materials, and not dependent on the stiffness of the machine. This is the way how TSTM with an adjustment mechanism can measure full-restraint stress. If the material properties are the same, the full-restraint stresses measured by TSTMs with different stiffnesses will still yield same results.

In this coming discussion, some experimental proofs from the UTokyo TSTM and other TSTMs will be provided to further validate our statements regarding Kovler's method. As shown in the left panel of Figure 5.5, experimental data on the full-restraint stress evolution using UTokyo TSTM reveals that the detected shrinkage of specimen is only part of the elastic strain, another part of it is converted to stress due to the confinement caused by the machine. When the displacement reaches $0.5 \mu m$, the step motor is activated and returns the specimen back to original position. It can also be assumed that, according to Eq. (B.5), if the system's stiffness is doubled, then at the same period of time, the evolution of stress values will be the same, while the cumulative elastic strain will be much less, due to a higher stiffness (accordingly, there will be less cycles since the specimen needs longer time to overcome the confinement).

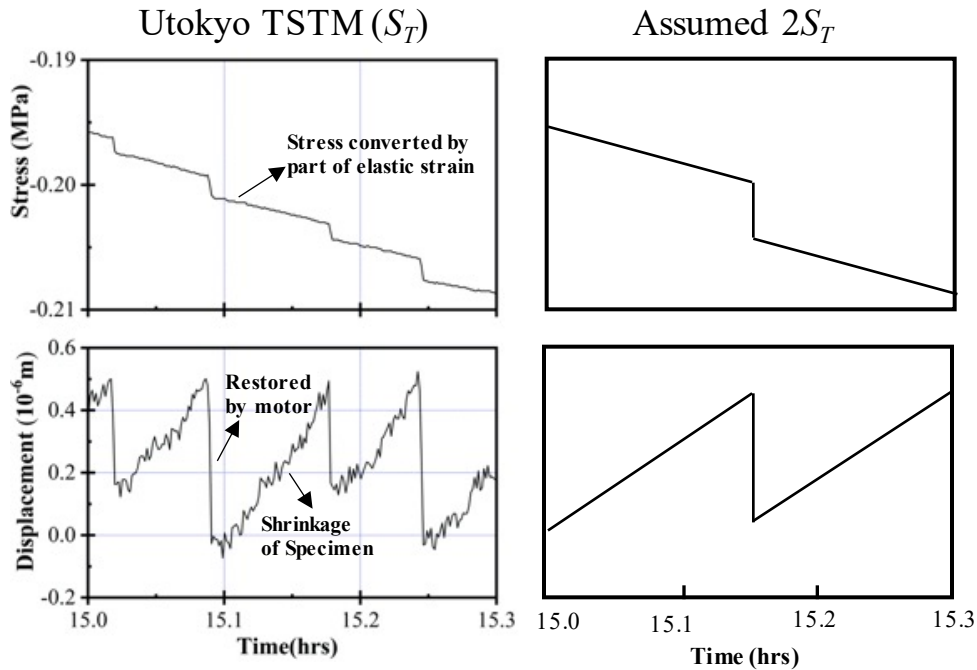


Figure 5.5 Experimental data on displacement restoration process (Left); Virtual evolution pattern if machine stiffness is doubled (Right)

Other researchers using Kolver's method on rather similar mix proportions have led to quite deviated outcomes for specific creep. As shown in Table 5.1, in both studies the water to binder ratio (w/c) and mix proportions for both OPC concrete are quite similar (Kovler, Igarashi and Bentur, 1999; Tao and Weizu, 2006), however it results in almost 50% discrepancy for the evaluated specific creep. It can be found in Figure 5.6, no matter for concrete blended with silica fume or OPC concrete, the differences are both around one time lower with respect to device I. Based on the above derivation (Eq. (B. 5)), it can be roughly estimated that probably device I has a stiffness which is around half of device-II (not "double" as stated in (Lin, 2006)), and thus ~two times of the cumulative elastic deformation is detected. Correspondingly, the creep effect measured from device I is just half of that of device II. Experimental evidences from their and our studies, along with the aforementioned mathematical derivation strongly indicate that Kovler's method does not offer us the realistic creep effect and thus, experiments from varied researchers cannot be directly compared. However, Kovler's method is convenient and it stills offer valuable though qualitative information, if comparison is conducted using the same device. In the future development, for consistent results from varied researches to accomplish more engineering and academic values, better evaluation method on early-age creep effect should be proposed.

Table 5.1 Mix Proportions for OPC and SF concrete used by two studies

Device	Concrete Type	w/b	Cement	Silica Fume	Water	Sand	Gravel
		kg/m ³					
K. Kovler Device I	OPC	0.33	506	--	167	572	1145
	SF	0.33	444	49	163	572	1145
T. Zhang Device II	OPC	0.35	500	--	175	690	1030
	SF	0.35	470	30	175	690	1030

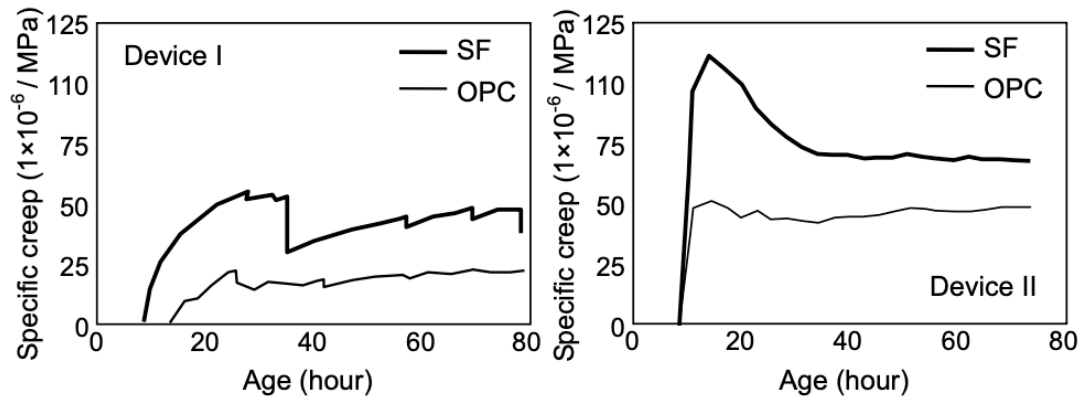


Figure 5.6 The large discrepancy on measurement of specific creep using different TSTM devices (Kovler, Igarashi and Bentur, 1999; Tao and Weizu, 2006)

5.3 Prediction of Adiabatic Temperature Rise

The multicomponent model for the heat of hydration from Kishi (Maekawa, Chaube and Kishi, 1999) is reproduced in this study and the validation is provided as the following. The mix proportion used is listed in Table 5.2. Figure 5.7 shows that the model can capture the temperature development quite well, no matter for EPC, OPC or MC.

Table 5.2 Concrete mix proportions in adiabatic temperature test

Notation	W/C (%)	W	C	S	G	AE (C%)
		kg/m ³				
EPC400	38.0	152	400	730	1058	0.25
EPC300	47.7	143	300	813	1092	0.25
EPC250	57.2	143	250	869	1071	0.25
OPC400	39.2	157	400	658	1129	0.25
OPC300	49.3	148	300	765	1129	0.25
OPC200	78.5	157	200	862	1089	0.25

MC400	39.2	157	400	663	1129	0.25
MC300	49.3	148	300	770	1129	0.25
MC200	78.5	157	200	865	1089	0.25

Note: EPC, OPC and MC stand for Early hardening Portland cement, ordinary Portland cement and moderate-heat Portland cement, respectively.

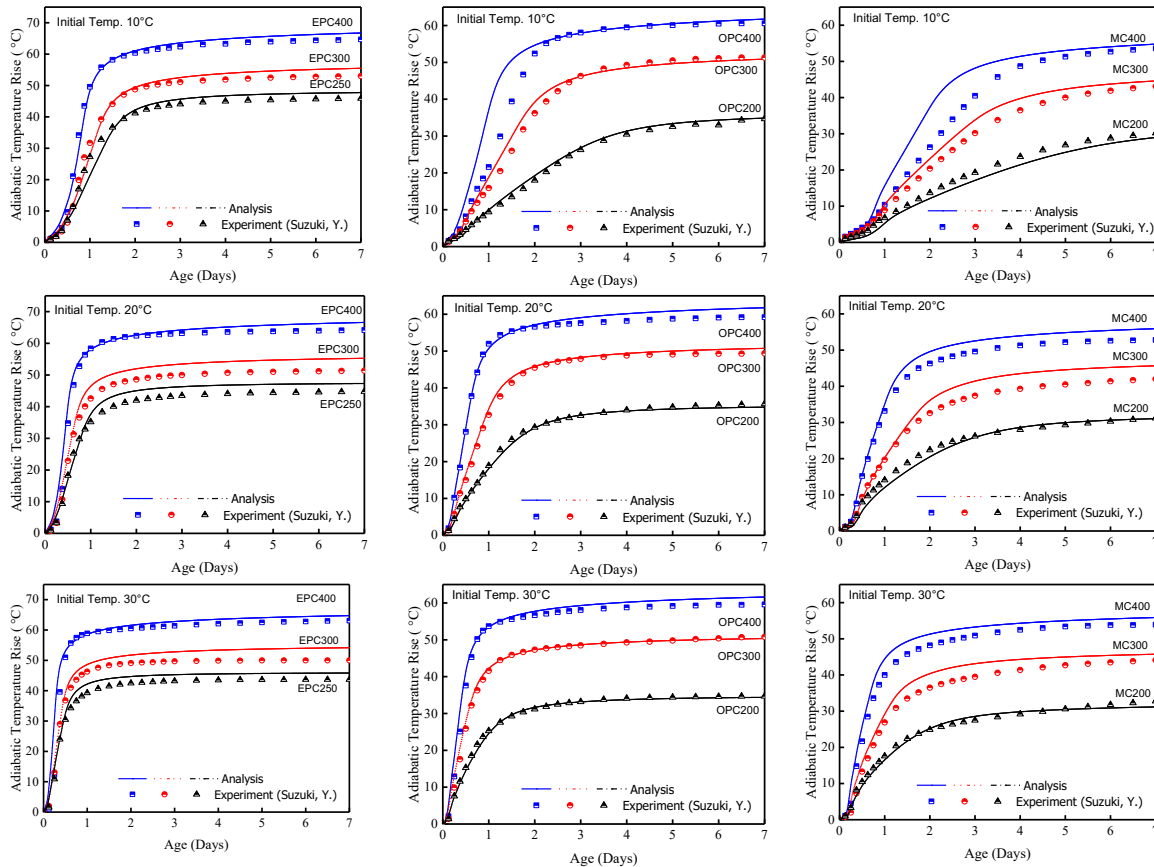


Figure 5.7 Validation of hydration heat model on adiabatic temperature rise

5.4 Estimation of Porosity from Bulk Density

In this section, the bulk densities of both low-density and high-density C-S-H are used for the computation for porosity inside each group of pores: The interlayer porosity, the gel porosity, inter-hydrate porosity and capillary porosity. Noted that since most of the bulk densities determined from traditional techniques (MIP, nitrogen adsorption test, etc.) requires drying pre-treatment of the specimen, it might vary with the realistic amount of pores. There is still a gap of understanding of traditional models (Jennings' Model, Powers' Model) with some recent ^1H -NMR findings. ^1H -NMR detects a large amount of gel pores and relatively small amount of capillary pores, especially when the specimen is cured underwater. It is not fully addressed in this

study. In this study, we trying to summarize some of these densities from various studies to form up a reasonable range of porosity. In the future, if with more accurate information, the porosity of each group of pore can be updated in the analytical model. But actually, how to quantify the effect of certain drying technique on porosity of a specific group of pore (e.g., gel pore) remains as a daunting, which requires very detailed and systematic characterization. In this study, the effect of drying on porosity and pore size distribution in each type of pore is not considered in the analytical model.

- The density of single sheet of C-S-H with all evaporable water removed is reported as 2.85 g/cm³ (Jennings, 2008b). Also, the density of aggregates of C-S-H layers (excluding gel pores) is detected as 2.604 g/cm³ by neutron and X-ray scattering (Allen, Thomas and Jennings, 2007) and 2.71 g/cm³ by ¹H-NMR (Muller *et al.*, 2013). Please noted that gel pores is excluded in this density. This is the density for solid C-S-H that includes all water physically bound within the internal structure of particles. The density of 2.604 g/cm³ has been considered as a density value with quite high accuracy, and therefore this value is chosen in this study.

By these information, we can estimate the interlayer porosity, by calculation as below. Considering one unit volume (1 cm³) of these closely-packed regions consisting of sheets of C-S-H with confined water inside (density taken as $\rho_{w,c} = 1.0\text{-}1.20$ g/cm³), the total mass of solid sheets and confined water should yield:

$$V_{t,s} \times 2.85 + (1 - V_{t,s}) \times \rho_{w,c} = 1 \times 2.604 \quad (D.1)$$

Where $V_{t,s}$ is the portion of true solid C-S-H excluding any evaporable water within one unit volume. $V_{t,s}$ is therefore to be computed as 85.1% ($\rho_{w,c} = 1.20$ g/cm³) to 86.7% ($\rho_{w,c} = 1.0$ g/cm³) and therefore, the interlayer porosity is 13.3% to 14.9% (per volume of close-packed C-S-H sheets with interlayer water in between).

- The optimized d-dried bulk density for HD C-S-H (Optimized from nitrogen adsorption test (Tennis and Jennings, 2000)) used in Jennings model is reported as 1.75 g/cm³ and that for LD C-S-H is 1.44 g/cm³. These density values are much lower than the 2.604 g/cm³, it must include gel pores and even some inter-hydrate pores and small capillary pores inside. It can be considered that the “units” with density of 2.604 g/cm³ are loosely or tightly packed with pores between, to form the LD C-S-H and HD C-S-H, respectively.

Now it comes to use 2.604 g/cm³ density and d-dried bulk density to estimate the porosity for other groups of pores. But noted that, the 2.604 g/cm³ density includes interlayer water, while d-dried state has been considered by researchers that, part of (or most of) these interlayer water will be removed (Taylor, 1997). Therefore, it can be thought that the d-dried state density will be lower. Whereas, meanwhile, at the dried state, the C-S-H layers will be compacted closer to each other and the density may be slightly higher due to this compaction. As a conservative treatment to both of the above phenomenon, we consider the range of d-dried density of these “units” will be from

Appendix

2.604 g/cm³ to 2.47 g/cm³ (with all water between layers dried and not compacted). Then, the porosity of both HD and LD C-S-H can be estimated as the followings. For d-dried state of the HD C-S-H, the water in non-interlayer pores must be emptied, density can be taken as 0.

$$V_{d-unit} \times \rho_{d-unit} + (1 - V_{d-unit}) \times 0 = 1.75 \times 1 \quad (D.2)$$

Where V_{d-unit} is the volume of d-dried units in one unit volume of HD C-S-H, and ρ_{d-unit} is the density of these d-dried units which ranges from 2.47 to 2.604 g/cm³. By this computation, the V_{d-unit} is estimated as 67.2% to 70.9%, and the porosity of HD C-S-H is therefore 29.1% to 32.8%. If one uses the above values to convert this d-dried HD C-S-H to the saturated state of HD C-S-H,

$$\rho_{sat,HD} \times 1 = V_{d-unit} \times \rho_{d-unit} + (1 - V_{d-unit}) \times 1.0 \quad (D.3)$$

We can obtain the saturated bulk density of HD C-S-H $\rho_{sat,HD}$ is ranging from 2.04 g/cm³ to 2.08 g/cm³. This saturated density of HD C-S-H, interestingly, is quite close to the maximum saturated bulk density of C-S-H detected by ¹H-NMR (Muller, 2014), which signifies the computed porosity for HD C-S-H is within reasonable range. The same logic can be applied to LD CSH. The porosity of LD C-S-H can be computed as 41.7% to 44.7%. After converting to the saturated density, $\rho_{sat,LD}$ is around 1.86 to 1.89 g/cm³. Now we can estimate the porosity of each group of pore.

- The interlayer porosity to gel porosity detected by ¹H-NMR is around 1:2 (Muller, 2014)

The interlayer porosity 13.3% to 14.9% is the porosity inside each unit, this value can be normalized into the porosity of LD C-S-H and HD C-S-H, which is around 10% volume of the C-S-H. For simplicity, it is considered 10% of C-S-H belongs to interlayer porosity. Then the gel porosity is 20%. The rest of pores can be assigned to inter-hydrate pores and small capillary pores within C-S-H products. It is considered in this study that HD C-S-H is in a relatively stable state (being tightly-packed), with only gel pores and inter-hydrate pores. Capillary pores are excluded in the HD C-S-H. The LD C-S-H, however, possesses certain portion of small capillary pores as well. Although these categorization is not directly validated, it is supported by high-resolution TEM images (ROSSEN, 2014). The following porosity can be derived:

→ HD C-S-H (tightly-packed agglomerates): 10% interlayer porosity, 20% gel porosity, 9.1%-12.8% inter-hydrate pores.

→ LD C-S-H (loosely-packed agglomerates): 10% interlayer porosity, 20% gel porosity, 21.7%-24.7% inter-hydrate pores.

Powers and Brownyard established a model based largely on evidence from total and non-evaporable water contents (Powers and BROWNYARD, 1946). In this model, hardened cement paste is assumed to comprise three phases (a) unreacted cement (b) hydration product (c) capillary pores. It is concluded that the hydration product has a “gel porosity” around 28%. Noted that here the gel porosity is not equivalent to the gel porosity defined in our study. Powers define this part

Appendix

of porosity is the total porosity inside all the hydration products. While in our categorization, the gel porosity is referred to the gel pores with diameter $\sim 2\text{-}5\text{nm}$, with the role of “gateway” for water exchange.

Firstly, with the previous established densification model, it offers us quantitative information of the amount of both LD and HD C-S-H at varied w/c and age. Secondly, using the porosity within this HD and LD C-S-H as computed above, it is found that for w/c=0.3 ($\alpha=0.7$, mature paste), the converted “gel porosity” corresponding to Powers’ definition is around 26%. Meanwhile for w/c=0.5 ($\alpha=0.9$, mature paste), the “gel porosity” is around 30.5%. Since the amount of LD and HD C-S-H varies with varied w/c and hydration degree, the “gel porosity” is also changed accordingly. But it is within the reasonable range and in good agreement with values of 28% suggested by Powers and 30% suggested by Taylor (Taylor, 1997)

6. REFERENCES

- AASHTO (2017) *AASHTO T 363 Standard Method of Test for Evaluating Stress Development and Cracking Potential due to Restrained Volume Change using a Dual Ring Test*.
- Allen, A. J., Thomas, J. J. and Jennings, H. M. (2007) 'Composition and density of nanoscale calcium-silicate-hydrate in cement', *Nature Materials*. Nature Publishing Group, 6(4), pp. 311–316. doi: 10.1038/nmat1871.
- Altoubat, S. A. and Lange, D. A. (2001) 'Creep, shrinkage, and cracking of restrained concrete at early age', *ACI Materials Journal*, 98(4), pp. 323–331. doi: 10.14359/10401.
- Asamoto, S. (2006) *Enhanced Multi-scale Constitutive Model of Solidifying Cementitious Composites and Application to Cracking Assessment of Concrete Structures*. The University of Tokyo.
- Asamoto, S., Ishida, T. and Maekawa, K. (2006) 'Time-dependent constitutive model of solidifying concrete based on thermodynamic state of moisture in fine pores', *Journal of Advanced Concrete Technology*, 4(2), pp. 301–323. doi: 10.3151/jact.4.301.
- ASTM (2004) *ASTM C1581-04 Standard Test Method for Determining Age at Cracking and Induced Tensile Stress Characteristics of Mortar and Concrete under Restrained Shrinkage*.
- ASTM (2017) *ASTM C157/C157M Standard Test Method for Length Change of Hardened Hydraulic-Cement Mortar and Concrete*.
- ASTM (2019) *ASTM C1698-19 Standard Test Method for Autogenous Strain of Cement Paste and Mortar*.
- Bazant, B. Z. P. and Baweja, S. (1997) 'Microprestress-solidification theory for concrete creep.', *Journal of Engineering Mechanics*, 123(November), pp. 1195–1201.
- Bazant, Z. P. (1988) *Mathematical Modeling of Creep and Shrinkage of Concrete*. JOHN WILEY AND SONS.
- Bazant, Z. P. (2001) 'Prediction of concrete creep and shrinkage: Past, present and future', *Nuclear Engineering and Design*. Elsevier Sequoia SA, 203(1), pp. 27–38. doi: 10.1016/S0029-5493(00)00299-5.
- Bentz, D. P. (1997) 'Three-dimensional computer simulation of portland cement hydration and microstructure development', *Journal of the American Ceramic Society*. Blackwell Publishing Inc., 80(1), pp. 3–21. doi: 10.1111/j.1151-2916.1997.tb02785.x.
- Bishnoi, S. (2008) 'Vector Modelling of Hydrating Cement Microstructure and Kinetics', *EPFL Phd Thesis*, 4093.
- Bishnoi, S. and Scrivener, K. L. (2009a) 'Studying nucleation and growth kinetics of alite hydration using μic ', *Cement and Concrete Research*. Elsevier Ltd, 39(10), pp. 849–860. doi: 10.1016/j.cemconres.2009.07.004.
- Bishnoi, S. and Scrivener, K. L. (2009b) ' μic : A new platform for modelling the hydration of cements', *Cement and Concrete Research*. Elsevier Ltd, 39(4), pp. 266–274. doi: 10.1016/j.cemconres.2008.12.002.
- Bizzozero, J., Gosselin, C. and Scrivener, K. L. (2014) 'Expansion mechanisms in calcium aluminate and sulfoaluminate systems with calcium sulfate', *Cement and Concrete Research*. Pergamon, 56, pp. 190–202. doi: 10.1016/j.cemconres.2013.11.011.
- van Breugel, K. (1995) 'Numerical simulation of hydration and microstructural development in hardening cement-based materials (I) theory', *Cement and Concrete Research*, 25(2), pp. 319–331. doi: 10.1016/0008-8846(95)00017-8.
- van Breugel, K. (1999) 'Mixture Optimization of HPC in view of autogenous shrinkage', in *Proc. 5th Int. Symp. on Utilization of High Strength/High Performance Concrete*, pp. 1041–1050.
- Chen, I. A., Hargis, C. W. and Juenger, M. C. G. (2012) 'Understanding expansion in calcium sulfoaluminate-belite cements', *Cement and Concrete Research*. Pergamon, 42(1), pp. 51–60.
- Choi, Hyeonngil *et al.* (2015) 'Modelling of creep of concrete mixed with expansive additives', *Magazine of Concrete*

REFERENCES

- Research*. Thomas Telford Services Ltd, 67(7), pp. 335–348. doi: 10.1680/mac.14.00249.
- Cohen, M. D. (1983a) ‘Modeling of expansive cements’, *Cement and Concrete Research*. Pergamon, 13(4), pp. 519–528. doi: 10.1016/0008-8846(83)90011-X.
- Cohen, M. D. (1983b) ‘Theories of expansion in sulfoaluminate - type expansive cements: Schools of thought’, *Cement and Concrete Research*. Pergamon, 13(6), pp. 809–818. doi: 10.1016/0008-8846(83)90082-0.
- Diamond, S. and Huang, J. (2001) ‘The ITZ in concrete - A different view based on image analysis and SEM observations’, *Cement and Concrete Composites*. Elsevier, 23(2–3), pp. 179–188. doi: 10.1016/S0958-9465(00)00065-2.
- Dridi, W. (2013) ‘Analysis of effective diffusivity of cement based materials by multi-scale modelling’, *Materials and Structures*. Springer, 46(1–2), pp. 313–326.
- Etzold, M. A., McDonald, P. J. and Routh, A. F. (2014) ‘Growth of sheets in 3D confinements - A model for the C-S-H meso structure’, *Cement and Concrete Research*. Elsevier Ltd, 63, pp. 137–142. doi: 10.1016/j.cemconres.2014.05.001.
- Feldman, R. F. and Sereda, P. J. (1968) ‘A model for hydrated Portland cement paste as deduced from sorption-length change and mechanical properties’, *Matériaux et Construction*. Springer, 1(6), pp. 509–520. doi: 10.1007/BF02473639.
- Feldman, R. F. and Sereda, P. J. (1970) ‘A new model for hydrated Portland cement and its practical implications’, *Engineering Journal (Canada)*, 53(8–9), pp. 53–59.
- Flatt, R. J. and Scherer, G. W. (2008) ‘Thermodynamics of crystallization stresses in DEF’, *Cement and Concrete Research*. Pergamon, 38(3), pp. 325–336. doi: 10.1016/j.cemconres.2007.10.002.
- Gajewicz, A. M. *et al.* (2016) ‘A 1H NMR relaxometry investigation of gel-pore drying shrinkage in cement pastes’, *Cement and Concrete Research*. Elsevier Ltd, 86, pp. 12–19. doi: 10.1016/j.cemconres.2016.04.013.
- Garci Juenger, M. C. and Jennings, H. M. (2001) ‘The use of nitrogen adsorption to assess the microstructure of cement paste’, *Cement and Concrete Research*. Pergamon, 31(6), pp. 883–892.
- Grudemo, A. (1979) *Strength-structure relationships of cement paste materials*, CBI Report. CBI.
- Hillerborg, A. (1985) ‘A modified absorption theory’, *Cement and Concrete Research*. Pergamon, 15(5), pp. 809–816. doi: 10.1016/0008-8846(85)90147-4.
- Hunt, C. M. (1966) *Nitrogen Sorption Measurements and Surface Areas Of Hardened Cement Pastes*.
- Ioannidou, K., Krakowiak, K. J., *et al.* (2016) ‘Mesoscale texture of cement hydrates’, *Proceedings of the National Academy of Sciences*. National Academy of Sciences, 113(8), pp. 2029–2034.
- Ioannidou, K., Kanduč, M., *et al.* (2016) ‘The crucial effect of early-stage gelation on the mechanical properties of cement hydrates’, *Nature Communications*. Nature Publishing Group, 7(1), pp. 1–9.
- Ioannidou, K., Pellenq, R. J. M. and Del Gado, E. (2014) ‘Controlling local packing and growth in calcium-silicate-hydrate gels’, *Soft Matter*. Royal Society of Chemistry, 10(8), pp. 1121–1133.
- Ishida, T. and Chaube, R. P. (1997) ‘Analysis of autogenous shrinkage and drying shrinkage of concrete based on micro structure’, in: Japan Concrete Institute.
- Ishida, T., Maekawa, K. and Kishi, T. (2007) ‘Enhanced modeling of moisture equilibrium and transport in cementitious materials under arbitrary temperature and relative humidity history’, *Cement and Concrete Research*, 37(4), pp. 565–578. doi: 10.1016/j.cemconres.2006.11.015.
- Jennings, Hamlin M. (2000) ‘A model for the microstructure of calcium silicate hydrate in cement paste’, *Cement and Concrete Research*. Elsevier Science Ltd, 30(1), pp. 101–116.
- Jennings, Hamlin M. (2000) ‘Reply to the discussion of the paper by Ivan Odler “A model for the microstructure of calcium silicate hydrate in cement paste”’, *Cement and Concrete Research*, 30(8), pp. 1339–1341.
- Jennings, H. M. (2004) ‘Colloid model of C–S–H and implications to the problem of creep and shrinkage’, *Materials and Structures*. Springer, 37(1), pp. 59–70.
- Jennings, H. M. *et al.* (2007) ‘A multi-technique investigation of the nanoporosity of cement paste’, *Cement and*

REFERENCES

Concrete Research, 37, pp. 329–336.

Jennings, H. M. (2008a) ‘Refinements to colloid model of C-S-H in cement: CM-II’, *Cement and Concrete Research*. Pergamon, 38(3), pp. 275–289.

Jennings, H. M. (2008b) ‘Refinements to colloid model of C-S-H in cement: CM-II’, *Cement and Concrete Research*. Pergamon, 38(3), pp. 275–289. doi: 10.1016/j.cemconres.2007.10.006.

Jennings, H. M. and Tennis, P. D. (1994) ‘Model for the Developing Microstructure in Portland Cement Pastes’, *Journal of the American Ceramic Society*. John Wiley & Sons, Ltd, 77(12), pp. 3161–3172.

Jiang, W., De Schutter, G. and Yuan, Y. (2014) ‘Degree of hydration based prediction of early age basic creep and creep recovery of blended concrete’, *Cement and Concrete Composites*. Elsevier, 48, pp. 83–90. doi: 10.1016/j.cemconcomp.2013.10.012.

Kishi, T. and Yoshida, R. (2008) ‘A Study on Several Ink-bottle Geometric Structures in Hardened Cement Paste (In Japanese)’, *SEISAN KENKYU*. 東京大学生産技術研究所, 60(5), pp. 512–515. doi: 10.11188/seisankenkyu.60.512.

Kolneath, P. (2021) *Development of an Expansive Agent Model for Concrete in a Multi-scale Thermodynamic Platform based on Hydration and Microstructure Formation*. The University of Tokyo.

Korpa, A. and Trettin, R. (2006) ‘The influence of different drying methods on cement paste microstructures as reflected by gas adsorption: Comparison between freeze-drying (F-drying), D-drying, P-drying and oven-drying methods’, *Cement and Concrete Research*, 36(4), pp. 634–649.

Kovler, K. (1994) ‘Testing system for determining the mechanical behaviour of early age concrete under restrained and free uniaxial shrinkage’, *Materials and Structures*. Kluwer Academic Publishers, 27(6), pp. 324–330. doi: 10.1007/BF02473424.

Kovler, K., Igarashi, S. and Bentur, A. (1999) *Tensile creep behavior of high strength concretes at early ages*, *Materials and Structures/Matériaux et Constructions*.

Lim, S., Lin, Z. and Kishi, T. (2008) ‘Thermal cracking sensitivity of slag and fly ash concretes by the uniaxial restraint test’, in: Japan Concrete Institute, p. Vol. 30, No.2.

Lin, Z. (2006) *Quantitative Evaluation of the Effectiveness of Expansive Concrete as a Countermeasure for Thermal Cracking and the Development of Its Practical Application*. The University of Tokyo.

Lin, Z. H. (2003) ‘Application of virtual instrument technology on the experimental evaluation of cracking sensitivity of early-age concrete’, *Industrial Construction*, pp. 37–40.

Lin, Z. H. and Kishi, T. (2006) ‘Cracking Resistance of Expansive Concrete Mixed With Lightweight Aggregate, Proceedings of the Japan Concrete Institute’, in *Proceedings of the Japan Concrete Institute*. Proceedings of the Japan Concrete Institute, pp. 28, 647–652.

Lingling, X. and Min, D. (2005) ‘Dolomite used as raw material to produce MgO-based expansive agent’, *Cement and Concrete Research*. Pergamon, 35(8), pp. 1480–1485. doi: 10.1016/j.cemconres.2004.09.026.

Luan, Y. and Ishida, T. (2013) ‘Enhanced shrinkage model based on early age hydration and moisture status in pore structure’, *Journal of Advanced Concrete Technology*, 11(12), pp. 360–373. doi: 10.3151/jact.11.360.

Lura, P. (2003) *Autogenous Deformation and Internal Curing of Concrete*. Delft University of Technology.

Lura, P., Jensen, O. M. and Van Breugel, K. (2003) ‘Autogenous shrinkage in high-performance cement paste: An evaluation of basic mechanisms’, *Cement and Concrete Research*. Pergamon, 33(2), pp. 223–232.

Ma, H. (2013) *H.Ma-PhD thesis.pdf*. The Hong Kong University of Science and Technology.

Ma, H. and Li, Z. (2013) ‘Realistic pore structure of Portland cement paste: Experimental study and numerical simulation’, *Computers and Concrete*, 11(4), pp. 317–336. doi: 10.12989/cac.2013.11.4.317.

Mabrouk, R., Ishida, T. and Maekawa, K. (2004) ‘A unified solidification model of hardening concrete composite for predicting the young age behavior of concrete’, *Cement and Concrete Composites*, 26(5), pp. 453–461. doi: 10.1016/S0958-9465(03)00073-8.

Maekawa, K., Chaube, R. and Kishi, T. (1999) *Modelling of Concrete Performance*. 1st edn. E & FN SPON.

Maekawa, K., Ishida, T. and Kishi, T. (2009) *Multi-scale modeling of structural concrete*. Taylor & Francis.

REFERENCES

- Maruyama, I. (2003) *Time dependent property of cement based materials on the basis of micro-mechanics*, PhD thesis. The University of Tokyo.
- Maruyama, I. *et al.* (2009) 'Evaluation of water transfer from saturated lightweight aggregate to cement paste matrix by neutron radiography', *Nuclear Instruments and Methods in Physics Research, Section A: Accelerators, Spectrometers, Detectors and Associated Equipment*, 605(1–2), pp. 159–162. doi: 10.1016/j.nima.2009.01.138.
- Maruyama, I. *et al.* (2018) 'Cavitation of water in hardened cement paste under short-term desorption measurements', *Materials and Structures/Materiaux et Constructions*. Springer Netherlands, 51(6), pp. 1–13. doi: 10.1617/s11527-018-1285-x.
- Maruyama, I. *et al.* (2019) 'Dynamic microstructural evolution of hardened cement paste during first drying monitored by ¹H NMR relaxometry', *Cement and Concrete Research*. Elsevier Ltd, 122, pp. 107–117. doi: 10.1016/j.cemconres.2019.04.017.
- Maruyama, I., Park, S. and Noguchi, T. (2003) 'Properties of high performance concrete in early age under quasi-complete restraint condition', *Proceedings of the Japan Concrete Institute*, 25(1), pp. 485–490.
- Mathur, P. C. (2007) *Study of cementitious materials using transmission electron microscopy*, PhD Thesis.
- Mehta, P. (2009) 'History and Status of Performance Tests for Evaluation of Soundness of Cements', in *Cement Standards—Evolution and Trends*. ASTM International, pp. 35–35–26. doi: 10.1520/stp35785s.
- Mehta, P. K. (1972) 'Chemistry and Microstructure of Expansive Cements', in. Berkeley: Conference on Expansive Cement Concretes, University of Berkeley.
- Mehta, P. K. (1973) 'Mechanism of expansion associated with ettringite formation', *Cement and Concrete Research*. Pergamon, 3(1), pp. 1–6. doi: 10.1016/0008-8846(73)90056-2.
- Mehta, P. K. and Monteiro, P. J. M. (2006) *Concrete: Microstructure, Properties and Materials*. 3rd edn. McGraw_Hill.
- Mizobuchi, T. (1998) 'Discussion on the experimental evaluation of reducing effect of thermal stress of expansive additive based on uniaxial restraint testing device, JCI conference', in, pp. 1051–1056.
- Mo, L. *et al.* (2014) 'MgO expansive cement and concrete in China: Past, present and future', *Cement and Concrete Research*. Elsevier Ltd, pp. 1–12.
- Mo, L., Deng, M. and Tang, M. (2010) 'Effects of calcination condition on expansion property of MgO-type expansive agent used in cement-based materials', *Cement and Concrete Research*. Pergamon, 40(3), pp. 437–446.
- Mo, L., Deng, M. and Wang, A. (2012) 'Effects of MgO-based expansive additive on compensating the shrinkage of cement paste under non-wet curing conditions', *Cement and Concrete Composites*. Elsevier, 34(3), pp. 377–383.
- Mohamed, A. K. *et al.* (2015) 'Atomistic structure of C-S-H from defective tobermorite structures: variations of defects and features', in *ICCC 2015, Beijing*. Available at: https://www.researchgate.net/publication/305496672_Atomistic_structure_of_C-S-H_from_defective_tobermorite_structures_variations_of_defects_and_features (Accessed: 19 January 2021).
- Muller, A. C. A. *et al.* (2013) 'Densification of C-S-H measured by ¹H NMR relaxometry', *Journal of Physical Chemistry C*. UTC, 117(1), pp. 403–412. doi: 10.1021/jp3102964.
- Muller, A. C. A. (2014) *Characterization of porosity & C-S-H in cement pastes by ¹H NMR*, PhD Thesis. EPFL.
- Nakarai, K. *et al.* (2007) 'Enhanced thermodynamic analysis coupled with temperature-dependent microstructures of cement hydrates', *Cement and Concrete Research*. Pergamon, 37(2), pp. 139–150. doi: 10.1016/j.cemconres.2006.10.006.
- Nguyen-Tuan, L. *et al.* (2020) 'Growth and porosity of C-S-H phases using the sheet growth model', *Cement and Concrete Research*. Elsevier Ltd, 129, p. 105960. doi: 10.1016/j.cemconres.2019.105960.
- Nguyen, D. H. *et al.* (2019a) 'Temperature-stress testing machine - A state-of-the-art design and its unique applications in concrete research', *Cement and Concrete Composites*. Elsevier, 102(October 2018), pp. 28–38. doi: 10.1016/j.cemconcomp.2019.04.019.
- Nguyen, D. H. *et al.* (2019b) 'Temperature-stress testing machine - A state-of-the-art design and its unique applications in concrete research', *Cement and Concrete Composites*. Elsevier Ltd, 102, pp. 28–38. doi:

REFERENCES

10.1016/j.cemconcomp.2019.04.019.

Non-structural Cracks in Concrete, Cement and Concrete Society, United Kingdom (1978).

Odler, I., Hagymassy, J., Yudenfreund, M., Hanna, Kaissar M., *et al.* (1972) 'Pore structure analysis by water vapor adsorption. IV. Analysis of hydrated portland cement pastes of low porosity', *Journal of Colloid And Interface Science*. Academic Press, 38(1), pp. 265–276. doi: 10.1016/0021-9797(72)90242-1.

Odler, I., Hagymassy, J., Yudenfreund, M., Hanna, Kaissar M., *et al.* (1972) *Pore Structure Analysis by Water Vapor Adsorption IV. Analysis of Hydrated Portland Cement Pastes of Low Porosity*.

Odler, I. (2000) 'Discussion of the paper "A model for the microstructure of calcium silicate hydrate in cement pastes" by H. M. Jennings', *Cement and Concrete Research*, 30, pp. 101–106.

Odler, I. (2003) 'The BET-specific surface area of hydrated Portland cement and related materials', *Cement and Concrete Research*, 33(12), pp. 2049–2056.

Pane, I. and Hansen, W. (2002) 'Early age creep and stress relaxation of concrete containing blended cements', *Materials and Structures/Materiaux et Constructions*. RILEM Publications, 34(246), pp. 92–96. doi: 10.1007/bf02482107.

Petersen, T. *et al.* (2018) 'A reaction model for cement solidification: Evolving the C–S–H packing density at the micrometer-scale', *Journal of the Mechanics and Physics of Solids*. Elsevier Ltd, 118, pp. 58–73. doi: 10.1016/j.jmps.2018.05.010.

Polivka, M. (1973) 'Factors Influencing Expansion Of Expansive Cement Concretes', in. ACI (Publ SP-38), pp. 239–250.

Powers, T. C. and BROWNYARD, T. L. (1946) 'Studies of The Physical Properties of Hardened Portland Cement Paste', *Portland Cement Assoc R & D Lab Bull*, (0).

R. Springenschmid (ed.) (1994) *Thermal Cracking in Concrete at Early Ages*. 1st edn, RILEM Symposium (Munich). 1st edn. E & FN SPON.

ROSSEN, J. E. (2014) *Composition and morphology of C-A-S-H in pastes of alite and cement blended with supplementary cementitious materials*. EPFL.

Smilauer, V. and Bittnar, Z. (2006) 'Microstructure-based micromechanical prediction of elastic properties in hydrating cement paste', *Cement and Concrete Research*. Pergamon, 36(9), pp. 1708–1718. doi: 10.1016/j.cemconres.2006.05.014.

Sanahuja, J., Dormieux, L. and Chanvillard, G. (2007) 'Modelling elasticity of a hydrating cement paste', *Cement and Concrete Research*. Elsevier Ltd, 37(10), pp. 1427–1439. doi: 10.1016/j.cemconres.2007.07.003.

Skalny, J. and Odler, I. (1972) 'Pore structure of hydrated calcium silicates. III. Influence of temperature on the pore structure of hydrated tricalcium silicate', *Journal of Colloid And Interface Science*. Academic Press, 40(2), pp. 199–205. doi: 10.1016/0021-9797(72)90009-4.

Springenschmid, R. (1998) *Prevention of Thermal Cracking in Concrete at Early Ages*, RILEM. Munich, Germany: E & FN SPON.

Standard (2007) *BS EN 197-1:2000 Cement-Part 1: Composition, Specifications and Conformity Criterion for Common Cements*.

Standard (2009) *GB 175-2007/XG 1-2009, National Standard of The People's Republic of China, Common Portland Cements, (in Chinese)*.

Standard (2012) 'ASTM C150M-12, Standard Specification for Portland Cement'.

Tao, Z. and Weizu, Q. (2006) 'Tensile creep due to restraining stresses in high-strength concrete at early ages', *Cement and Concrete Research*. Pergamon, 36(3), pp. 584–591. doi: 10.1016/j.cemconres.2005.11.017.

Taylor, H. F. W. (1997) *Cement chemistry*. Thomas Telford Services Ltd.

Taylor, H. F. W., Famy, C. and Scrivener, K. L. (2001) 'Delayed ettringite formation', *Cement and Concrete Research*. Pergamon, pp. 683–693. doi: 10.1016/S0008-8846(01)00466-5.

Tazawa, E. *et al.* (2000) *Work of JCI committee on autogenous shrinkage*. Paris: RILEM Workshop on Shrinkage of

REFERENCES

Concrete.

- Tennis, P. D. and Jennings, H. M. (2000) 'A model for two types of calcium silicate hydrate in the microstructure of Portland cement pastes', *Cement and Concrete Research*. Elsevier Science Ltd, 30(6), pp. 855–863.
- Thomas, J. J. and Jennings, H. M. (2006) 'A colloidal interpretation of chemical aging of the C-S-H gel and its effects on the properties of cement paste', *Cement and Concrete Research*. Pergamon, 36(1), pp. 30–38.
- Thomas, J. J., Jennings, H. M. and Allen, A. J. (1998) 'The surface area of cement paste as measured by neutron scattering: Evidence for two C-S-H morphologies', *Cement and Concrete Research*. Elsevier Ltd, 28(6), pp. 897–905.
- Vandamme, M., Ulm, F. J. and Fonollosa, P. (2010) 'Nanogranular packing of C-S-H at substoichiometric conditions', *Cement and Concrete Research*. Pergamon, 40(1), pp. 14–26.
- Wyrzykowski, M. *et al.* (2019) 'Water Redistribution–Microdiffusion in Cement Paste under Mechanical Loading Evidenced by ^1H NMR', *The Journal of Physical Chemistry C*. American Chemical Society, 123(26), pp. 16153–16163. doi: 10.1021/acs.jpcc.9b02436.
- Zeng, Q. *et al.* (2016) 'Pore structure of cement pastes through NAD and MIP analysis', *Advances in Cement Research*, 28(1), pp. 23–32. doi: 10.1680/adcr.14.00109.
- Zhao, Z. *et al.* (2020) 'Tensile Creep Model of Slab Concrete Based on Microprestress-Solidification Theory', *Materials*. MDPI AG, 13(14), p. 3157. doi: 10.3390/ma13143157.
- Zheng, L., Xuehua, C. and Mingshu, T. (1991) 'MgO-type delayed expansive cement', *Cement and Concrete Research*. Pergamon, 21(6), pp. 1049–1057. doi: 10.1016/0008-8846(91)90065-P.